Evaluation of Radiation Field Properties with Pixel Semiconductor Detectors Operating in Particle Tracking Mode

Inauguraldissertation

Zur Erlangung der Doktorwürde
der Fakultät für Chemie, Pharmazie und Geowissenschaften
der Albert-Ludwigs-Universität Freiburg im Breisgau

Vorgelegt von

Zdenek Vykydal
aus Prag

2012

Vorsitzender des Promotionsausschusses: Prof. Dr. Arne Cröll
Referent: PD Dr. Michael Fiederle
Korreferent: Prof. Dr. Stanislav Pospisil

Datum der Promotion: 11.6.2012   (Tag der mündlichen Prüfung)

Abstract

The usage of radiation detectors covers a wide range of applications from basic research towards industry or medicine. Continuous technological progress in electronic fabrication processes with help of the sophisticated data analysis methods now allows faster extraction of more complex information about interacting particles.

This thesis defines the methodology of evaluation of complex radiation field properties using Medipix2 semiconductor pixel detector which has been successfully used in the network of 16 detectors installed and operated in the ATLAS experiment at CERN in the frame of ATLAS-MPX project. The aim of the network is to perform real-time measurements of spectral characteristics and composition of the radiation environment inside the ATLAS detector. With the devices, in two different modes of operation, a large dynamic range of particle flux can be covered, of at least 9 orders of magnitude, which corresponds to the highest luminosity, while also measurements of the radiation background outside the collisions can be made. An important goal is the determination of the neutron component of the mixed radiation field. To identify different types of neutrons, the 300 μm thick silicon sensor area of each ATLAS-MPX device has been divided into several regions, covered by different neutron converter materials. A ^{6}LiF layer is used for thermal neutron detection and a polyethylene foil for fast neutron detection. The calibration of the detection efficiency of all devices has been performed with various known neutron sources: ^{252}Cf, ^{241}AmBe, thermal neutrons and 14 MeV neutrons from Van de Graaff accelerator.

ATLAS-MPX devices have been operated almost continuously starting from early 2008 (background and cosmic radiation measurements and the first LHC beam appearances in 2008 and 2009) through the stable LHC operation during the 2010 and 2011 run periods up to nowadays. This thesis presents the first evaluations of the luminosity dependence, activation of the environment and comparison of the different radiation groups with the Monte Carlo simulations.

Based on the several years of experience with ATLAS-MPX network operation and data analysis several ideas for the future upgrade of the detector network are presented including new Timepix readout chip, multilayer detector concept and possibility of usage of the CdTe sensor material.

The results presented in this thesis have proven to be an important feedback for ATLAS community and will possibly allow the calculation of the safety factors to be used in the future to determine the viability of the ATLAS electronics exposed to growing doses of neutrons and photons, in particular in view of planned LHC upgrade. There is a growing interest in these results also from the other large LHC experiments.

Abstrakt

Die Nutzung von Strahlungsdetektoren umfasst einen weiten Bereich von Anwendungen in der Grundlagen-Forschung bis zur Industrie- und Medizin-Applikationen hin. Der kontinuierliche technologische Fortschritt in der Elektronik-Fertigung in Kombination mit hochentwickelter Daten-Analyse erlaubt heute eine schnellere Extrahierung von komplexen Informationen über wechselwirkende Teilchen.

Diese Arbeit beschreibt die Methodik der Auswertung komplexer Strahlungsfelder durch Nutzung von pixelierten Medipix2 Halbleiter-Detektoren, die erfolgreich im Rahmen des ATLAS-MPX Projekts am CERN beim ATLAS-Experiment in einem Netzwerk von 16 Detektoren installiert und betrieben wurden. Das Ziel dieses Netzwerks ist die Durchführung von Echtzeit-Messungen über spektrale Charakteristiken und die Strahlungsumgebung innerhalb des ATLAS-Detektors. Mit den Medipix2-Detektoren, die in zwei unterschiedlichen Betriebsweisen eingesetzt werden, kann ein hoher dynamischer Bereich von Teilchenflüssen erfasst werden, der mindestens 9 Größenordnungen überstreicht und damit sowohl Messungen bei höchster Luminosität als auch Untergrundmessungen ohne Teilchenkollisionen ermöglicht. Ein wichtiges Ziel ist die Bestimmung der Neutronenkomponente des gemischten Strahlungsfelds. Um die unterschiedlichen Neutronentypen zu identifizieren, wurde die Fläche des 300 μm dicken Silizium Sensors jedes ATLAS-MPX Geräts in unterschiedliche Regionen eingeteilt und mit verschiedenen Neutronen-Konvertern beschichtet. Eine ^{6}LiF Schicht wird zur Detektion thermischer Neutronen genutzt und eine Polyethylen Folie für den Nachweis schneller Neutronen. Die Detektionseffizienz-Kalibrierung aller Geräte wurde mit bekannten Neutronenquellen durchgeführt: ^{252}Cf, ^{241}AmBe, thermischen Neutronen und 14 MeV Neutronen von einem Van de Graaff Beschleuniger.

Die ATLAS-MPX Geräte wurden nahezu kontinuierlich betrieben, beginnend Anfang 2008 mit Messungen des Untergrunds und der kosmischen Strahlung, nachfolgend mit ersten LHC Strahl-Messungen 2008 und 2009, und weiterführenden Messungen während des stabilen LHC Betriebs in den Jahren 2010 und 2011 bis heute. Diese Arbeit präsentiert erste Untersuchungen der Luminositäts-Abhängigkeit, der Aktivierung der Umgebung und einen Vergleich der unterschiedlichen Strahlungs-Gruppen mit Monte Carlo Simulationen.

Basierend auf den jahrelangen Erfahrungen mit dem ATLAS-MPX Netzwerk und der zugehörigen Datenanalyse werden einige Ideen für zukünftige Upgrades des ATLAS Detektor Netzwerks präsentiert inklusive des neuen Timepix Auslese-Chips, Vielschicht-Detektor-Konzepten und der Möglichkeit der Nutzung von CdTe Sensor Material.

Die in dieser Arbeit vorgestellten Resultate haben sich als wichtiges Feedback für die ATLAS Community herausgestellt und werden möglicherweise die Berechnung von Sicherheitsfaktoren für die Funktionsfähigkeit zukünftiger ATLAS Elektroniken erlauben, die insbesondere durch das geplante LHC Upgrade zunehmend höheren Dosen von Neutronen und Photonen ausgesetzt sein werden. Auch die anderen, großen LHC Experimenten zeigen ein wachsendes Interesse an diesen Resultaten.

Acknowledgements

Content

Used Abbreviations

ADC	**A**nalog to **D**igital **C**onverter
ALICE	**A** **L**arge **I**on **C**ollider **E**xperiment
ASIC	**A**pplication **S**pecific **I**ntegrated Circuit
ATLAS	**A** **T**oroidal **LHC** **A**pparatu**S**
BCM	The **B**eam **C**ondition **M**onitor
CCD	**C**harge **C**oupled **D**evice
CdTe	**Cad**mium **Te**lluride
CdZnTe	**Cad**mium **Zin**c **Te**lluride
CMOS	**C**omplementary **M**etal **O**xide **S**emiconductor
CMS	**C**ompact **M**uon **S**olenoid
DAC	**D**igital to **A**nalog **C**onverter
ESTAR	**E**lectron **ST**opping powers **A**nd **R**anges
FPGA	**F**ield **P**rogrammable **G**ate **A**rray
GMT	**G**reenwich **M**ean **T**ime
HETP	**H**igh **E**nergy **T**ransfer **P**articles
IP	**I**nteraction **P**oint
KERMA	**K**inetic **E**nergy **R**eleased per unit **MA**ss
LETP	**L**ow **E**nergy **T**ransfer **P**articles
LHC	**L**arge **H**adron **C**ollider
LHCb	**L**arge **H**adron **C**ollider **b**eauty
LiF	**L**ithium **F**luoride
LUCID	**LU**minosity measurement using a **C**herenkov **I**ntegrating **D**etector
LVDS	**L**ow **V**oltage **D**ifferential **S**ignaling
MIP	**M**inimum **I**onizing **P**article
MoEDAL	The **Mo**nopole and **E**xotics **D**etector **a**t the **L**HC
MPX	**M**edi**P**i**X**2
PCB	**P**rinted **C**ircuit **B**oard
SEE	**S**ingle **E**vent **E**ffect
SEU	**S**ingle **E**vent **U**pset
SNR	**S**ignal to **N**oise **R**atio
SRIM	The **S**topping and **R**ange of **I**ons in **M**atter
TOT	**T**ime **O**ver **T**hreshold
THL	**Th**resho**l**d
VDM	**V**an **d**er **M**eer
XCOM	Photon cross sections on a personal **COM**puter

List of Figures

List of Tables

1. Introduction

Better radiation detectors and methods have been sought since the discovery of the natural radioactivity by H. Becquerel and X-ray imaging by W. Roentgen in the late 19th century. Starting from the photographic plates over various types of track chambers, photographic films and nuclear emulsions the direction of the development in radiation detection is nowadays connected closely to the field of electronics.

Semiconductor detectors become important in the early 60s after the successful development of high purity silicon and germanium crystals for electronic industry. It offers better energy resolution, linearity of response over wide energy range and compact dimensions. Continuous technological progress in electronic fabrication processes in the last decades opens up new possibilities in ionizing radiation detection. Although, the interaction principles are the same, increased miniaturization level allows faster extraction of more information about interacting particles and using sophisticated data analysis methods.

The goal of this thesis is to define the methodology of evaluation of complex radiation field properties using Medipix2 semiconductor pixel detectors [1] in real-time. This concept was successfully applied in the network of 16 Medipix2-based detectors installed and operated in the ATLAS experiment at CERN in the frame of ATLAS-MPX project [2], [3]. Work on this project starting from the detectors preparation and calibration measurements over the installation of the devices in the ATLAS experimental cavern and data evaluation form a main part of this thesis. The text is organized as described below.

Section 2 describes fundamental principles of radiation interaction with matter, summarizes basic properties of several semiconductor materials and gives a brief overview of a selection of pixel detector technologies.

Section 3 provides detailed description of a hybrid single photon counting pixel detector Medipix2. Two different methods of evaluation of the data from Medipix2 pixel detector in different radiation fields are described. The characteristics of the Medipix2 detectors allow a very large dynamic range to be covered, of at least 9 orders of magnitude, by the use of two different modes of analyzing the detector output. The "tracking mode" permits to visualize individual cluster of every charged particle

interacting in the sensor providing spectral information. In the "counting mode" the signal from individual interactions is overlapped so the spectral information is averaged but the statistics can be significantly higher.

In section 4 the description of the ATLAS-MPX project is given. The aim of the project is to measure spectral characteristics and composition of radiation in and around the ATLAS detector. This information is necessary for understanding the performance of various detector systems and to predict their useful lifetimes. Data generated by the ATLAS-MPX network are available at the ATLAS Detector Operation web page and are regularly sent to ATLAS control room. A manual for accessing the information is found in Appendix A.

Section 5 describes the calibration procedures performed on the Medipix2 devices installed in the ATLAS environment. The calibration process was rather complex using different known radiation sources with focus on the neutrons as one of the main aims of the ATLAS-MPX project.

Section 6 summarizes the main results of the ATLAS-MPX network data analysis after 3 years of successful operation.

Section 7 presents the first comparison of the ATLAS-MPX network measurements and Monte Carlo predictions for four defined particle categories.

Section 8 is devoted to the ideas for the future upgrade of the ATLAS-MPX detector network. Main improvement will be usage of the Timepix readout chips which brings the possibility to measure energy deposited by each individual radiation quanta interacting in the sensor volume. The concept of multilayer device is proposed in order to determine also the direction of energetic particles. First tests with Cadmium Telluride (CdTe) sensor chip bonded to Timepix readout chip are presented with the evaluation of benefit from the higher detection efficiency of this material to gamma radiation.

Conclusions of the results of the thesis are summarized in section 9. General conclusions about the work are drawn and the main results are discussed.

2. Basic principles of the radiation detection

This chapter presents an overview of fundamental principles of radiation interaction with matter in subsection 2.1. Subsection 2.2 focuses on the semiconductor detectors summarizing basic properties of several semiconductor materials and giving a brief overview of a selection of pixel detector technologies.

2.1 Interaction of the radiation with matter

The capability of a specific material as a radiation detector basically depends on the manner in which the radiation interacts with such detection medium. An understanding the fundamental mechanisms of radiation interaction is necessary to understand correctly the detector response. Following subsections gives and overview of the interaction mechanisms of the main four radiation species:

- Heavy charged particles
- Electrons
- Photons (X-rays, gamma rays)
- Neutrons

First two groups are charged particles which continuously interact through the Coulomb electrostatic force with the electrons present in any detection material through which they pass. Second two groups are particles with no charge. They have to interact with the detection medium first transferring all or part of its energy to electrons or nuclei of the detection medium atoms or to charged particle products of the nuclear reactions. Consequently, the charged products of the interactions can be detected as for the first two groups.

2.1.1 Heavy charged particles

Heavy charged particles lose their energy mainly by means of Coulomb interactions with the electrons and nuclei of the absorbing material. Collisions with free or bound electrons result in ionization or excitation of the atoms of the detection medium while interaction with nuclei leads to the Rutherford scattering or nuclear reactions. Energy lost by the incident particle in the interactions with electrons of the semiconductor target material

generates an electron-hole pair and contributes to the detection process. The collisions with the atomic nuclei are rare and not significant in the response of semiconductor radiation detectors.

Assuming that the incident particle mass is much higher that electron mass it practically doesn't deviate from the original direction during the collisions. Interaction of such particle with the detector is characterized by the specific energy loss S described by the Bethe formula:

$$S = -\frac{dE}{dx} = \frac{4\pi e^4 z^2}{m_e v^2} NZ \left[\ln\left(\frac{2m_e v^2}{I}\right) - \ln\left(1 - \frac{v^2}{c^2}\right) - \frac{v^2}{c^2} \right] \qquad (1)$$

where m_e is the electron mass, v and ze are the velocity and charge of the primary particle, N and Z are the atom density and atomic number of the target material. I is the average ionization and excitation potential of the absorption material [4]. A plot of the specific energy loss of protons and alpha particles in silicon is shown in Fig. 1.
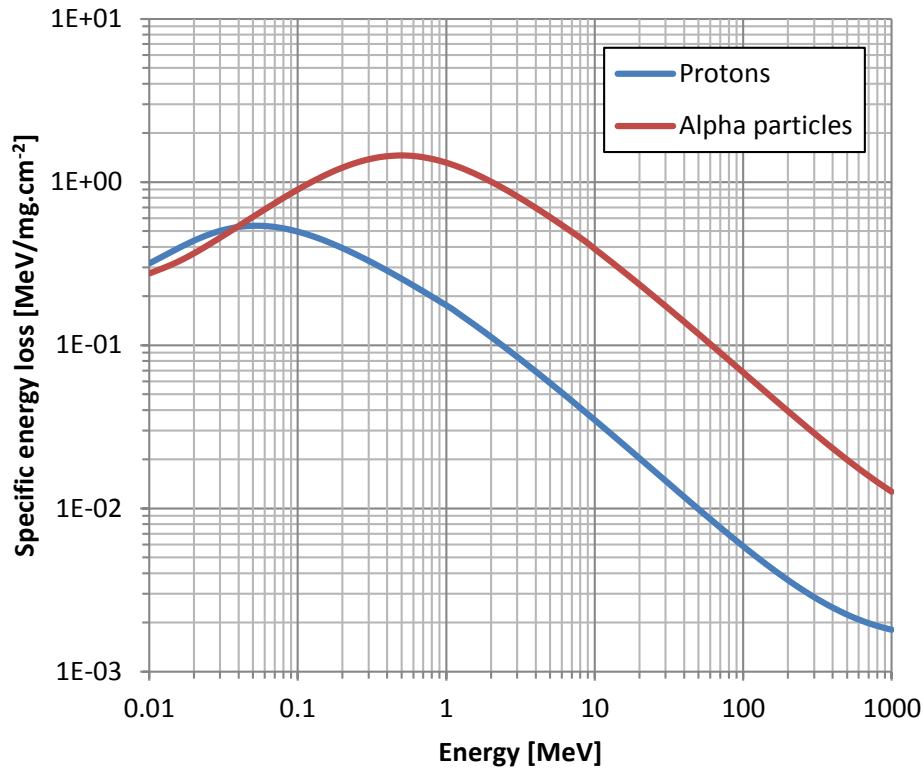
Figure 1. Specific energy loss of protons and alpha particles in silicon calculated in SRIM [5].

A plot of the specific energy loss along the track of a charged particle is known as the Bragg curve. An example for an alpha particle of initial energy 5 MeV for different target materials (silicon, germanium and cadmium telluride) is illustrated in Fig. 2. For most of the track the specific energy loss increases roughly as $1/E$ (kinetic energy of the alpha particle) as predicted by Eq. (1). Near end of the track the initial charge of the alpha particle is reduced because of electron pickup and the specific energy loss falls sharply.
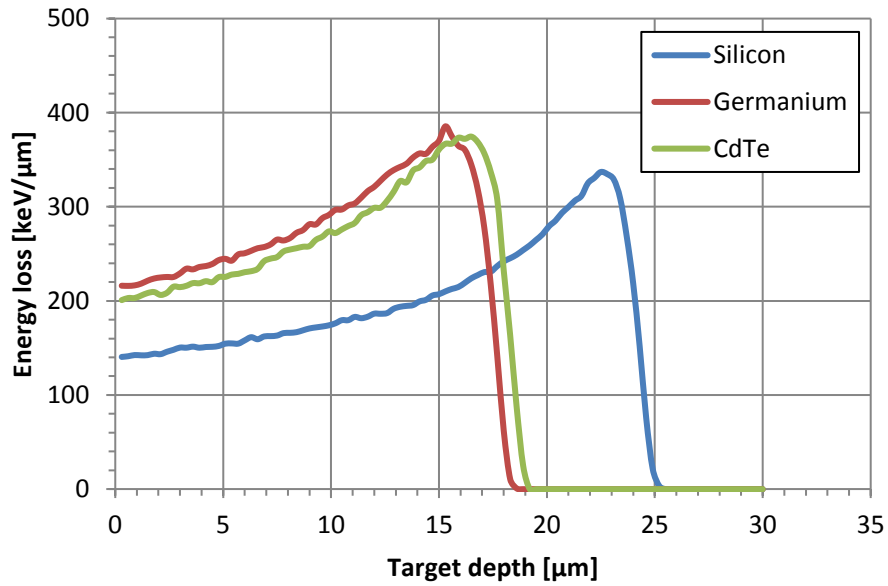
Figure 2. A typical shape of the Bragg curve showing the variation of the energy loss as a function of the penetration depth of the alpha particles in different materials calculated in SRIM [5].
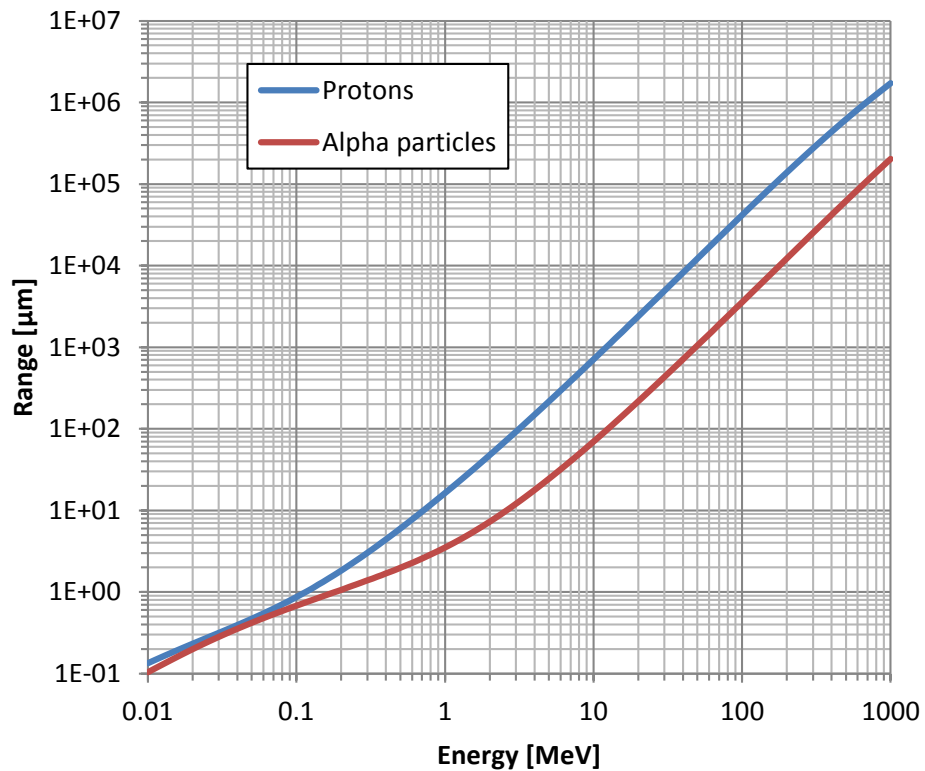
Figure 3. Range of protons and alpha particles in silicon calculated in SRIM [5].

The range of the given heavy ionizing particle in target material can be calculated by integrating the reciprocal stopping power from Eq. (1) over energy. The range is fairly

unique value specific for the absorber material. Ranges of protons and alpha particles in silicon are depicted on Fig. 3. Any detector capable to measure the full incident energy of the charged particles must have an active thickness that is greater than the range of those particles in the detector material.

2.1.2 Electrons

Coulomb interaction of electrons with matter can be described with the specific energy loss similarly to the heavy charged particles. However, because of lower electron mass the trajectory of the interacting electron in the target material is not straight but its direction changes significantly after each collision. The electron interaction in target material cannot be characterized with the characteristic range as in the case of heavy charged particles. Continuous slowing down approximation range (CSDA) is used instead as a very close approximation of the average part length of the electron in the absorbing material (see Fig. 4). Target material with thickness greater than the CSDA range ensures that almost no electrons with corresponding energy can pass through.
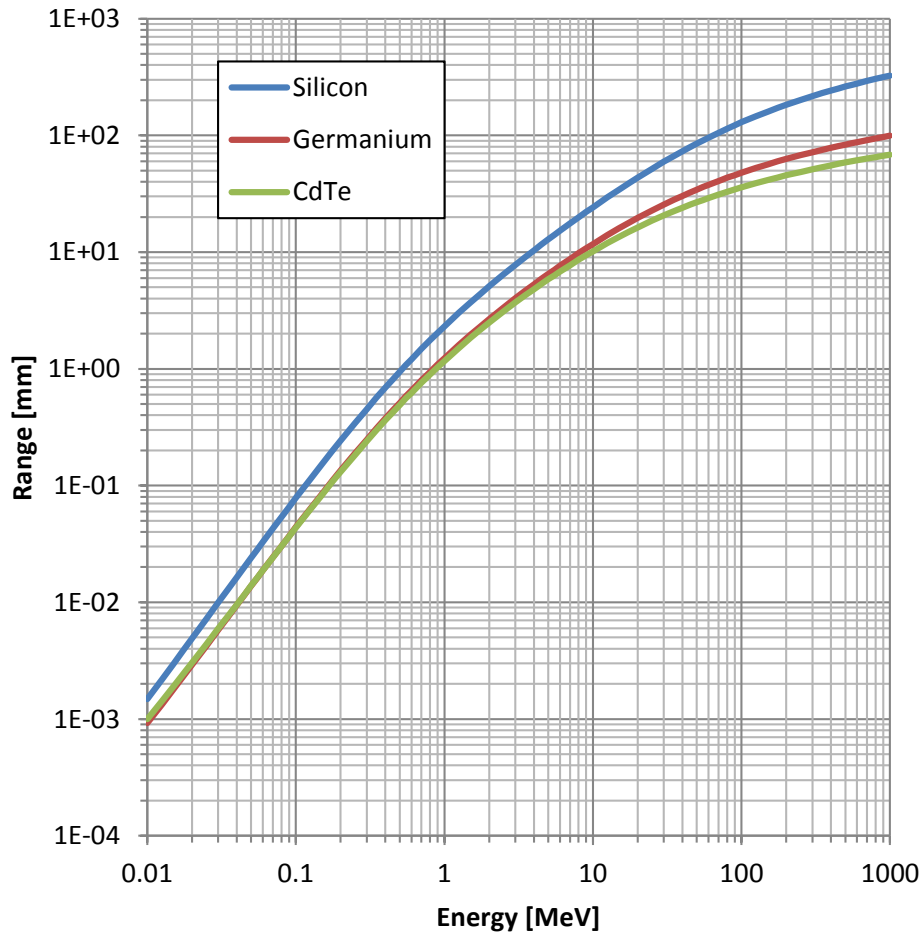
Figure 4. CSDA electron range in silicon, germanium and CdTe calculated in ESTAR [6].

All charged particles also lose their energy by radiative processes in the form of bremsstrahlung or electromagnetic radiation arising from the acceleration. The intensity of the bremsstrahlung is proportional to m^{-4} and, therefore, protons radiate with the intensity roughly 10^{13} times lower that electrons moving with the same velocity [4]. Radiative losses are generally most important for high electron energies and for absorber materials with large atomic number. In case of silicon that means electron with energies above 10 MeV as depicted in Fig. 5.
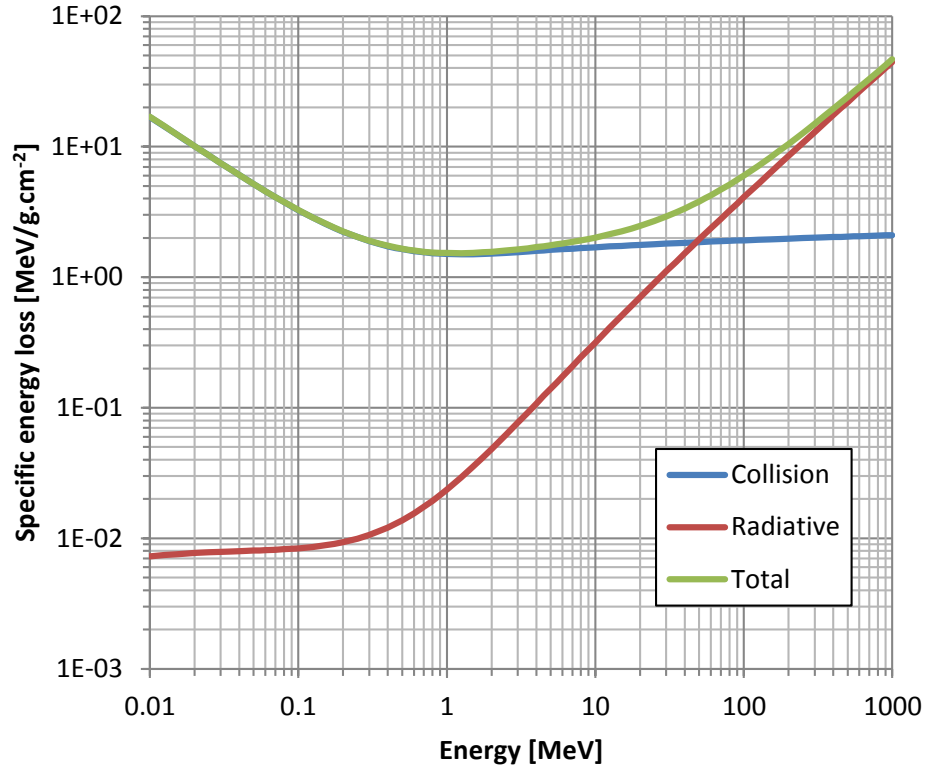
Figure 5. Electron specific energy loss in silicon caused by collisional and radiation losses calculated in ESTAR [6].

2.1.3 X-ray and gamma photons

Contrary to the charged particles photons have no charge and therefore cannot interact with the target material by means of Coulomb force. There are a large number of known interaction mechanisms but only three major types play an important role in radiation measurement: photoelectric effect, Compton scattering and pair production. For the description of these effects is convenient to use corpuscular description of electromagnetic radiation.

Photoelectric effect

In the interaction of low energy photons (up to 100 keV) the most probable scenario is that the whole photon energy is absorbed by an atomic electron with the subsequent ejection of the electron from one of the atom bound shells. The energy of the emitted electron is given by:

$$E_e = E_0 - E_b \qquad (2)$$

where E_e is the energy of the ejected electron, E_0 is energy of the incident photon and E_b is the binding energy of the electron in the atom.

Vacancy after the emitted electron is filled through capture of a free electron from the target material or from the upper shells of the atom. The energetic difference is consequently irradiated in the form of one or more characteristic X-ray photons. If the vacancy is formed in one of the inner atoms shells the characteristic X-ray photons can be absorbed again with the consequent release of the electron from the bound shell. This so called Auger electron will have energy characteristic to the material of the target [4].

Compton scattering

The probability of Compton scattering is increased for photons with energies above 10 keV. In this case photon hit the loosely bound electron from the outer shell of the atom transferring part of its energy and changing the original direction (see Fig. 6).
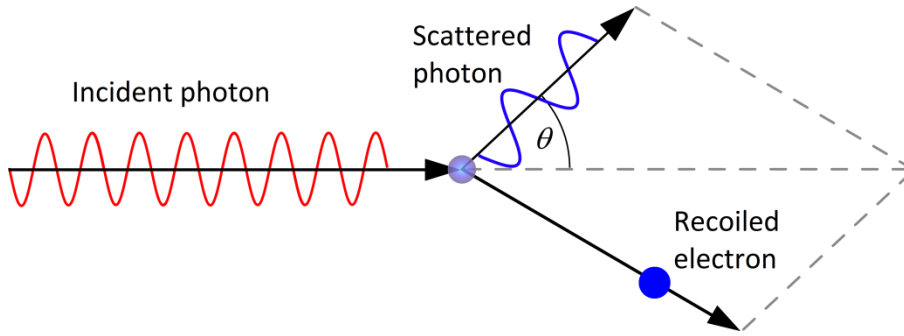
Figure 6. Scheme of the Compton scattering.

The kinematics of the energy transfer is described by the following equations:

$$E_\gamma = E_0[1 + (E_0/m_e c^2)(1 - \cos\theta)]^{-1} \qquad (3)$$

$$E_e = E_0 - E_\gamma = E_0 \left[\frac{(E_0/m_e c^2)(1 - \cos\theta)}{1 + (E_0/m_e c^2)(1 - \cos\theta)} \right] \qquad (4)$$

where E_0 is energy of the incident photon, E_γ is energy of recoiled photon, E_e is energy of electron, m_e is electron mass, c is speed of light and θ is angle between incident and recoiled photons [4]. From the Eq. (4) one can see that the maximum photon energy is lost in direct collision, where $\theta = 180°$:

$$E_e^{max} = E_0 - E_\gamma = \frac{E_0}{1 + m_e c^2/2E_0} \qquad (5)$$

Pair production

Gamma photons with energy greater than 1.022 MeV (twice the rest-mass energy of an electron) may interact in the field of the nucleus forming an electron-positron pair. All the excess energy goes into kinetic energy shared equally between these two particles. The positron slows down in the material and subsequently annihilates and two photons with energy 511 keV are released. These annihilation photons can interact by Compton scattering or photoelectric effect.

Photon attenuation

The probability of the photon interaction is often expressed with so called linear attenuation coefficient $\mu = \mu_{photoelectric} + \mu_{Compton} + \mu_{pair}$ as a sum of the probabilities of the abovementioned processes. Photon beam attenuation can be described by the following equation:

$$n = n_0 e^{-\mu x} \tag{6}$$

where n_0 is number of incident photons and n is number of transmitted photons in absorber depth x. Energy dependence of the linear attenuation coefficient and his components for silicon are shown in Fig. 1.
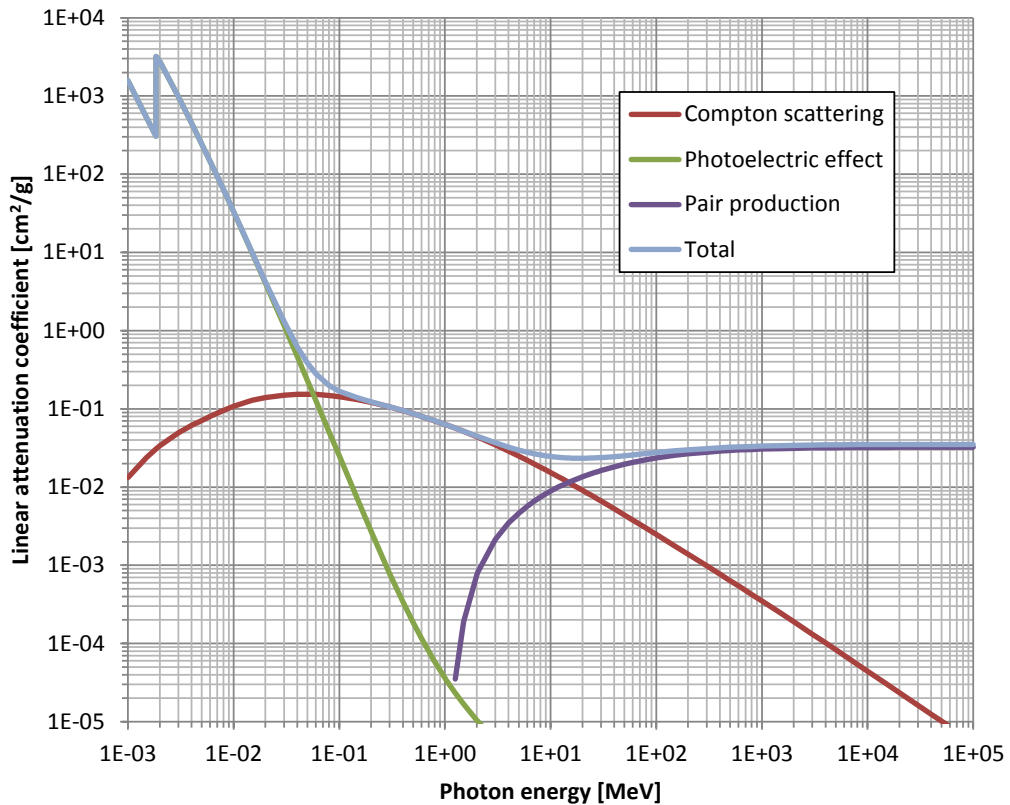
Figure 7. Linear attenuation coefficient of photons in silicon calculated in XCOM [7].

2.1.4 Neutrons

Neutrons have no electric charge and therefore cannot be detected directly by means of the Coulomb force. Neutrons are generally detected through reactions with nuclei of the absorbing material which results in emission of different secondary radiation:

- recoil of the nucleus
- proton
- alpha particle
- fission fragments
- electrons of internal conversion
- gamma photons.

The relative probability of the different type of neutron interaction with the absorbing material strongly depends on neutron energy and thus rather different techniques are used for neutron detection in different energy regions. Neutrons are often roughly divided into two groups. Slow neutrons have the energy below 0.5 eV and fast neutrons are above this energy level (so called cadmium cut off energy) [4].

Slow neutrons

Slow neutrons often interact by elastic scattering with the absorber nuclei but because of the small kinetic energy this process cannot be used for the detection. However, this process brings slow neutrons in the thermal equilibrium with the absorber material. Neutrons in thermal equilibrium are referred as thermal neutrons and at room temperature the corresponding energy is 25 meV. Thermal neutrons have often much larger effective neutron absorption cross section for a given nuclide and therefore can be detected more efficiently. Sometimes a class of epithermal neutrons is defined for neutrons with kinetic energy from 1 eV to 10 keV [8].

Fast neutrons

The probability of neutron absorption is decreasing rapidly with increasing neutron energy. Therefore, for fast neutrons, with energies greater than approximately 1 MeV, elastic scattering is often used for the neutron detection. The most efficient material for this process is hydrogen (or hydrogen rich material) because the neutron can lose up to all its energy in a single collision. In each scattering process the neutron energy is lowered to the energy region of slow neutrons where absorption reactions become more probable [9].

Neutron converter materials

Neutrons are not directly detectable for most of detectors. Therefore, almost every type of neutron detector involves the combination of a target material designed to convert efficiently neutrons to the secondary radiation to be detected with one of the conventional radiation detectors. Some examples of the materials used as neutron converters and corresponding nuclear reaction are mentioned below [10].

^{10}B(n,α) - heavy charged particle production

$$n + {}^{10}B \rightarrow \alpha \ (1.78 \ \text{MeV}) + {}^{7}Li^* \ (1.01 \ \text{MeV}) + \gamma \ (0.48 \ \text{MeV}); \quad 94\%$$

$$n + {}^{10}B \rightarrow \alpha \ (1.47 \ \text{MeV}) + {}^{7}Li \ (0.84 \ \text{MeV}); \quad 6\%$$
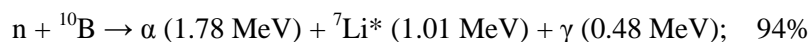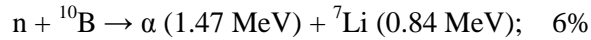
Thermal neutrons capture cross section[1] (see Fig. 8): σ (25 meV) = 3842 b.
The natural boron has 19.8% abundance of ^{10}B.

^{6}Li(n,α) - heavy charged particle production

$$n + {}^{6}Li \rightarrow \alpha \ (2.05 \ \text{MeV}) + {}^{3}H \ (2.73 \ \text{MeV})$$

Thermal neutrons capture cross section (see Fig. 8): σ (25 meV) = 940 b.
The natural lithium has 7.40% abundance of ^{6}Li.

^{3}He(n,p) - heavy charged particle production

$$n + {}^{3}He \rightarrow p \ (0.57 \ \text{MeV}) + {}^{3}H \ (0.19 \ \text{MeV})$$

Thermal neutrons capture cross section (see Fig. 8): σ (25 meV) = 5320 b.
It is commercially available but very expensive material.
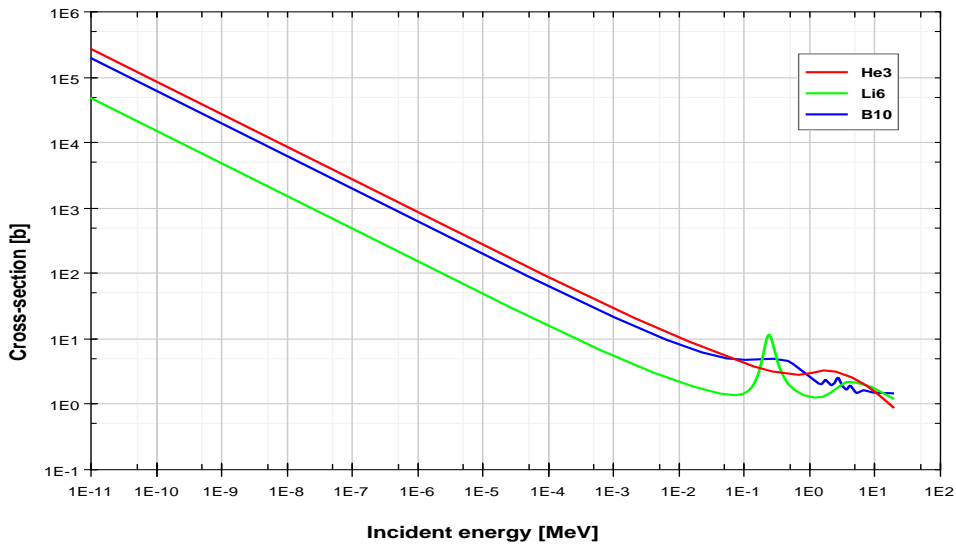
Figure 8. Neutron capture cross sections of ^{3}He, ^{6}Li and ^{10}B [11].

^{113}Cd - gamma photon production

$$n + {}^{113}Cd \rightarrow {}^{114}Cd + \gamma \ (0.56 \ \text{MeV}) + \text{conversion electron}$$

Thermal neutrons capture cross section (see Fig. 9): σ (25 meV) = 20743 b

---

[1] Expressed in barns: 1 b = 10^{-28}m^2
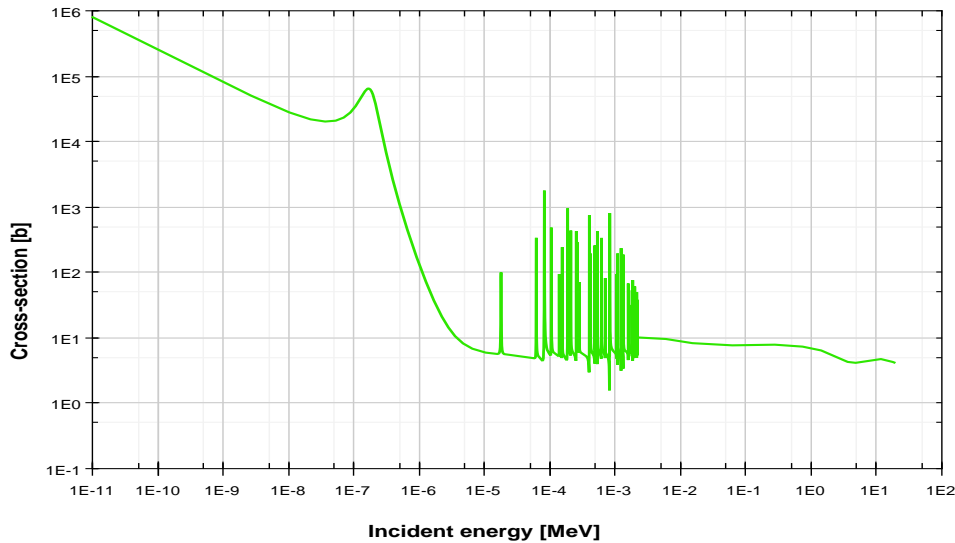
Figure 9. Neutron capture cross section of [113]Cd [11].

Reactions resulting in heavy charged particle production are usually much more attractive for neutron detection. Contrary to the gamma rays, heavy charged particles are detected directly and their energy is high enough to allow discrimination of gamma ray background usually present in neutron fields.

2.2 Semiconductor pixel detectors

The most widely used detectors of this type today are based on silicon or germanium[2]. The reason is that these materials are, due to extensive research in semiconductor junctions as electronics components, well explored and also the production technology of pure monocrystals is well known. The basic characteristics of pure (intrinsic) silicon and germanium are shown in Tab. 1.

Silicon (Z = 14) is usually used for heavy charged particle (protons, α particles...) and low energy photon detectors. The advantage of silicon is wide energy gap and relatively high resistivity even at room temperature.

Germanium with atomic number Z = 32 can be advantageously used for high energy photon detection. Technology of producing large and high purity germanium monocrystals is widely developed at present. From the properties listed in Tab. 1 results the necessity of cooling germanium detectors to increase the resistance of the crystal and decrease the thermal current and noise. Commonly liquid nitrogen (T = 77 K) cooling is used.

---

[2] Usage of the novel high Z detector materials like GaAs, CdTe, HgI, etc. is still rare.

Intrinsic semiconductor	Si	Ge
Atomic number Z	14	32
Mass number A	28.09	72.60
Density (300 K)	2330 kg.m^{-3}	5330 kg.m^{-3}
Atomic density	4.96E+28 m^{-3}	4.41E+28 m^{-3}
Relative dielectric constant	12	16
Energy gap E$_g$ (300 K)	1.115 eV	0.665 eV
Energy gap E$_g$ (77 K)	1.154 eV	0.730 eV
Electron density n$_i$ (300 K)	1.5E+16 m^{-3}	2.4E+19 m^{-3}
Intrinsic electric resistivity r$_i$ (300 K)	2.3E+3 Ωm	0.47 Ωm
Electron mobility μ$_e$ (300 K)	0.135 m^{2}V^{-1}s^{-1}	0.39 m^{2}V^{-1}s^{-1}
Hole mobility μ$_d$ (300 K)	0.048 m^{2}V^{-1}s^{-1}	0.19 m^{2}V^{-1}s^{-1}
Electron mobility μ$_e$ (77 K)	2.1 m^{2}V^{-1}s^{-1}	3.6 m^{2}V^{-1}s^{-1}
Hole mobility μ$_d$ (77 K)	1.1 m^{2}V^{-1}s^{-1}	4.2 m^{2}V^{-1}s^{-1}
Energy for electron-hole pair generation w (300 K)	3.62 eV	-
Energy for electron-hole pair generation w (77 K)	3.76 eV	2.96 eV

Table 1. Characteristics of intrinsic silicon and germanium [12].

As consequence of high thermal stimulated current[3], which for a silicon plate of 1 cm^2 area becomes about four orders of magnitude greater than the effective signal[4], is it not possible to use an intrinsic semiconductor as a radiation detector. For germanium the situation is even about several orders of magnitude worse. The only known and viable method enabling an effective decrease of thermal stimulated current of semiconductor detectors is using the properties of the P-N junction.

2.2.1 Doped semiconductors

Silicon and germanium belong to group IV of the periodic table of elements. Both materials crystallize in a cubic crystal structure where their four valence electrons mediate covalent bonds between nearby atoms. In such a crystal at non-zero temperature, part of its thermal energy is given to the electrons. This energy can be large enough to allow valence electrons to overcome the energy gap from valence to the conduction band. Thus electron-hole pairs are created which, as charge carriers, can move in the crystal by application of an external electric field causing the thermal electric current.

If the crystal contains a small concentration (relatively less than 10^{-6}) of elements from V. group of periodic table of elements, there atoms can replace the semiconductor atoms at some places. Four out of five donor valence electrons mediate the covalent bonds with surrounding atoms. The remaining fifth electron is only weakly bonded to the atom of impurity and needs only a small amount of energy to reach the conduction band. However in this case, no corresponding hole is created. This small energy is with high probability obtained by thermal excitation. Because the density of impurities is in most cases much larger than concentration of thermal excited intrinsic electrons, almost all electrons in conduction band comes from ionized donors. Larger then intrinsic electron density in conduction band increases the recombination speed and as a result the balance of electron and holes densities is altered. As a consequence, the electron density in the

---

[3] For silicon plate of d = 1 mm thickness, and bias voltage V = 10 V is the current density of thermal stimulated current i$_0$ ≥ 1 × 10^{-3} Acm^{-2}.
[4] Mean value of the signal current is for the same plate (Si, d = 1mm, V = 10V) about 5 × 10^{-7} A.

conduction band exceeds the hole density in the valence band by several orders of magnitude. As the majority charge carriers are electrons and minority holes, this type of doped semiconductor is called N-type semiconductor.

On the contrary, P-type semiconductors are doped by atoms from group III of the periodic table of elements (acceptors). Atoms of trivalent impurities are to the atoms of the medium bounded only by three instead of four covalent bonds. The fourth, unsaturated atomic bond represents a hole with similar parameters as the temperature induced hole carriers. These acceptor vacancies are occupied by temperature excited electrons from the conduction band after which the positive charged holes remain in the valence band. This again leads to an unbalance of charge carriers when the hole density in the valence band is much greater than the electron density in the conduction band.

2.2.2 P-N junction

A P-N junction is forming by changing the type and concentration of impurities along the crystal (e.g. by diffusion of acceptors on the wafer of N-type semiconductor). Suppose sufficient temperature, so that all dopes in semiconductor are ionized. At the P-type semiconductor the concentration of the holes predominates electron concentration by several orders, while at N-type semiconductor the situation is reversed. At the junction area, the gradient of concentration of charge carriers causes the diffusion of holes to the N-type region and electrons to the P-type side. For that reason, at the junction area is the lack of movable charge carriers, but there are still unmovable ionized donors and acceptors, fixed in crystal lattice. As a result, the electric field of high intensity in direction of potential drop arises. This field affects against the charge carriers diffusion until the current density caused by the diffusion is compensated by drift current density and the equilibrium was established (see Fig. 10).
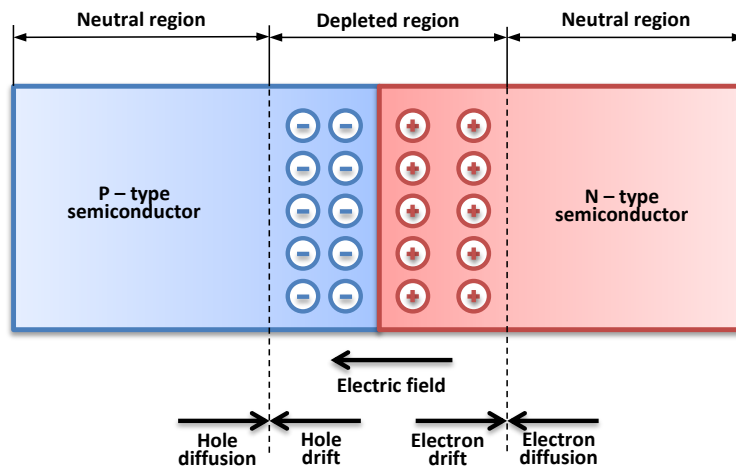
Figure 10. A P–N junction in thermal equilibrium without bias voltage applied. The electric field is shown on the bottom, the electrostatic force on electrons and holes and the direction in which the diffusion tends to move electrons and holes.

If we have the intention to use P-N junction for ionizing radiation detection, it is necessary to polarize it in so-called reverse direction. In this case, the positive polarity of

applied voltage is on N-type side and negative polarity is on P-type region. In this way applied voltage causes expansion of depleted area (area without movable charge carriers) suitable for detection. Electron-hole pairs formed in depleted area by ionizing radiation interaction than create the current (respectively charge) signal, which can be amplified and measured. Through the reverse polarized P-N junction only minority carrier current flows. If we achieve, that this reverse current will be several times less than the signal current, than the reverse polarized P-N junction will have the character of spectrometric detector with sensitive volume of depleted area size.

2.2.3 Position sensitive detectors

The development of the new detectors lies in the domain of high energy physics and related fields. At new colliders such as the LHC (Large Hadron Collider) at CERN[5], new detectors are required for monitoring the tracks of primary and secondary particles produced by colliding particle beams. The task of tracking detectors is to resolve the various particle tracks and to assign them to primary or secondary vertices. For this purpose several types of position sensitive detectors have been developed.

Strip detectors

First of all are the micro strip detectors. These devices consist of thin (usually about 300 μm thick), high resistivity silicon sensors segmented into narrow strips with pitch in the order of tens of microns. Reverse biased P-N junctions structures, formed between strips and the rear side of the detector, determine one dimensional coordinate of the crossing particles. The charge generated from individual events is spread between nearby strips due to drift and diffusion. With analog read-out electronics, the center of the charge distribution can be calculated. In this manner it has been possible to reach excellent spatial resolution down to 5 μm [13]. The major setback of this type of detector is that multiple tracks cannot be resolved unambiguously.

Pixel detectors

Advances in CMOS[6] technology (1 μm[7] CMOS technology became standard in the early 90s) enabled to construct two-dimensional matrices of P-N junctions (diodes) at micrometer scale. Further improvement in CMOS technology enabled the possibility of integrating the read-out logic unit close to the detector elements. Following the nomenclature used for CCDs[8] and optical devices the term pixel detector is used for such devices. Each detecting element from the matrix is composed of one diode attached to its read-out electronics (with dimensions equal to the detection element). The concept of active pixel detectors consists in having the electronics cell equally dimensioned and close to the corresponding pixel. Thanks to the proximity between the detection and read-out parts of the device, the capacitance of the collection electrode can remain very small and the signal to noise ratio high. Further, it is also possible to implement a number of

---

[5] European Organization for Nuclear Research
[6] Complementary Metal Oxide Semiconductor
[7] 1 μm corresponds to the transistor gate length and is a measure for the electronics component miniaturization.
[8] Charge Coupled Device

important logical features such as data selection (zero-suppression). Several possibilities of realizing pixel detectors have been developed.

Monolithic pixel detectors

In monolithic pixel detectors (see Fig. 11) electronics circuitry is integrated with the detecting elements onto the same substrate. This result in a more robust and thinner device (reducing energy loss and scattering inside a complex high energy particle detector) compared to the hybrid approach (see below).
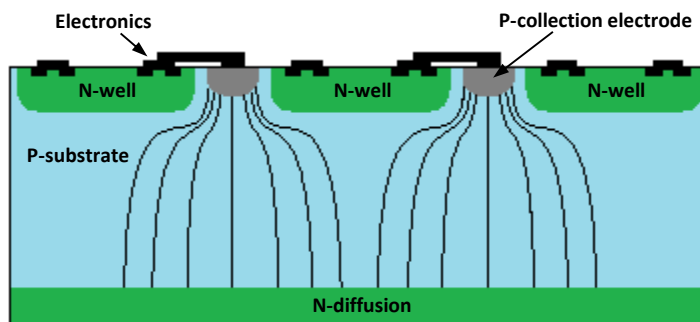
Figure 11. Cross sectional view of a part of monolithic pixel detector.

Silicon on insulator (SOI)

A different processing technique is called silicon on insulator (SOI). An insulating layer separates the active detector part from the read-out electronics which are embedded in a thin silicon layer (see Fig. 12). The high resistivity substrate below the oxide layer may be used as the detection volume. This reduces the drain and source diode capacitance making the electronics faster for a given power consumption. Another advantage of SOI detectors is radiation tolerance. The drawback of this technology is that design requires nonstandard processing (double-sided processing, P implants underneath the oxide layer of the SOI wafer) which expensive manufacturing costs.
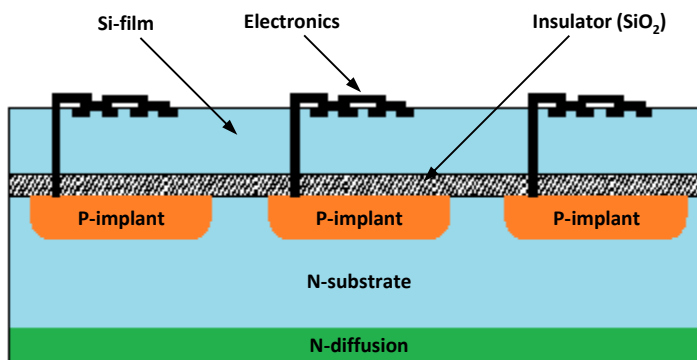
Figure 12. Cross sectional view of a segment of a pixel detector in SOI technology.

Hybrid pixel detectors

In a hybrid pixel detector the read-out chip and the sensor are manufactured separately. Each of the two parts of the detector have a matching matrix of spot electrodes which are

16

connected together mechanically and electrically through small connecting spherical bonds (usually made out of solder or indium with diameter of about 20 μm) as depicted in Fig. 13. This procedure is called bump-bonding process and offers the possibility of optimizing the read-out electronics and the sensor independently. The possibility of choosing the sensor material makes this approach highly attractive in medical imaging applications. GaAs or CdTe can be used instead of silicon which, being a low Z material, has low absorption efficiency for X-rays with energies greater than about 20 keV [13]. It is important to note that only the hybrid approach allows the design of the pixel read-out in standard CMOS technology which is a major consideration in view of processing costs.
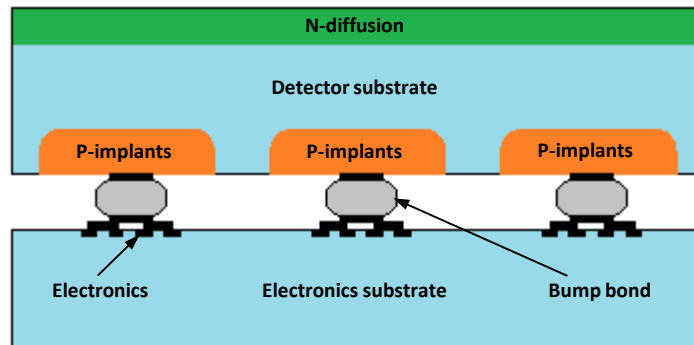
Figure 13. Cross section of a part of a hybrid pixel detector.

This thesis concentrates on the Medipix2 pixel detector which is designed as a hybrid device in standard CMOS technology.

3. Methods of evaluation of mixed radiation fields with pixel detectors

Measurement of the mixed radiation fields is rather complicated task. For most accurate field characterization it is necessary to follow individually the interaction of each radiation quanta. Below are the most common particle characteristics of interest:

- Position and direction
- Energy
- Time of arrival
- Particle type

Different interaction mechanisms for different energy ranges of the incident particles makes impossible to find ideal material and technique to characterize precisely complex radiation fields. However the possibility to use different sensor materials and advanced data processing techniques makes the hybrid pixel detectors good candidate to universal radiation detector for wide range of possible applications.

The Medipix2 detector [1] used in this thesis is one of the available options. The extensive development of the many collaborating institutes [14] makes it an easy to use and rather universal device. It can be operated in two modes: the tracking mode and the counting mode. Both modes are based on simultaneous exposure of all the 256 x 256 pixels to the incoming radiation quanta, during a well-defined, adjustable exposure time. A very large dynamic range can be achieved with this unique device, as will be explained later.

3.1 Medipix2 pixel detector

The hybrid pixel detector Medipix2 (see illustration in Fig. 14) is the successor of the Medipix1 photon counting chip. Fast progress of CMOS technology enabled enhanced functionality of the pixel cell while at the same time providing a significant reduction in pixel size. The chip is designed and manufactured in six-metal 0.25 µm CMOS technology. It was successfully bump bonded to sensors from Si, CdTe and GaAs materials with thicknesses from 200 µm to 2 mm.

18
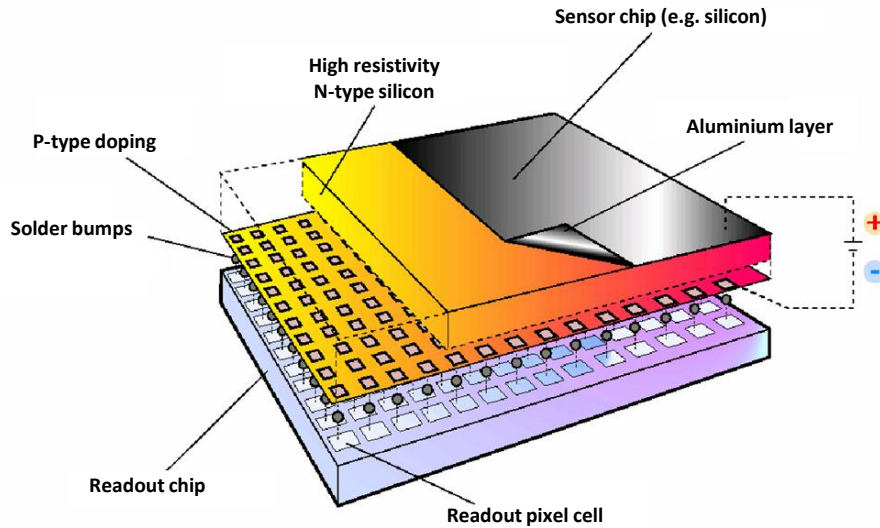
Figure 14. Schematics of the Medipix2 electronic chip connected via bump bonds to sensor chip [14].

There are two versions of Medipix2 chip. This thesis works with the so called MXR version of the chip. The main features of the chip are following:

- 256 × 256 square pixels of 55 μm in size.
- Sensitive area of ~2 cm² (87% of chip).
- The chip is designed to accept either positive or negative charge input in order not to restrict the choice of the sensor material (Si, GaAs, CdZnTe...).
- Maximum count rate is above 100 kHz per pixel
- Each pixel contains amplifier, two discriminators and a 14-bit counter. It is possible to select a window in energy. Upper and lower thresholds can be adjusted pixel wise with 3-bit precision.
- Support of the 32-bit parallel and serial read-out.
- Designed as 3-side tillable for feasible large area coverage.

3.1.1 Medipix2 peripheral circuitry

The Medipix2 chip has been designed to minimize the dead area between chips when covering large areas by butting several chips together. This is achieved by placing the periphery circuits at the bottom of the chip (see Fig. 15).

The non-sensitive area in the other three edges is minimized to less than 50 μm, so the various configurations of the butted chips can be made. The complete chip dimension is 16120 μm × 14111 μm. The sensitive area is composed of a matrix of 256 × 256 pixels of 55 μm × 55 μm size each resulting in a detection area of 1.982 cm² which represents 87% of the entire chip area. The non-sensitive area at the bottom of the chip is 2040 μm × 14111 μm which is 12.65% of the total chip area. There are 127 input/output

pads in this region to wire bond the chip to the carrier PCB[9]. Chip has three independent power supply inputs at 2.2 V and the static power consumption is about 500 mW [1].
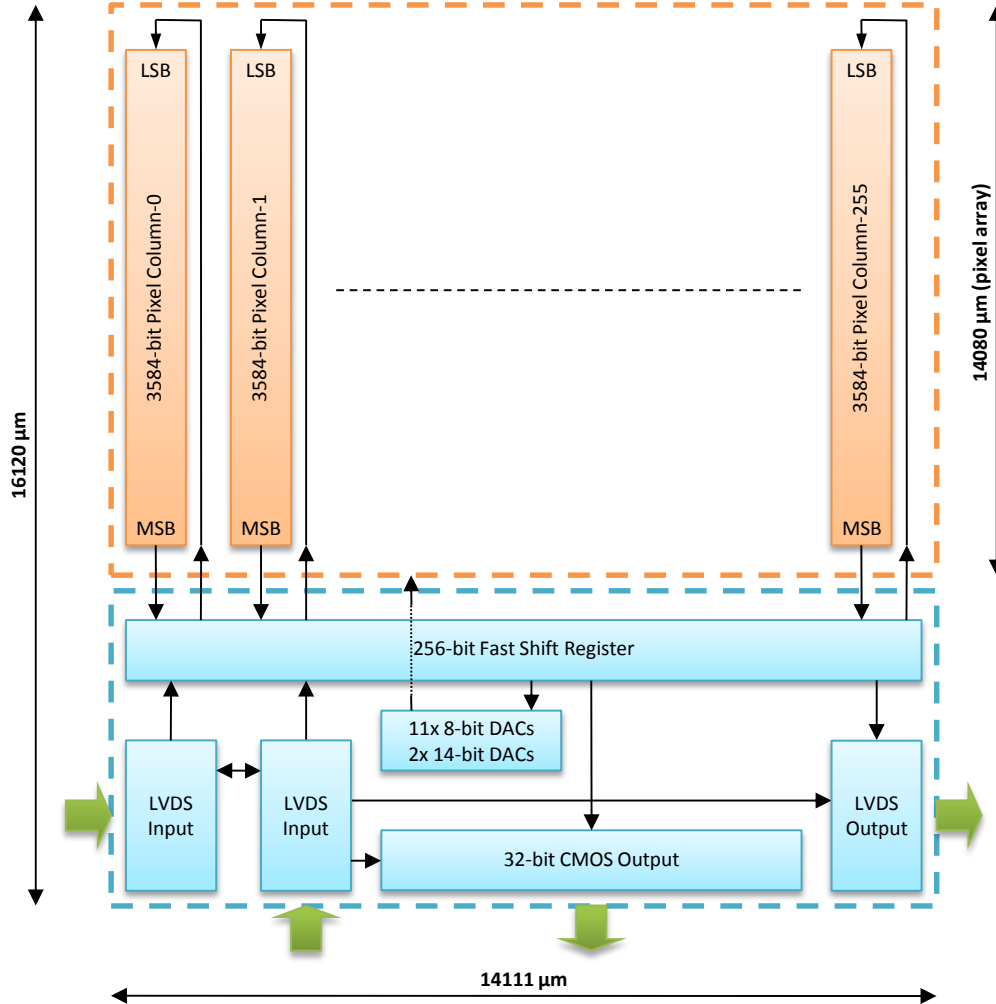
Figure 15. Medipix2 surface plan and block diagram.

3.1.2 Medipix2 pixel cell architecture

The Medipix2 cell occupies an area of 55×55 μm^2 and consists of 529 transistors. It can be divided into an analog and a digital part as shown in Fig. 16. Both the analog and digital circuitry has been designed to operate with independent 2.2 V power supplies. The static analog power consumption is about 8 μW per pixel.

---

[9] Printed Circuit Board
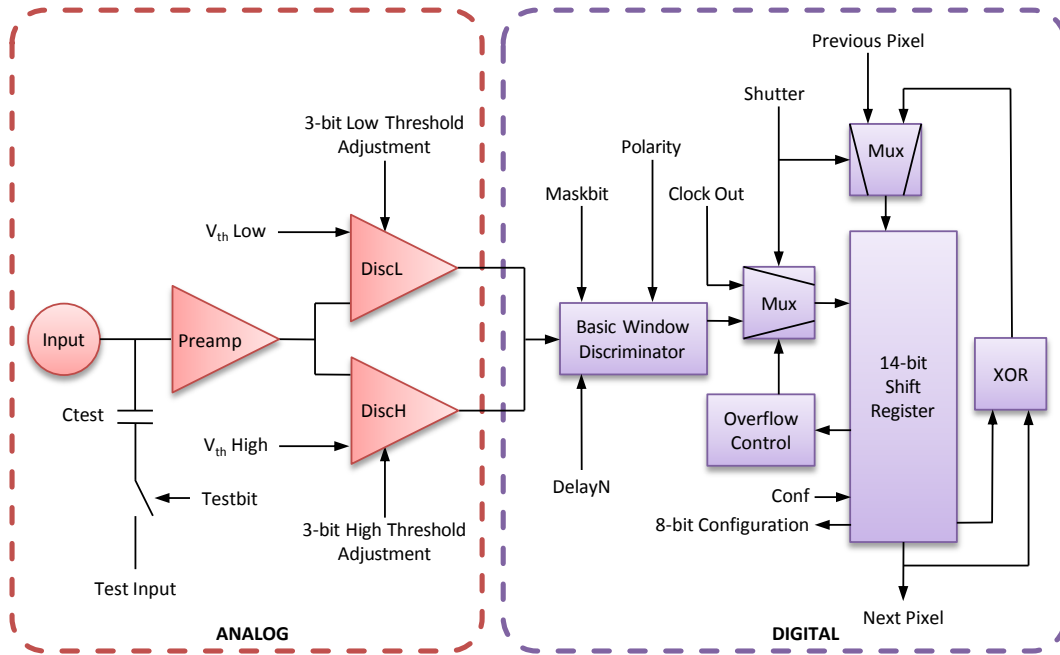
Figure 16. Medipix2 pixel cell block diagram. In red the analog part of the pixel and in violet the digital side.

The analog part consists of a charge preamplifier with DC leakage current compensation, a test capacitance, and two branches of identical discriminators. The octagonal bump bond opening used for connection with sensor is placed on top of the analog side and has a diameter of 20 μm. The digital side contains the Basic Window Discriminator (BWD) and the 14-bit shift register and the overflow control logic. The pixel has two different working modes depending on the CMOS input *Shutter* state.

Data acquisition mode
When the *Shutter* signal is low the pixel turns to data acquisition mode. In this case the shift register works as a pseudo-random counter of 14-bits with dynamic range of 11810 counts. The output of the basic window discriminator logic is used as clock for this counter. When a charged particle interacts in the sensor depleted area it deposits a charge which drifts towards the collection electrode. This charge is then amplified and compared with two different thresholds. The comparators outputs are than connected to the BWD. This logic does the discrimination between two input signals and can work in two modes:

- Single mode is set when the high threshold level (V_{th} High) is set lower than the low threshold (V_{th} Low). In this case the output pulse is generated when a signal from the low discriminator is received. A high discriminator signal is in this case ignored.
- Energy window mode is set when V_{th} High is higher than V_{th} Low. An output pulse is produced only when the signal from the low discriminator is obtained while the high discriminator remains quiet.

Every pulse coming from the discriminator logic increments the counter value by one unit. After the maximal value is reached the overflow control logic stops the counter.

Each pixel can handle count rates above 100 kHz depending of the settings of the internal signal shaping. Read-out is performed after exposure to avoid dead time.

Readout/settings mode

When the *Shutter* signal is high the pixel readout/setting mode can be initialized. In this mode the 14-bit shift register of each pixel is connected to the next and previous to form a 3584-bit shift register as shown in Fig. 15. Communication between the pixel matrix and the IO logic is carried out through the 256-bit FSR. When the *Shutter* signal is high an external clock can be used to shift the data from pixel to pixel. This mode is used both for setting the eight pixel configuration bits and for reading the 14-bit counter information.

3.2 Medipix2 readout interface

To transfer the data from the Medipix2 chip to the computer and to control the chip functionality a special readout interface is needed. Several read out interfaces have been already developed by members of the Medipix collaboration. The MUROS2 read out board [15] is an FPGA[10] based interface which is flexible and fast (about 100 Mbit/s) and gives the possibility of performing all kinds of operations on the chip. PRIAM readout interface uses the parallel bus of the Medipix2 chip to read five chips in less than 300 µs [16]. Work on this thesis was done using the USB based readout interface.

3.2.1 USB readout interface

The USB readout interface was developed as my master thesis project [12], [17]. In contrast to the other development directions the aim of my work was to develop a fully independent and easy to use interface which integrates the entire necessary detector support including bias voltage power supply into one compact device (see Fig. 17).

The USB bus was chosen because it provides not only the communication lines but also the power line (5 V and up to 500 mA) and it is widely used in all computer equipment. Main features of developed USB interface are:

- Serial readout speed: 4 frames per second
- Microprocessor controlled measurement
- Fully USB powered (total power consumption is below 2 W)
- Integrated source of detector bias (5 - 100 V)
- Back-side electrode monitoring for triggering purposes
- I/O connector for external triggering support (input, output) and coincidence applications
- Ability to flash firmware via USB connection
- Pixelman software compatibility (see section 3.3)
- Small dimensions of the interface box 20 mm × 50 mm × 60 mm

---

[10] Field Programmable Gate Array
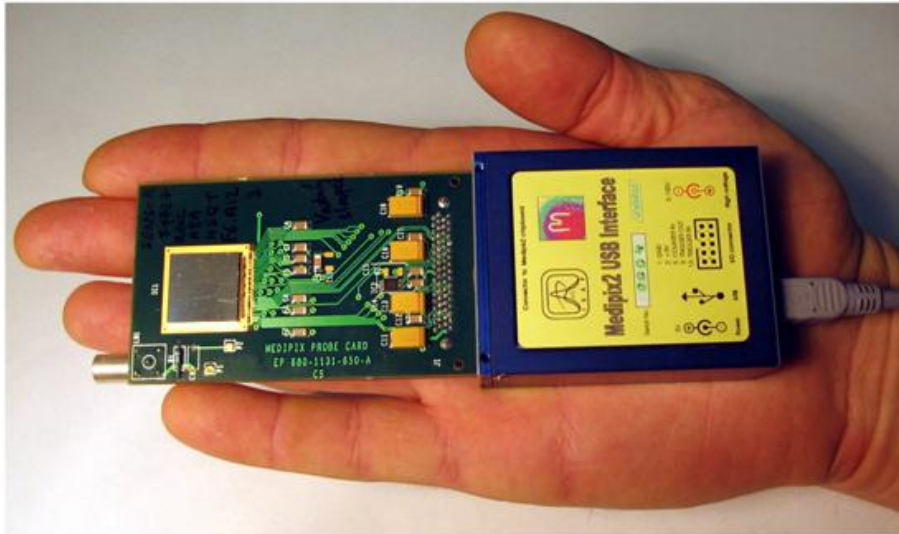
Figure 17. Image of the Medipix2 chip mounted on the carrier PBC connected to the USB readout interface box.

3.2.2 USB Lite readout interface

The success of the small and easy to use USB interface concept leads to the further miniaturization. This was achieved by accommodating the Medipix2 detector chip on the same printed circuit board as the USB readout interface. This so called "USB Lite" interface [18] is fully compatible with the previous version of the system and the size is comparable to the commonly used USB flash memories (see Fig. 18). Compactness of the system opens up new possibilities in applications like personal dosimetry, medical imaging, etc.

Figure 18. USB Lite interface is the step in further readout interface miniaturization where dimensions of the whole setup has been reduced to 15 mm × 60 mm (25% out of it is the active area of the Medipix2 detector).

3.2.3 FITPix readout interface

Availability of the USB2.0 circuits allows the development of a significantly faster readout interface while the advantages of the previous generation remain preserved. The interface consists of a FPGA, USB 2.0 interface chip, DAC, ADC and a circuit which generates bias voltage for the sensor. Presence of the FPGA provides direct access to the hardware resources enabling fast hardware triggering possibility (70 ns delay) necessary for many application tasks like synchronized operation of multiple devices. Three modes of hardware trigger have been implemented:

- Hardware trigger starts the measurement
- Hardware trigger terminates the measurement
- Hardware trigger controls measurement fully

The readout speed of the FITPix interface is up to 90 Mbit/s what is about 90 frames per second with single Medipix2 chip. The power consumption of the interface itself is 775 mW, thus it can be fully powered from the USB bus including single Medipix2 chip. Current firmware supports up to 12 chips in the chain (external power supply is required in this case). Whole interface is accommodated in a box with the same dimensions like its predecessor and also the pin out is compatible [19].

3.3 Pixelman control software

A dedicated software support is essential in order to control and manage complex measurements. Such a multi-platform software package called Pixelman has been developed for acquisition control and data processing with a Java graphical user interface [20].
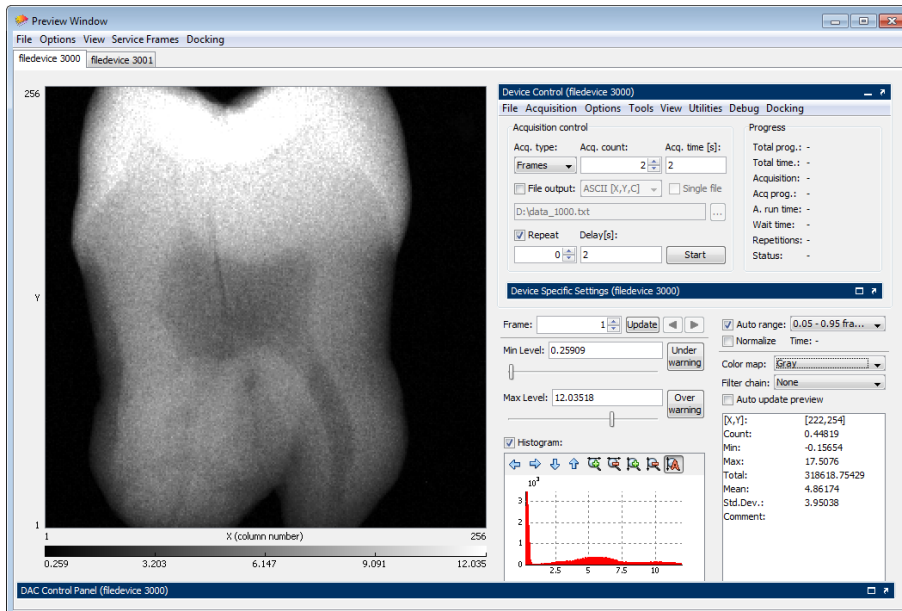
Figure 19. Java graphical user interface of the Pixelman preview and control window. Radiography of a tooth is shown as an example.

The functionality of the original version of Pixelman package [21] has been upgraded and extended to include support for new devices from the Medipix family. The software package can be run on Microsoft Windows, Linux and Mac OS X operating systems. The architecture is very flexible and current functionality can be extended further by an independent plugins in C++, Java or combinations of both (see the block diagram in Fig. 20). The software package can be used locally or as a distributed acquisition system using computers with different operating systems over a local network or the Internet.
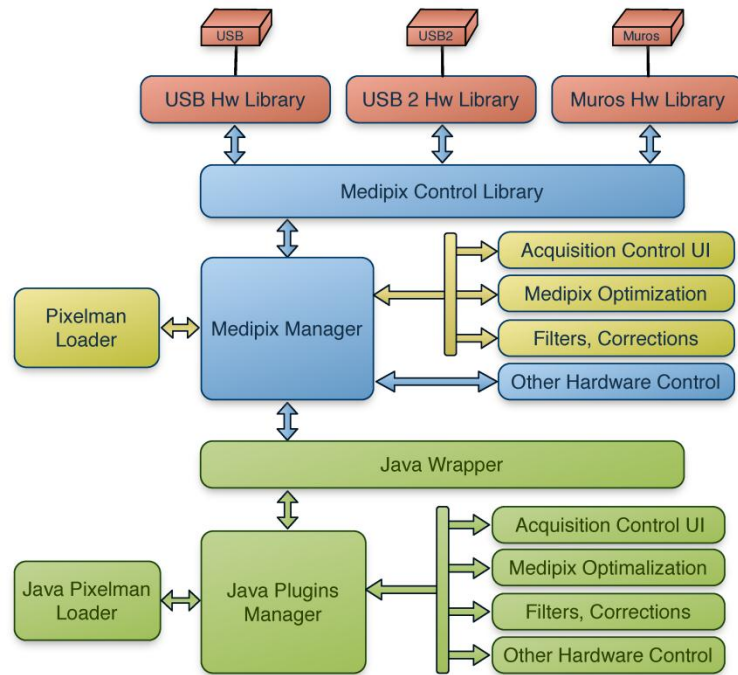
Figure 20. Scheme of the Pixelman software architecture: hardware libraries (red), multi-platform C++ core and plugins (blue), windows plugins (yellow), multi-platform Java core and plugins (green) [20].

3.4 Data acquisition and evaluation for mixed radiation field measurements

In the radiography techniques the task is to measure unknown object properties using known radiation field and detector device (i.e. pixel detector). The task of measurement the radiation field characteristics with pixel detectors is very similar with the difference that in this case the object properties are knows and selected properly to help with the characterization of the unknown radiation field. With the single particle counting Medipix2 detector we have generally two main parameters to tune:

- Acquisition time (from ~10 µs up to tens of minutes)
- Energy threshold (from ~10 keV up to hundreds of keV)

By setting the acquisition time according to the specific radiation field intensity and composition we can operate the device in two data evaluation modes as described below.

3.4.1 Tracking mode

For so called tracking mode the acquisition time has to be set low enough in order to distinguish between individual particle interaction signatures without signal overlapping. In this mode, the signature of particles interacting in the sensitive volume is a track of adjoining activated pixels with different size and shape depending on the type of particles, their energy and their incidence angle. By analysis of these characteristic pixel clusters is possible to distinguish the type of the interaction and particle. This mode provides most information about the surrounding radiation field but very short acquisition times may result in large dead time of the measurement because the data are read out more often (readout time is fixed and given by the used readout interface described in section 3.2).

A set of parameters have to be evaluated for each cluster to characterize the differences in their shapes:

- Area - number of adjacent pixels.
- Height - maximum value of a pixel in the cluster
- Roundness - comparison of a cluster area to the length of its border
- Linearity - consistency of activated pixels in the cluster with straight line
- Width of the straight track - characteristic of a particle ionization power

Low energy threshold

An example of a data from the Medipix2 detector bump-bonded to a 300 µm thick silicon sensor operating in a low energy threshold of ~10 keV is shown in Fig. 21. The low threshold (LT) setting is necessary to record single photons, electrons and MIPs[11]. The different characteristic cluster shapes are clearly distinguishable in Fig. 21. To automatize the particle identification a pattern recognition algorithm was developed allowing the particle identification in a real-time in the Pixelman software [22]. The shape of the cluster depends on the particle energy, incidence angle and on the nature of the interaction in the detector sensitive volume. The six different categories of a characteristic cluster shapes were defined (see corresponding numbers in Fig. 21):

1) Dot – low energy X-rays and electrons
2) Small blob – more energetic photons and electrons
3) Curly track – energetic photons and electrons (MeV range)
4) Heavy blob – energetic particles with low range (alpha particles)
5) Heavy track – energetic heavy charged particles
6) Straight track – energetic light charged particles (MIPs, Muons…)

---

[11] Minimum Ionizing Particles
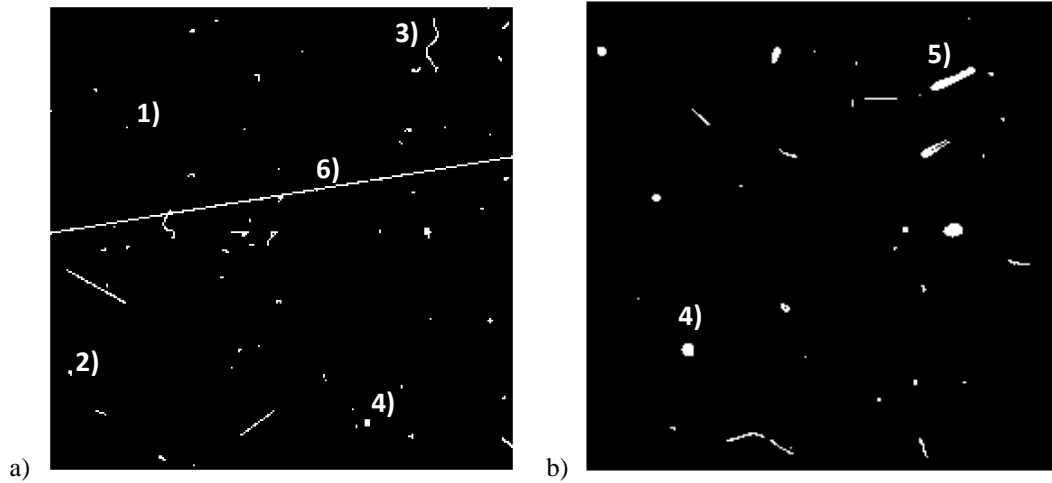
Figure 21. a) Background radiation in the ATLAS experimental cavern in 2008 before any collision period measured with Medipix2 detector with 300 μm thick silicon sensor, low threshold of 10 keV, acquisition time of 100 min. A cosmic muon track (6) is traversing horizontally the 14 mm wide sensor. Two other muon tracks corresponding to non-parallel incidence on the sensor are only covering smaller track lengths. Various traces and tracks of X-ray photons, electrons (including delta-rays along a muon track) are also visible (1, 2, and 3). b) Measurement of neutrons (wide spectrum from 2 – 30 MeV) produced by a cyclotron beam with low threshold of 10 keV and acquisition time of 100 μs. The characteristic comet-like clusters (5), following Bragg law of energy deposition, from protons recoiled to silicon sensitive volume from the PE converter layer above the sensor are observed. Protons recoiled perpendicularly to the sensor surface create circular clusters (4).

Photons are detected indirectly. They can deposit energy through three interactions: photoelectric effect, Compton scattering and pair creation. In each case, they transfer all or part of their energy to electrons or electron-positron pairs, which are detected. Low energy X-rays and electrons will leave dots labeled (1) in Fig. 21a. More energetic gamma rays, X-rays and electrons are observed either as small blobs, labeled (2) in Fig. 21a, or as curly tracks, labeled (3) in Fig. 21a. These types of clusters are commonly classified as signatures of particles with low energy transfer (LETP).

Minimum ionizing hadrons, muons and electrons with the energy higher than energy corresponding to minimum ionization produce continuous long straight tracks, labeled (6) in Fig. 21a. Their clusters are easily recognizable except when they are hitting the sensitive layer perpendicularly and thus activate only a few pixels. To be classified by the pattern recognition algorithm as MIPs, incident particles must create a thin straight track of at least 20 pixels length in the sensor.

Clusters generated by heavy charged non-relativistic particles like low-energy protons, alpha particles and nuclear fragments will typically appear as heavy blobs, labeled (4) in Fig. 21b, or heavy tracks, labeled (5) in Fig. 21b, depending on their energy and incidence angle with respect to the sensitive surface. Cluster types 4 and 5 fall into the category of particles with high energy transfer (HETP).

Neutrons can be detected as secondary HETP either from the conversion layer or directly in the silicon sensor depending on their energy. The layout of the neutron conversion layers is discussed in detail in section 4.3.1.

27

The reliability of the cluster pattern recognition procedure was tested with measurements of alpha, beta, gamma and neutron sources, in proton beams and in their mixed fields [22], [23].

High energy threshold

Particles with high energy transfer as well as neutrons are often accompanied by significant gamma and electron background. This low energy transfer background can be effectively removed by increasing the Medipix2 energy threshold setting. It was experimentally tested that at the energy threshold (HT) level of typically 230 – 300 keV the low energy transfer particles are not counted. This allows measurements with longer acquisition times reducing dead time caused by data readout.

In the same time the characteristic shapes of the particles with high energy transfer are changed significantly. With low threshold settings the energetic tracks are several pixels in width because of charge diffusion during the collection process (see detail in Fig. 22a). In high threshold settings the border pixels of such tracks are not counted anymore because their signal, brought there during the charge diffusion process, is much lower that signal in central pixels of the track, and is below threshold level. Thus the energetic tracks are only one or two pixels in width in HT settings (see detail in Fig. 22b).

a)   b)
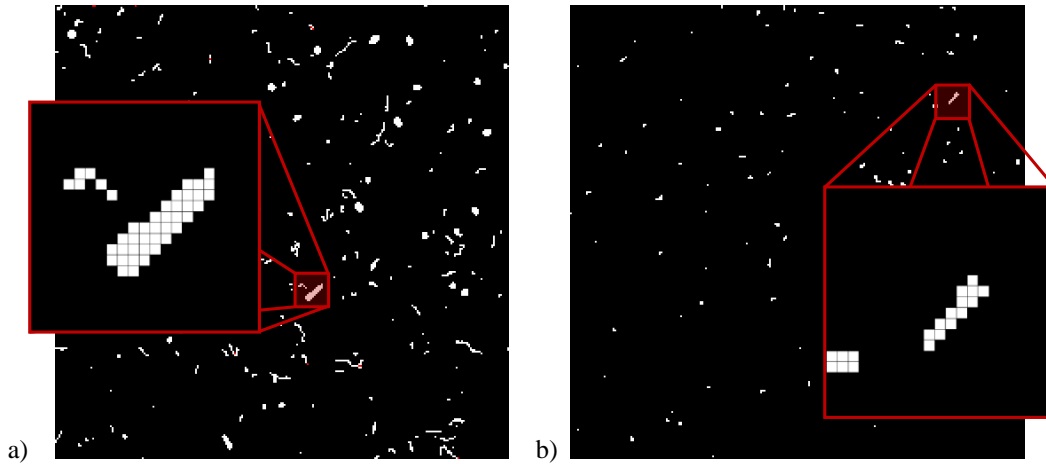
Figure 22. Medipix2 detector with 300 µm thick silicon sensor irradiated perpendicularly by 14 MeV neutrons and accompanying radiation from Van der Graaff accelerator. Detector surface was covered with PE for detection of the recoiled protons. Change of the detection threshold influence the shape of the tracks characteristic to the different ionizing particles. a) Response at low energy threshold of 10 keV, 1 s acquisition time. b) Response at high energy threshold of 250 keV, 5 s acquisition time. Low energy tails of the individual tracks are suppressed making the recoiled proton tracks thinner.

3.4.2 Counting mode

In so called counting mode the overlapping of the individual particle tracks is allowed and the acquisition time length is limited only by the depth of the Medipix2 counters (11810 counts per pixel). That means that in the same radiation field conditions the acquisition time in counting mode can be roughly ~10^6 higher than needed for the tracking mode.

The counting mode is preferred analysis tool in a high intensity radiation environment (practically at rates above 10^5 clusters.cm^{-2}.s^{-1}). In this mode, the number of interactions/hits in individual pixels is counted at selectable threshold settings. This results in a lower limit of energy deposition in the pixel by radiation with the ionizing power exceeding the threshold setting. Calibration of the devices enables the conversion of the individual counts into deposited energy and dose rates (see section 5 for details).

More information can be obtained by placing proper object in front of the detector sensitive volume. In such case the sensitive area of the pixel detector is divided into several regions with different response to the different radiation fields. This approach was also used in the ATLAS-MPX experiment and it is described in detail in section 4. The photograph of the object structure is shown on Fig. 23.
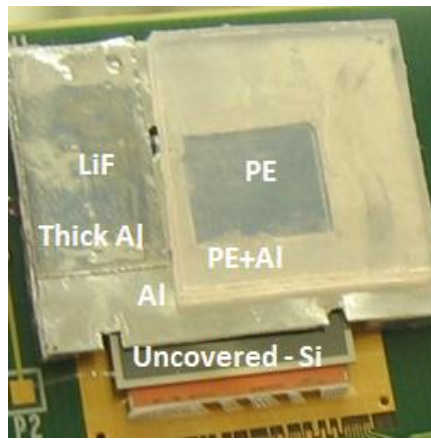
Figure 23. View on the Medipix2 detector with 300 μm thick silicon sensor covered with defined conversion layers prepared for the ATLAS-MPX project.

Low energy threshold
At low threshold settings the Medipix2 detector is sensitive to particles with the low energy transfer. An image of the conversion layers defined in Fig. 23 taken in X-ray field together with corresponding histogram are shown in Fig. 24.
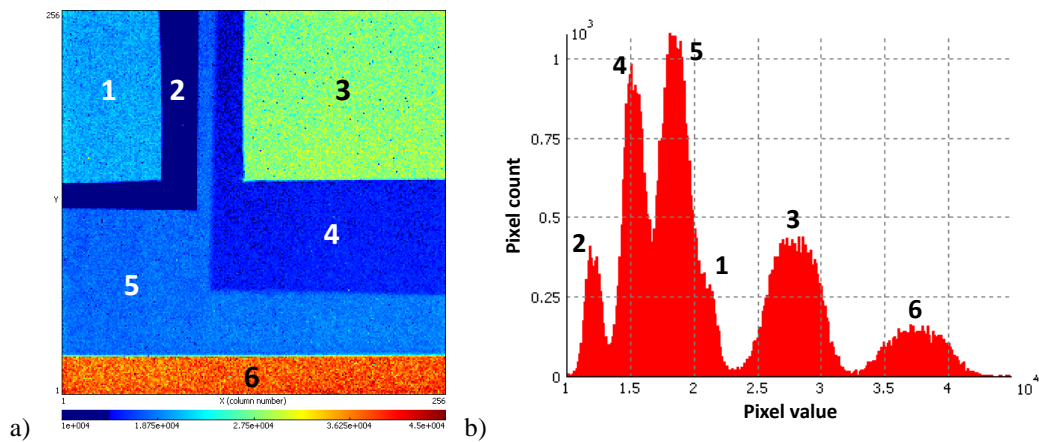
Figure 24. a) Image of the conversion layers on the top of the Medipix2 chip in X-ray field. b) Histogram of the image with numbers showing the response of the different areas of the chip.

The possibility to distinguish different region response at low threshold, as demonstrated in Fig. 24, is limited to specific radiation fields. For example in the field of [252]Cf neutron source the gamma background is so strong that the response of the detector is completely uniform (see Fig. 25a)

High energy threshold

At high threshold value (typically $230 - 300$ keV) the low energy transfer particles (LETP – gamma and X-rays, electrons) do not contribute to the count rate. The detector records only high energy transfer particles (HETP – alpha particles, energetic ions, hadrons) including products of neutron interactions (see Fig. 25b). This HT mode can be effectively used in radiation fields with high fluxes and for neutron detection. Using the adjustable threshold it would be possible to execute threshold scans to determine the LETP and HETP contributions in the stable radiation environment, even at high particle fluxes.

a)   b)
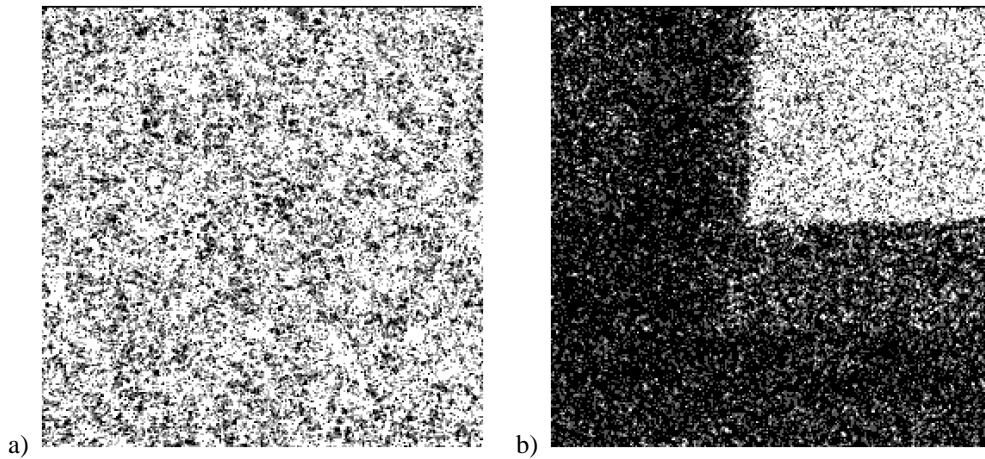
Figure 25. a) Integral image of the Medipix2 device with conversion layer mask exposed to the [252]Cf neutron field. a) At low threshold of 10 keV and 1 s acquisition time b) At high threshold of 250 keV and 2000 s acquisition time. The upper right corner is pronounced significantly due to presence of recoiled protons from the neutron interaction in the PE region above.

4. ATLAS-MPX project

This section describes the ATLAS-MPX project as an application of the pixel detector Medipix2 for real-time measurement of the spectral characteristics and composition of the radiation environment inside the ATLAS detector during operation particularly in the early LHC operation stages with low luminosity.

4.1 The LHC accelerator and the ATLAS detector at CERN

Particle accelerators are tools used in the field of high energy physics to study the internal structure of the matter helping us to understand the physicals processes in the nature. One of the world's biggest experimental programs in high energy physics is running at CERN (European Organization for Nuclear Research [24]) situated near Geneva on the border between Switzerland and France.

Figure 26. An aerial view of the CERN experimental site near Geneva. LHC and SPS accelerator rings are sketched in [24].

4.1.1 The Large Hadron Collider

The Large Hadron Collider (LHC) is the world's largest and most powerful particle accelerator. The LHC is situated in a tunnel 27 km in circumference approximately 100 m below the ground beneath the France - Swiss border near Geneva (see aerial view in Fig. 26). It is a synchrotron accelerator designed to collide opposing particle beams of either protons or lead ions. Its operation started 10th September 2008 but shortly after an accident occurs causing more than one year of delay. Now the LHC run at energy of 3.5 TeV per beam.

There are four different large detectors built at the four interaction points of the LHC:

- **ATLAS** - *A Toroidal LHC ApparatuS* - A general-purpose detector designed to investigate the widest range of fundamental physics, such as the Higgs boson, extra dimensions and particles that could be responsible for dark matter and super symmetry.
- **CMS** - *Compact Muon Solenoid* - A general-purpose detector with the same goals as the ATLAS detector. Having these two detectors reduces the possibility of biased results and makes discoveries more convincing.
- **ALICE** - *A Large Ion Collider Experiment* - A detector built to focus on heavy ion (lead) collisions to investigate the nature of the quark-gluon plasma.
- **LHCb** - *Large Hadron Collider beauty* - This experiment will investigate why the antimatter-matter quantity is so different as we observe in the universe today by high-statistics studies of hadrons containing a b-quark.
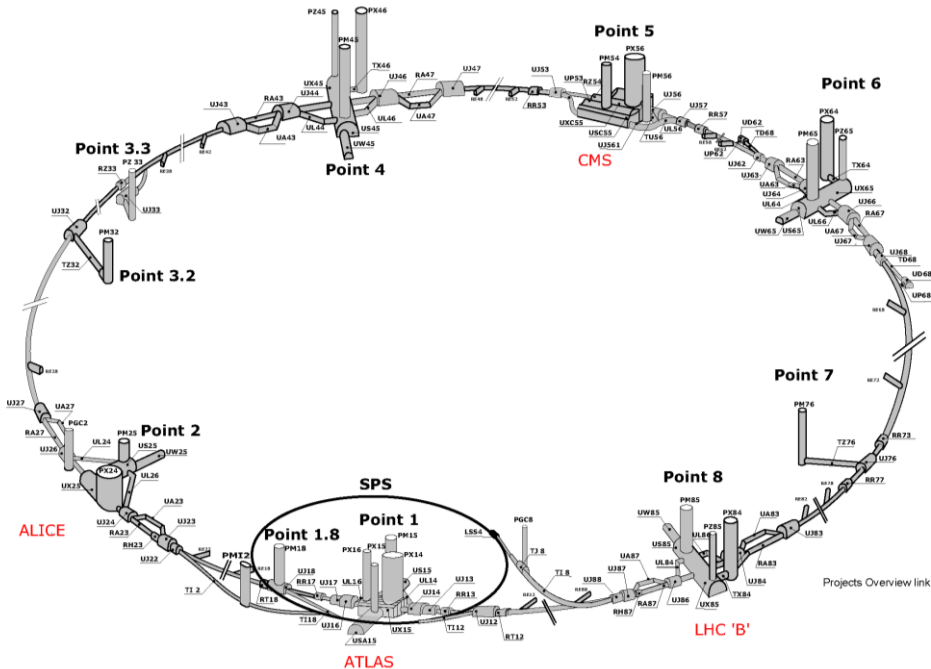
Figure 27. Layout of the LHC tunnel with position of the four big detectors and support infrastructure. There are three additional smaller experiments at LHC (TOTEM, LHCf and MoEDAL) [24].

4.1.2 ATLAS detector

ATLAS is one of two general-purpose detectors at the LHC [25] designed to exploit the full potential of the LHC p-p collision program. ATLAS detector will record sets of measurements on the particles created in collisions - their paths, energies, and their identities. This is accomplished in ATLAS through six different detecting subsystems that identify particles and measure their momentum and energy (see Fig. 28):

- **Inner detector (ID)** is used for tracking and measurement of the charge and the transverse momentum of charged particles. It is composed of pixel detector, semiconductor tracker (SCT) and transition radiation tracker (TRT).
- **Calorimeters** are used for identification of electrons, photons and hadrons and measurement of their energies. It consists of liquid argon electromagnetic calorimeter (LAr) and hadronic tile calorimeter (TileCal).
- **Muon spectrometer (MS)** serves for identification, tracking and measurement of charge and momentum of muons.
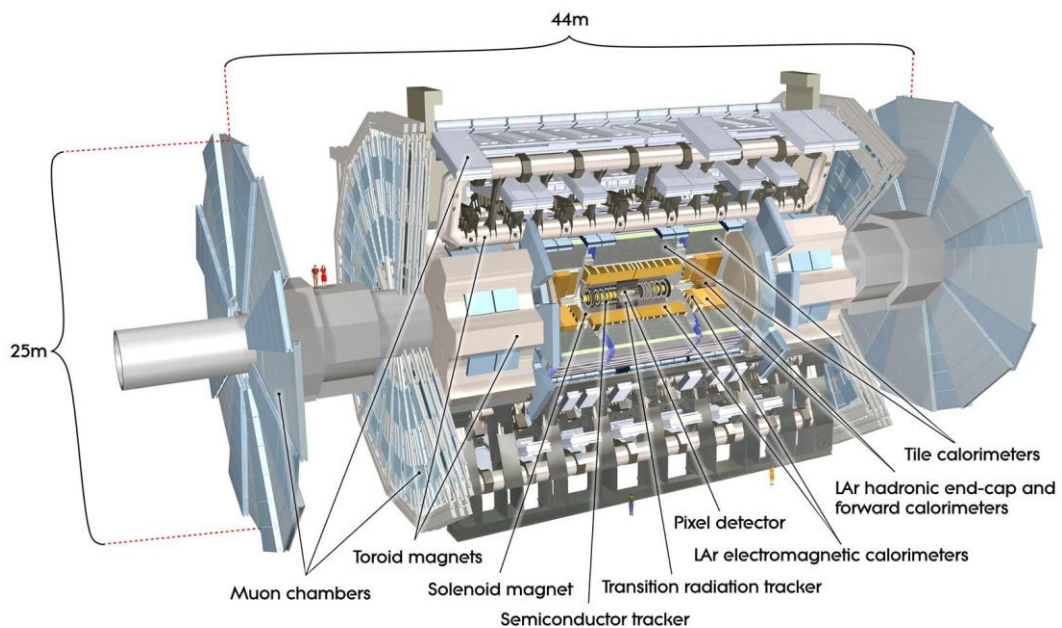
Figure 28. A computer model of the ATLAS detector showing position of the main components and detector systems. The ATLAS detector is the largest volume particle detector ever constructed with the size of 44 m × 25 m × 25 m and weight of 7000 tones [24].

There can be as much as 6×10^9 particle collisions in the ATLAS interaction point and the data recorded by ATLAS detectors for each collision takes about 1 MB. Such enormous dataflow cannot be handled by any data acquisition system. For this reason ATLAS is equipped with a very advanced 3-level trigger and data acquisition system designed to reject uninteresting events and keep the data flow in the feasible range of ~100 MB.s^{-1}.

4.2 ATLAS-MPX detector network project

The precise evaluation of spectral characteristics and composition of radiation in and around the ATLAS detector is necessary for understanding the performance of various detector systems and to predict their useful lifetimes. The results of these measurements may prove to be an important feedback for data analysis and improvement of data taking strategy, particularly in the early phase of operation. For this purpose a system of 16 ATLAS-MPX detecting devices has been installed in the ATLAS experimental cavern [26]. This system is capable of providing quantitative real-time information on fluxes and flux distributions of the main radiation species in the experiment including slow and fast neutrons. The original proposals for this system can be found in [2] and [3]. Three main tasks were identified from an operational point of view:

- Measurement of the radiation field inside the ATLAS detector volume including neutrons.
- Measurement of background radiation in the experimental hall and in the detector surroundings.
- Measurements in the neighborhood of selected subdetectors to determine characteristics such as particle/energy leakage, punch through, etc., which can contribute to the evaluation of their performances.

4.3 Description of the ATLAS-MPX detector unit

The ATLAS-MPX detector consists of a Medipix2 imaging assembly [1] with neutron converters mounted on the printed circuit board with passive components, connectors and drivers for three Ethernet cables (see Fig. 29 left). The sensitive part of the Medipix2 assembly comprises a 300 μm thick silicon chip.

a)   b)
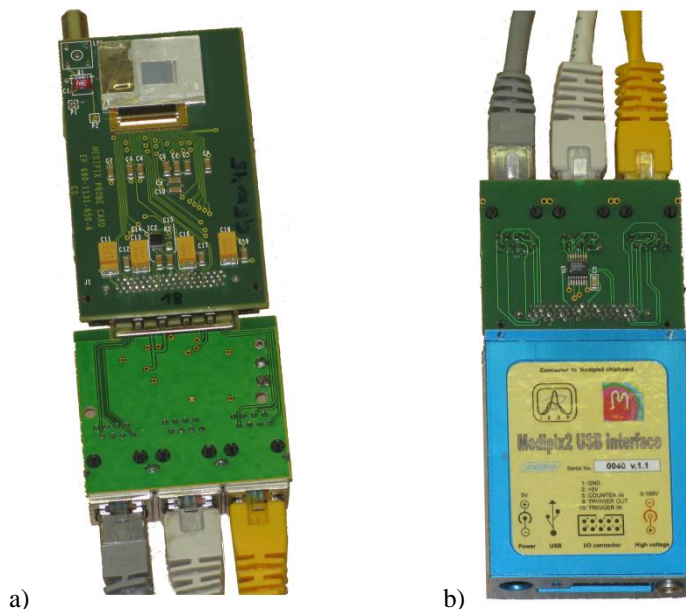
Figure 29. a) Open ATLAS-MPX detector unit. Medipix2 on a chipboard connected to the LVDS converter board. b) Universal Serial Bus (USB) based readout interface connected to the LVDS converter board counterpart.

When hitting the silicon sensor, the incoming particles deposit energy which creates free charge carriers. If the charge-generated signal exceeds the threshold, the pixel is activated and the counter is incremented by one. A single particle can activate one or several pixels forming a cluster of neighboring pixels. Cluster shape strongly depends on the physics of the interaction of the particle with the sensor material and process of charge collection. Different shapes are visible in the recorded frames (e.g., Fig. 21) similarly to what can be observed, for instance, in nuclear emulsion or bubble chamber.

All pixels are exposed simultaneously with a common, electronically adjustable shutter, that allows precise (few ns) exposure times from 10 μs to minutes or hours. This precise exposure control is the key to the large dynamic range. Particle hits outside the active exposure time are simply not recorded in the counters. The resulting 256×256 picture frame shows the illuminated pixels against the zero-count (not hit) pixels.

Each ATLAS-MPX detector is fitted in a blue duralumin box (see Fig. 30) with dimensions of 160 mm $\times$ 25 mm $\times$ 60 mm and an appropriate entrance window above the detector sensitive surface.
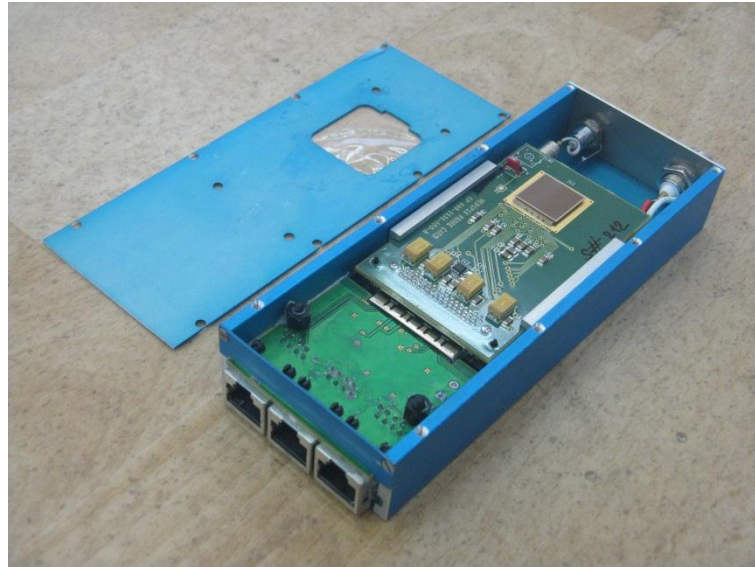
Figure 30. ATLAS-MPX detector (Medipix2 detector without the neutron conversion layers) mounted in the duralumin box.

4.3.1 Neutron conversion layers

For neutron detection, each detector is covered with a mask of converter materials dividing its area into regions sensitive to the different types of neutrons (thermal and fast). In the masked regions, the sensor is shielded against free alpha particles and other short-range heavily ionizing quanta. The structure of neutron converters is shown in Fig. 31a, where converting materials, ^{6}LiF and polyethylene (PE), are recognizable. These materials and their overlap with the aluminum support foils divide the sensitive area of each detector into following six different regions (see Fig. 31b):

1) **⁶LiF region** - The layer of 3 mg/cm³ thick ⁶LiF powder, spray coated below a 50 µm thick aluminum foil, is used for thermal neutrons detection, exploiting the large cross section of the ⁶Li(n,α)³H reaction.

2) **PE region** - Fast neutrons are detected via protons recoiled from their elastic interaction on a 1.3 mm thick PE foil above this region. Fast neutrons can be also directly registered via their nuclear reactions in silicon itself and in surrounding materials.

3) **PE+Al region** – In this area a 1.3 mm thick polyethylene foil lies on a 100 µm thick aluminum support, allows measurement of recoiling protons only with energies above 3.5 MeV. Here the aluminum foil acts as an energy threshold.

4) **Al foil** - The 100 µm thick Al foil serves as an attenuator of electrons and X-rays.

5) **Thick Al foil** - Thick Al foil, 50 µm + 100 µm thick aluminum, achieve further electron and X-ray attenuation.

6) **Uncovered area** - Remaining uncovered area is directly exposed to all incoming radiation. In this region, the fast neutrons can only be detected via nuclear reactions in silicon Si(n,p)Al and Si(n,α)Mg.
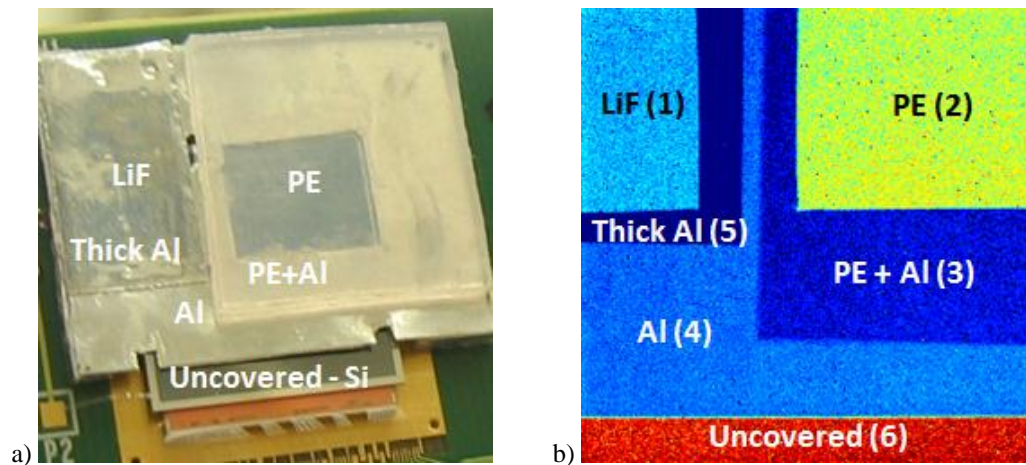
Figure 31. a) View on the MPX sensor covered with conversion layers. b) X-ray radiogram of the MPX detector conversion layers. Labels are explained in the text.

Detection efficiencies of the different regions in selected neutron fields were evaluated for each ATLAS-MPX detector unit. The calibration procedure is described in detail in section 5.

4.3.2 Connection structure of the ATLAS-MPX network

The detector data acquisition is controlled by the Universal Serial Bus (USB) based readout interface described in the section 3.2.1. Because the ATLAS-MPX detectors are mostly operated at positions with high radiation level in UX 15 experimental cavern, the USB interfaces are located in USA15 service cavern (see Fig. 33) and the connection with

the ATLAS-MPX detector is achieved through LVDS[12] converter board (Fig. 29). This board translates some CMOS logic signals of the Medipix2 chip to the LVDS standard which is more suitable for communication over long distances. Three Ethernet cables are used transfer all necessary Medipix2 signals (4 twisted pairs each). Moreover separate power cable is used to bring low voltage power to the chip (5 V) and to bias the silicon sensor (100 V).

All these cables go to the USA15 infrastructure area where computers and readout interfaces are situated (see Fig. 32). There are three control computers in USA15 each controlling the data acquisition of 5 ATLAS-MPX devices located in UX15. These three computers communicate with the main computer which serves as a main data storage and communication gate.

There is not direct access to the devices during the LHC operation. Especially during long term operation there is not negligible risk of detector malfunction due to radiation damage or SEE[13]. In this case, special circuit designed to control power supply for up to six USB interfaces via USB protocol can switch off the detector and readout power supply. It is possible to reset all ATLAS-MPX detectors remotely by means of this circuit to its initial state.
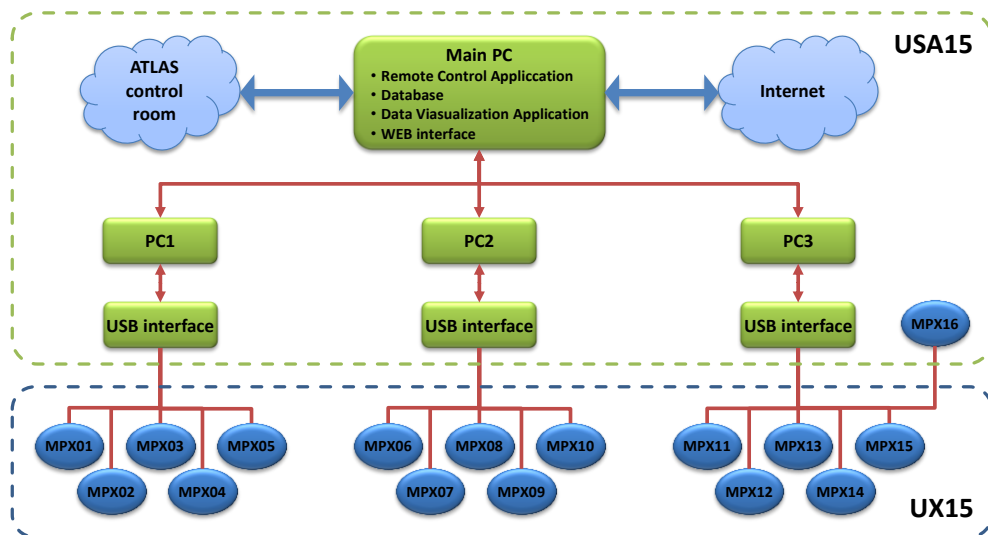
Figure 32. Diagram of the connection of the ATLAS-MPX network devices from their position in the UX15 experimental hall to USA15 infrastructure area where the computers are situated.

The length of the cables from USA15 cavern to the ATLAS-MPX devices is roughly 100 m, so it was necessary to significantly reduce the readout clock frequency of the USB interface. After each exposure, the counters of all pixels are read out in ~6 s, what means that the maximum frame rate of 0.15 frames per second.

---

[12] Low Voltage Differential Signaling
[13] Single Event Effect

37

4.4 ATLAS-MPX network layout

The ATLAS-MPX detectors are installed in UX15 experimental cavern (15 devices) and USA15 cavern (one device) (see Fig. 33). The nominal interaction point is defined as the origin of the coordinate system. The beam direction defines the Z-axis and the X-Y plane is transverse to the beam direction. The positive X-axis is defined as pointing from the interaction point to the center of the LHC ring and the positive Y-axis is defined as pointing upwards. The side A of the detector is defined as that one with positive Z and side C is that one with negative Z.
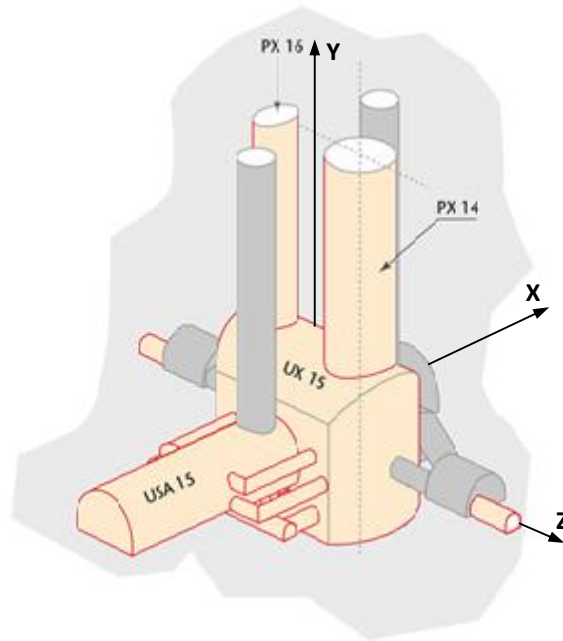
Figure 33. Image of the ATLAS detector caverns showing the position of the UX15 experimental cavern and USA15 infrastructure area [24]. Side A of the detector is at the right hand side of the image. Negative X-axis is in the direction of USA15.

The positions of the ATLAS-MPX devices are depicted on Fig. 34 and Fig. 35. Exact coordinates of all devices are summarized in Tab. 2.

- Two devices are between ID and JM plug in front of LAr calorimeter (one on side A and one on side C).
- Three devices are between TileCal barrel and TileCal extended barrel (EB) (two on side A and one on side C).
- One device is on the top of TileCal barrel and one is on the top of TileCal EB, both on side A.
- Three devices are on the muon small wheel chambers (side A) and one is attached to EIL4 part of the muon spectrometer (side A).
- One device is placed within JF shielding at the back of LUCID detector close to the LHC vacuum chamber.
- Four devices are placed outside of the experiment volume dedicated to the measurement of radiation background during LHC operation (one device sits on

top of JF cylindrical shielding, two on cavern walls and the last one is placed inside USA15 cavern).
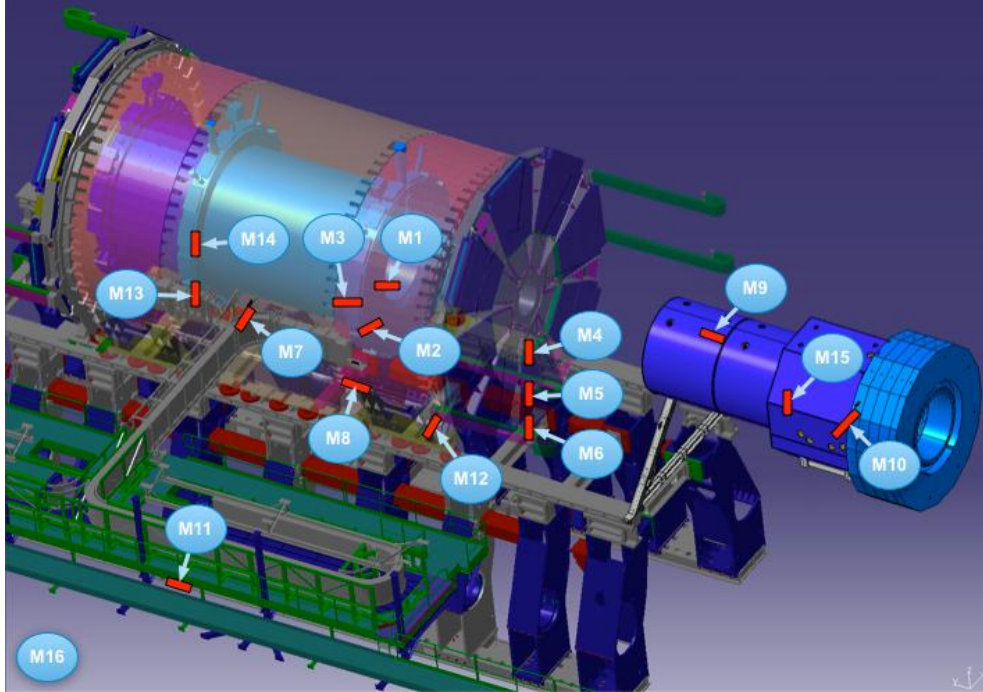
Figure 34. The network of ATLAS-MPX detectors in ATLAS.

Name	Location description	X [m]	Y [m]	Z [m]	R [m]
MPX01	between ID and JM plug	-0.71	0.29	3.42	0.77
MPX02	between TILE and EB	-2.23	-1.12	3.42	2.50
MPX03	between TILE and EB	-3.45	0.93	2.94	3.57
MPX04	on the Small Wheel	-0.65	-1.30	7.12	1.30
MPX05	on the Small Wheel	-0.55	-2.36	7.20	2.36
MPX06	on the Small Wheel	-0.65	-3.36	7.20	3.36
MPX07	top of TILECAL barrel	-4.53	0.79	0.35	4.59
MPX08	top of TILECAL EB	-4.37	-0.53	4.02	4.40
MPX09	on the JF cylinder	0.00	1.56	15.39	1.56
MPX10	cavern wall HO	-3.96	3.36	22.88	5.19
MPX11	cavern wall USA side	-16.69	0.05	4.86	16.69
MPX12	on the EIL 4	-6.25	0.00	7.23	6.25
MPX13	between TILE and EB, C	-2.21	-1.02	-3.42	2.44
MPX14	between ID and JM plug, C	-0.71	-0.30	-3.43	0.77
MPX15	at the back of LUCID	0.19	-0.08	18.74	0.20
MPX16	USA15	-39.48	0.90	-6.55	39.48

Table 2. ATLAS-MPX detector location and positions with respect to the central interaction point. Axes X, Y and Z correspond to the standard ATLAS coordinate system, $R = (X^2 + Y^2)^{1/2}$ is the distance from the beam axis at position Z).
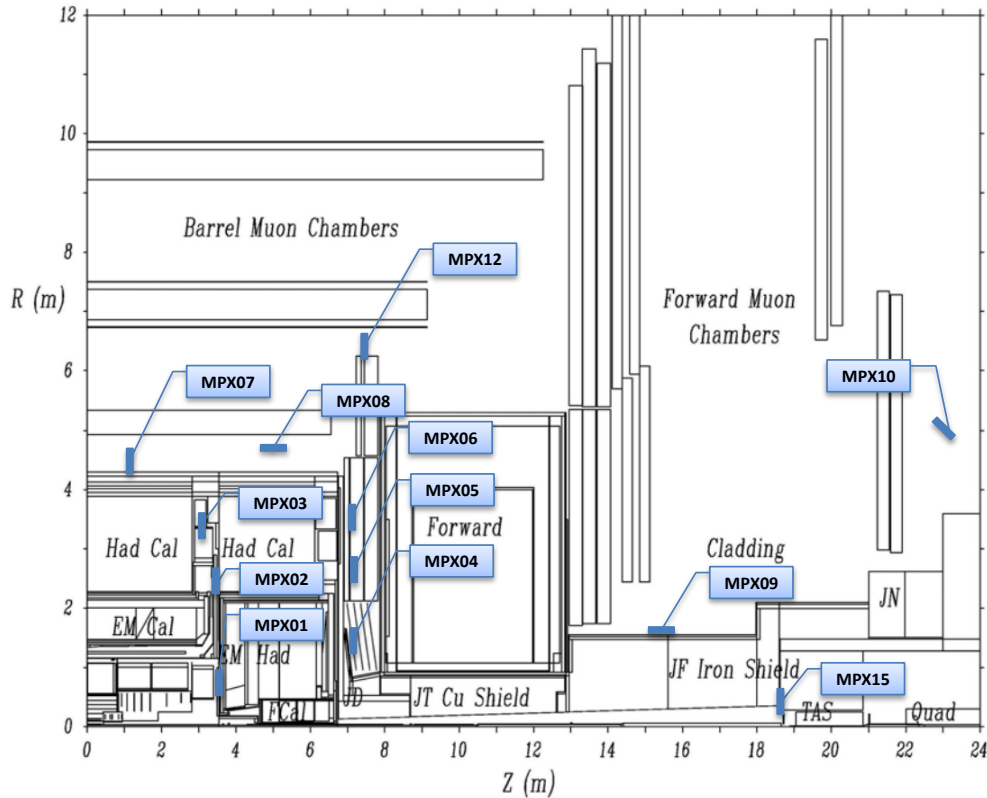
Figure 35. Locations and orientations with labels for 12 of 16 ATLAS-MPX detectors on side A in ATLAS. MPX13 and MPX14 are placed on side C almost symmetrically to MPX01 and MPX02. MPX11 is out of R-axis range and MPX16 is located in USA15. The detectors are oriented in three different directions: Perpendicular to the beam axis (Z-axis) facing the IP: MPX01, MPX02, MPX03, MPX04, MPX05, MPX06, MPX07, MPX12, MPX13, MPX14, MPX15; parallel to the beam axis: MPX08, MPX09, MPX11, MPX16; at 45º to the beam axis: MPX10.

At these positions the devices provide the real-time measurement of count rates of different particles species. These measurements give the capability to fulfill radiation monitoring tasks inside the ATLAS detector volume and cavern. One of these tasks is the measurement of radiation background (neutrons, X-rays, gamma rays, ions…) at the positions of the ATLAS-MPX detectors, in the environment of the ATLAS sub-detectors (forward regions of LAr calorimeter, TileCal, Muon chambers) and cavern. The measurement of neutron fields can be used for the evaluation of the radiation hardness of electronics and detectors operated at positions exposed to high radiation level. In particular, the measurement of neutron fluxes with the ATLAS-MPX detectors permits the determination of the neutron contribution to the radiation field close to the JM shielding between the ID and LAr. The comparison of measured neutron fluxes with Monte Carlo simulations results allows the assessment of the effectiveness of the ATLAS neutron shielding (JM and JF shielding).

On-line measurements of the radiation field will also contribute to the estimates of Single Event Upset (SEU) effects possibly affecting the electronic devices and control functions operating in the ATLAS experiment environment.
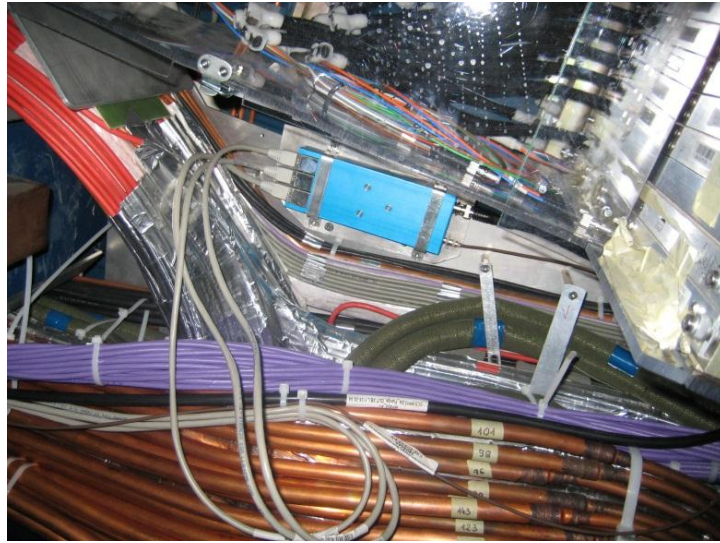
Figure 36. Placement of an ATLAS-MPX detector mounted in the blue duralumin box (MPX03) in real ATLAS environment on side A close to the LAr readout electronic.
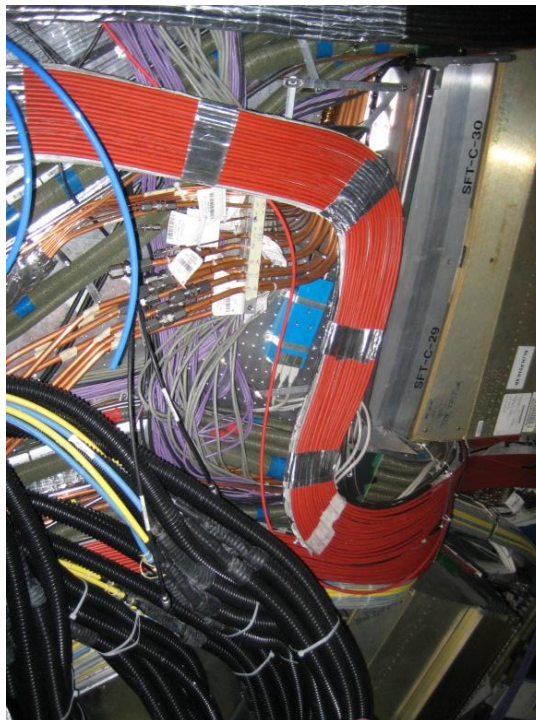
Figure 37. Location of an ATLAS-MPX detector mounted in the blue duralumin box (MPX13) in real ATLAS environment on side C between TileCal barrel and extended barrel.

The location of ATLAS-MPX detectors close to calorimeters also serves during data taking to provide information on the composition of cascades and related fluxes of particles possibly leaking out of calorimeters. Such calorimetric information is relevant for transverse energy measurements.

41
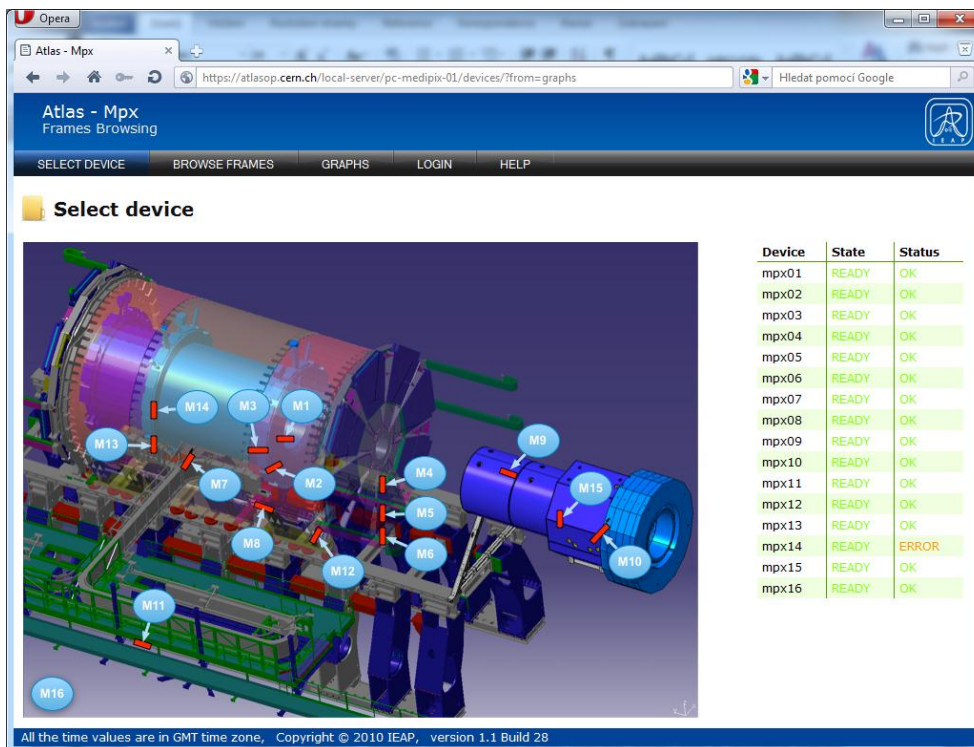
The correlation observed between the recorded numbers of events of each species measured in each ATLAS-MPX device and the LHC machine luminosity allows the ATLAS-MPX detectors to be used as a system of luminosity monitors. This is particularly true for the three ATLAS-MPX detectors (MPX01, MPX14 and MPX15) positioned close to the beam axis, which are the most sensitive. The variation in count rates measured in these detectors reflects the van der Meer luminosity scans performed in IP1.

4.5 User access to ATLAS-MPX data

ATLAS user may have access to the data currently or previously recorded by the ATLAS-MPX detectors. The user accessing the ATLAS-MPX web page [26] (under Detector Operation / Infrastructure / Radiation Monitors / ATLAS-MPX) may select a particular ATLAS-MPX detector, use a browser frame to visualize frames of this given (or any other) detector and finally may use graphs to visualize different cluster types or hits in pixels over a given period of time in a form of a plot.

4.5.1 Select Device

Select Device page shows the positions of all the detectors within UX15 cavern. User can click on each detector to select it for access to frames or graphs visualization. By hovering with cursor over the detector, its coordinates (X, Y, Z, and R) are shown. The current operation status of all detectors is shown in the table on the right side of the screen (see Fig. 38).

Figure 38. Screenshot from the Select Device page.

4.5.2 Browse Frames

Browse Frames page (see Fig. 39) is used to visualize single frames. In the detector box, user can change the detector to show frames either by selecting from the list box menu or by clicking on the *Select* link which will take him to *Select Device* page.
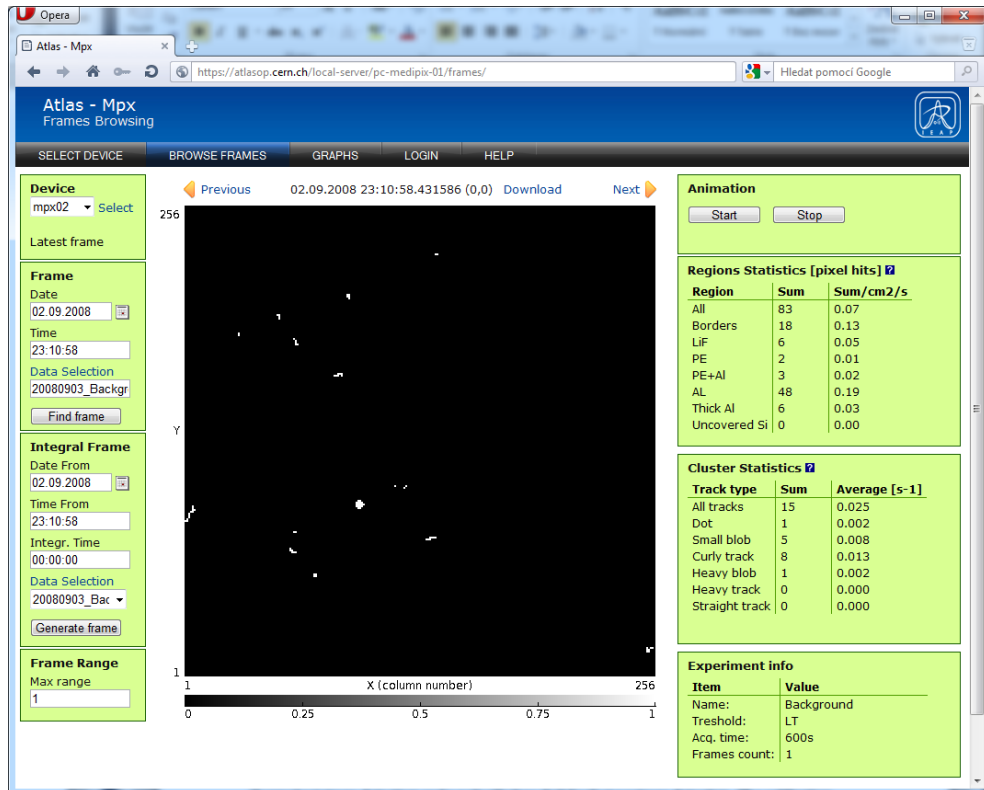
Figure 39. Screenshot from the Browse Frames screen.

In the *Frame* box it is possible to find a particular frame by its date and time or by experiment through clicking on *Data Selection* link and choosing the experiment of interest.

In the *Integral Frame* one can generate integral frames (sum of several consecutive frames). The first frame is specified by date and time (*Date From* and *Time From*) and then the time range needs to be specified in which frames will be summed (*Integr. Time*). Frames can be integrated only within a single experiment. Experiment can be chosen from the *Data Selection* list box menu.

In the *Frame Range*, box use can specify maximal range of Z axis (counts) in the frame. Browsing through the frames can be achieved by clicking on the *Next* and *Previous* link on top of the frame showing the next and previous frame, respectively. It is also possible to create an animation of frames by clicking on *Start* button in *Animation* box. Every second a next frame will be automatically visualized.

Region Statistics shows the sum of number of hits in pixels in each region. *Cluster Statistics* shows the sum of different cluster types in the current frame (or integral frame). In a case of integral frame, average number per frame is also calculated. In the

Experiment Info box one can see the basic settings of the device used for the particular experiment.

4.5.3 Graphs

This page has the purpose of visualizing different cluster types or hits in pixels over longer period of time in a form of plot (see screenshot in the Fig. 40). The detector whose plot is to be seen can be selected in *Device* list box menu in the same manner as in *Browse Frames* page. There is also the possibility to show quickly plots for last hour, last 24 hours, last week and last month by clicking on the links in *Device* box, respectively. Cluster types that should be visualized in the plot can be selected in *Cluster type* box. Regions that will be included in the plot can be selected in *Regions* box. Time range is specified in the *Time range* box by selecting starting date and time (*From Date* and *From Time*) and end time (*To Date* and *To Time*). In the case there is more experiment in the selected time range user can choose the desired experiment in the *Data Selection* list box menu. When the time range of a whole experiment is needed, the experiment can be selected by clicking on *Data Selection* link and time range is automatically filled with the time range of the experiment. Different graphs settings are available in *Graph parameters*:

- *Cluster/Region characteristics* - This switches plotting of the different cluster types in the selected *Regions* (cluster statistic) or number of occurrence of one selected cluster type in specified regions (region statistic).
- *Limit range of "Number of events" in graph* - Limits maximal range of Y axis.
- *Plot counts* - Instead of clusters, pixel hits in the frame are shown.
- *Integral graph* - Integral graph of clusters/pixel hits is plotted in the specified time range.

The *Statistics* box shows sum of different cluster types for the specified time range and average number normalized per second.

The easiest way to generate a plot in a graph tab is to select the device of interest from the "Device" frame and click on "last hour", "last day" etc. This will generate the default plot. If the parameters of the measurement have been modified (different sets of measured data called "experiments") during the selected time scale, the first one will be displayed and the next one can be displayed by choosing it from the "Data selection" combo box in the "Time range frame and click on "Plot graph" button.

The assignment of morphological categories (blob, track, etc.) to real particles is displayed as an help text when the cursor is moved over the corresponding check box in the "Cluster type" frame (that is generally the kind of help used over the whole web page but more detailed text to the help tab as well is in preparation). This description is valid only for the low threshold measurements (marked as LT on the graph label).

The time as given on MPX network web page is the GMT time. However, the time used in text describing results obtained with the MPX network can be CET time, including seasonal time shifts (winter, summer time). Hence, the user should accordingly take into account one or two hour shift in time between MPX network time and current CET time.
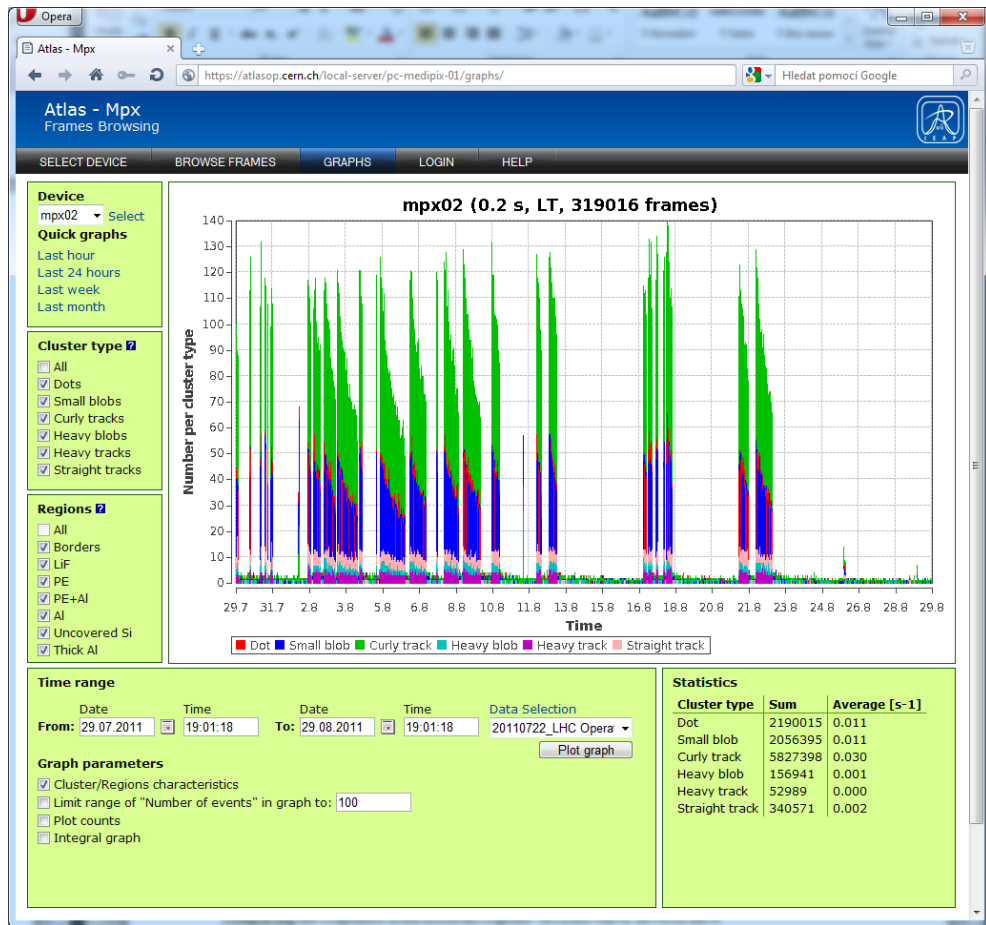
Figure 40. Screenshot from the Graphs screen.

5. ATLAS-MPX detector calibration

One of the main goals of the ATLAS-MPX network is to measure overall radiation field composition within ATLAS detector including neutron fields. Different radiation species are detected via different interaction mechanisms and therefore an extensive calibration of all devices installed in ATLAS was performed together with the two devices of reference. Reference devices allow us to do further measurements and apply the results on the devices already installed in ATLAS UX15 cavern.

5.1 Energy calibration

Energy calibrations of all devices were performed using the technique described in [28] to translate the ADC threshold units of the ATLAS-MPX devices to its corresponding energy. The detectors were placed in a light shielded box at room temperature and uniformly exposed to the radioactive source. Two sources were used:

- ^{55}Fe source of X-rays with energy of 5.8 keV
- ^{241}Am source of gamma photons with energy of 59.5 keV and 13.9 keV

After the pixel threshold equalization the devices were set to the single threshold counting mode and the threshold scan was performed, while irradiating with above mentioned radiation sources, for threshold (THL) values where the corresponding energy peak position was anticipated. Example differential plots of this scans for ^{55}Fe and ^{241}Am sources are shown in Fig. 41.

From the Gaussian fits of the peaks in THL scans the energy calibration curve was calculated. The 5.8 keV peak from ^{55}Fe is very close to the noise level of the device and couldn't be measured for some detectors. In this cases the 13.9 keV peak from ^{241}Am was used. A typical calibration plot is shown in Fig. 42. The detector has a linear dependence on the energy in the energy region from $6 - 60$ keV (can be extrapolated further).
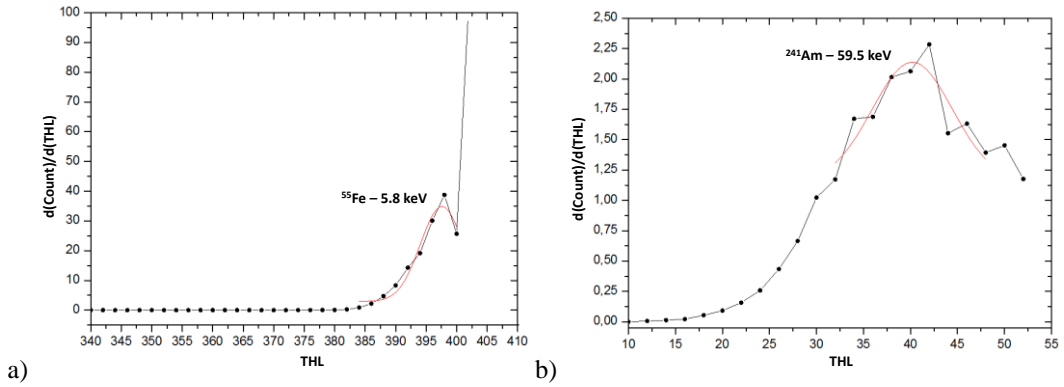
Figure 41. Example of the low energy threshold scans for one of the ATLAS-MPX detectors. a) 5.8 keV energy peak from [55]Fe source (close to the detector noise floor). b) 59.5 keV energy peak from [241]Am source.

Data were measured individually for all ATLAS-MPX detectors. The calibration curves remain consistent within 10% for all ATLAS-MPX devices. Note that this calibration was made globally for the whole device and therefore is limited in precision. For more precise result it would be necessary to perform per pixel energy calibration similarly to [29].
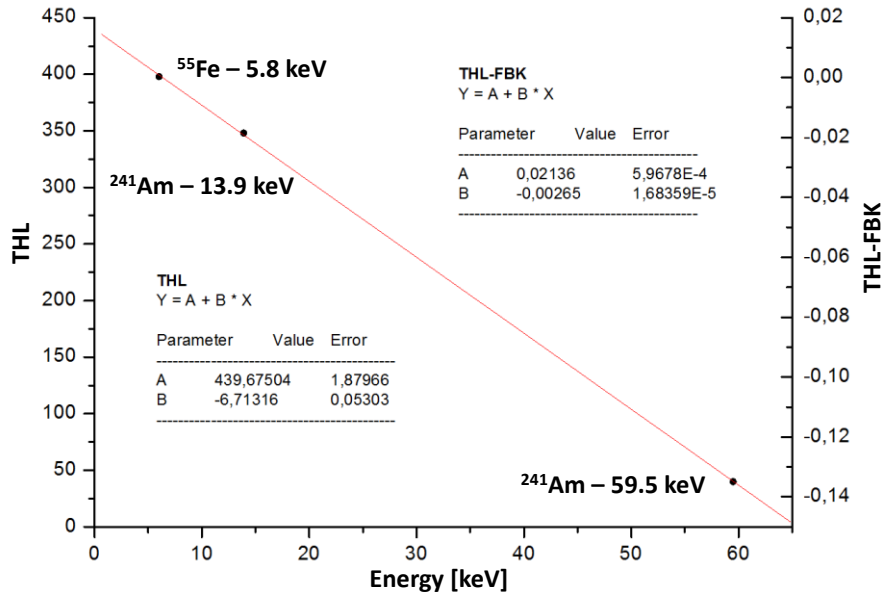
Figure 42. Example of the energy calibration curve for one of the ATLAS-MPX detectors. The calibration curves remain consistent within 10% for all ATLAS-MPX devices.

5.2 Photon efficiency calibration

Photons are electrically neutral particles and therefore cannot be detected directly by means of Coulomb force. They have to interact first in the silicon sensitive volume by one of the mechanisms described in subsection 2.1.3. The probability of the photon interaction in the sensitive volume of the ATLAS-MPX detector decrease significantly

with increasing photon energy. The detection efficiency of the Medipix2 detector bump bonded to the 300 μm silicon sensor chip is depicted in Fig. 43 from [28].

For the ATLAS-MPX devices the photon detection efficiency will vary from region to region due to photon attenuation in the material used for neutron conversion as shown in Fig. 31. This effect will be directionally sensitive and pronounced more significantly for lower photon energies.
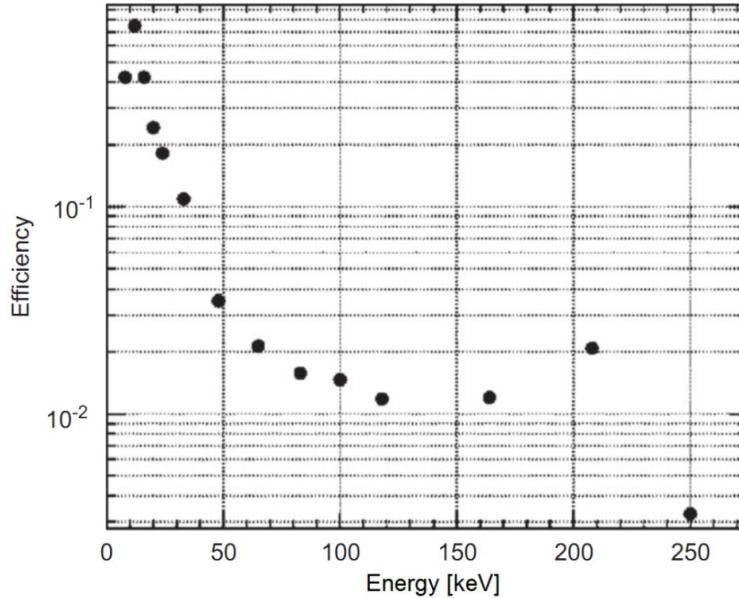
Figure 43. Photon detection efficiency of the Medipix2 detector with 300 μm silicon sensor [28]. For the ATLAS-MPX devices the photon detection efficiency will vary from region to region due to photon attenuation in the material mask used for neutron detection (see Fig. 31). This effect will be directionally and energy sensitive.

The response of the ATLAS-MPX device operating in the tracking mode to the X-ray photon irradiation will be clusters of several adjoining pixels. The size of these clusters will increase with increasing photon energy as shown in Fig. 44 from [28]. For energies around 10 keV there will be almost only single pixel clusters falling into dot category as described in subsection 3.4.1. For X-ray energies of several tens of keV the clusters will fall into small blob category. For energetic gamma photons the secondary electron will generate curly track signature.

In mixed radiation field it is not simple to distinguish between primary electron interactions and photon generated secondary electrons. In both cases the cluster signatures, commonly referred as low energy transfer signatures, will be the same for the same electron energies. The calculation of photon flux is not possible without further knowledge about the field composition and anisotropy.
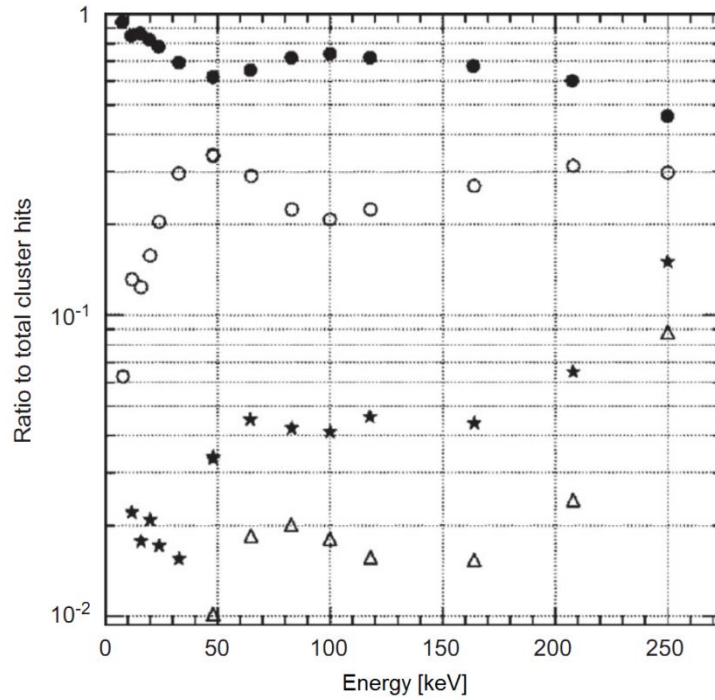
Figure 44. Electron track lengths as a function of energy: single-pixel clusters (●), two-pixel clusters (○), three-pixel clusters (*) and four-pixel clusters (Δ).

5.3 Fast and thermal neutron efficiency calibration

Detection efficiency for neutrons depends significantly on the geometry of neutron convertors positioning above the sensitive silicon area. Therefore, the efficiency calibration was performed individually for all devices with set of known neutron sources:

- **Thermal neutrons** - Neutrons from ^{238}PuBe sources moderated in graphite prism to form the isotropic field with cadmium ratio[14] of ~20 with flux of 2.5×10^6 neutrons.cm^{-2}.s^{-1}
- **^{252}Cf** – Fast neutrons with average energy of 2.1 MeV (see spontaneous fission spectrum in Fig. 45) and emission of 1×10^8 neutrons.s^{-1}.
- **^{241}AmBe** - Fast neutrons with average energy of 4.5 MeV (see spectrum in Fig. 45) and emission of 4×10^7 neutrons.s^{-1}.
- **14 MeV neutrons** – Generated from T(d,n)α reaction on Van de Graaff accelerator (VDG)

---

[14] Cadmium ratio is the ratio of response of an uncovered neutron detector to that of the same detector under identical conditions when it is covered with cadmium of a specified thickness. The neutron energy of 0.5 eV is taken as the boundary between those low energy neutrons that are absorbed by cadmium sheet and those higher energy neutrons that are not so absorbed. The cross section of ^{113}Cd is very large below this energy level as shown in Fig. 9.
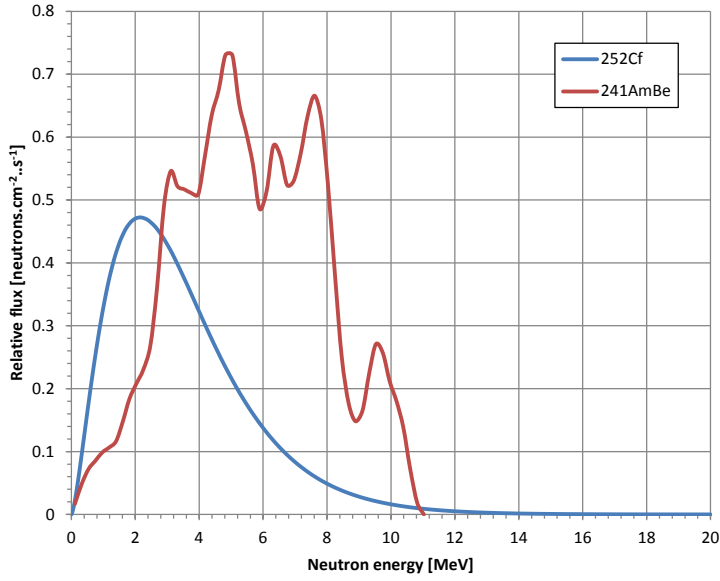
Figure 45. ^{252}Cf and ^{241}AmBe neutron spectra.

The high threshold (~250 keV) mode of operation was used in order to exclude all tracks induced by light particles in silicon. The acquisition time was set short enough in order to get about 100 registered events per frame. These separated tracks have been identified and counted. The efficiencies have been calculated according to the following equation:

$$\varepsilon_{A-Si} = \frac{\dfrac{N_A}{S_A} - \dfrac{N_{Si}}{S_{Si}}}{\Phi t} \tag{7}$$

where N_A, N_{Si} are detected number of events during the whole measurement in region A (^{6}LiF region was used for slow neutrons, PE region was used for fast neutrons) and for uncovered (Si) region (see Fig. 31); S_A, S_{Si} are areas corresponding to these regions; Φ is the incident neutron flux and t is the time of measurement. Graphs in Figures 46 – 49 shows the results of neutron efficiency calibration for all ATLAS-MPX devices including reference devices compared to the simulation [30], [31]. Mean values of the measured efficiencies are summarized in Tab. 3.

Source	Mean efficiency	Tolerance*
Thermal neutrons	1.02E-2	26%
^{252}Cf source (mean energy 2.1 MeV)	3.17E-4	21%
^{241}AmBe source (mean energy 4.5 MeV)	7.51E-4	16%
14 MeV neutrons from VDG	1.81E-3	14%

*This means standard tolerance of all calibrated devices.

Table 3. Summary of the mean neutron detection efficiency of the ATLAS-MPX devices.
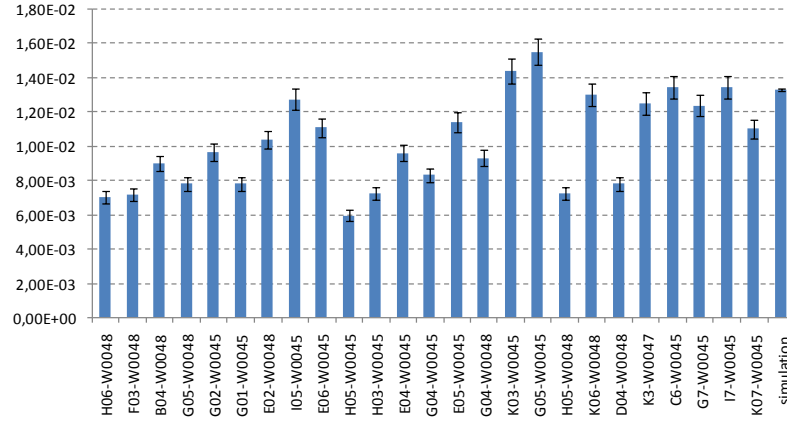
Figure 46. Thermal neutron efficiencies (^{6}LiF-Si region); mean value 1.02E-2; standard tolerance of all calibrated devices 26%.
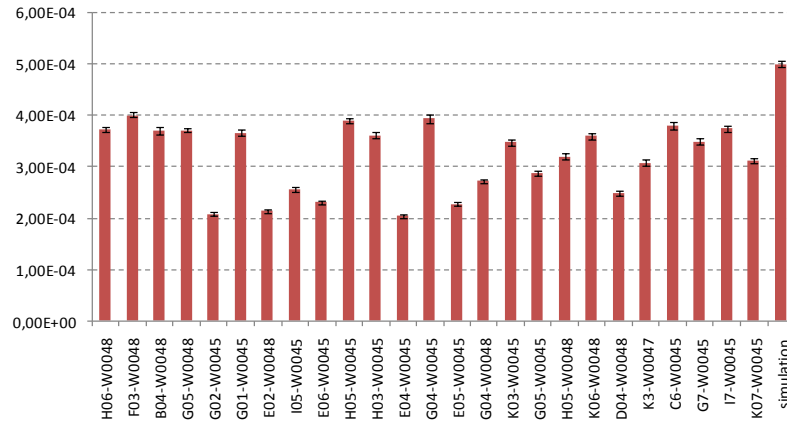
Figure 47. ^{252}Cf neutron (mean energy 2.1 MeV) efficiencies (PE-Si region); mean value 3.17E-4; standard tolerance of all calibrated devices 21%.
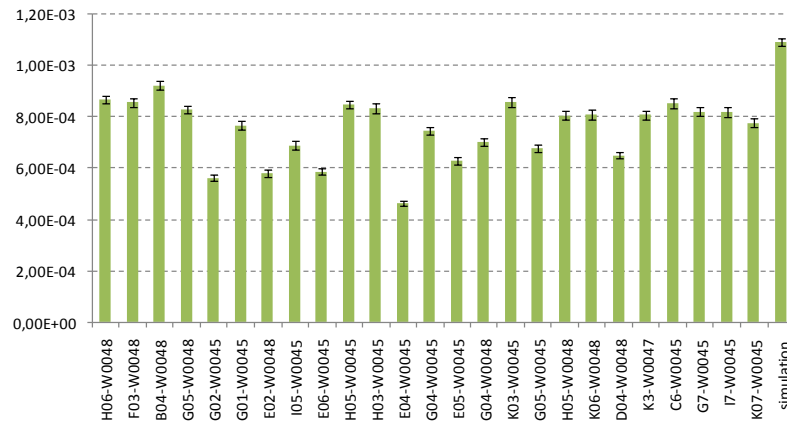
Figure 48. ^{241}AmBe neutron (mean energy 4.5 MeV) efficiencies (PE-Si region); mean value 7.51E-4; standard tolerance of all calibrated devices 16%.

51
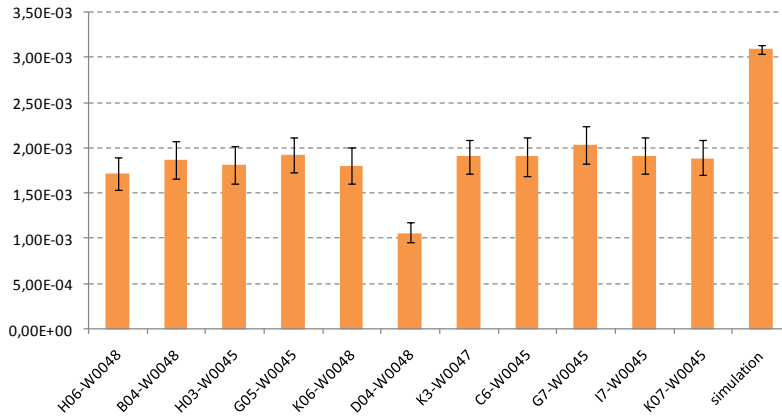
Figure 49. 14 MeV neutron efficiencies from Van de Graaff accelerator (PE-Si region); mean value 1.81E-3; standard tolerance of all calibrated devices 14%.

The event ratio between PE and PE+Al regions brings information about the energy hardness of the incident neutron spectrum. Protons recoiled from the fast neutron interaction in the PE layer above the sensor area are attenuated in the aluminum layer present in PE+Al region as depicted in Fig. 50. Protons in the low energy range can be stopped completely or reach the silicon layer with energy too low to exceed high energy threshold level of ~250 keV. Measured attenuation is in a good agreement with the result of the simulation (see Fig. 51).
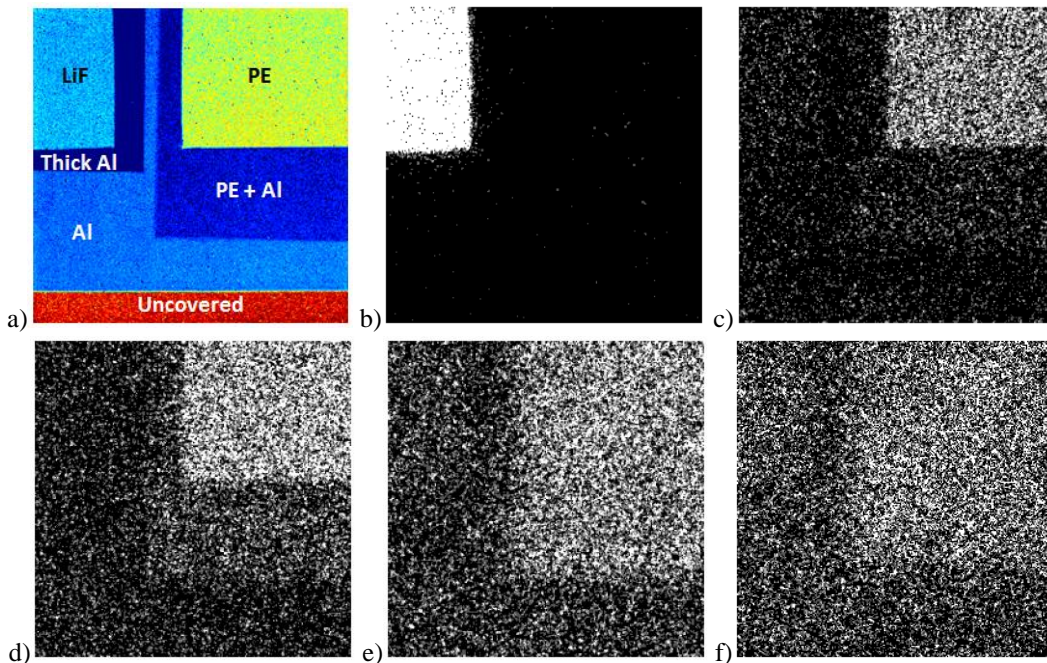
Figure 50. a) X-ray radiogram of conversion layers above one of the ATLAS-MPX devices. Integrated response of the device set to high threshold mode to b) thermal neutrons (25 meV) and to fast neutrons of c) ^{252}Cf (2.1 MeV); d) ^{241}AmBe (4.5 MeV); e) Van de Graaff accelerator (14 MeV) and f) cyclotron (2 - 30 MeV).
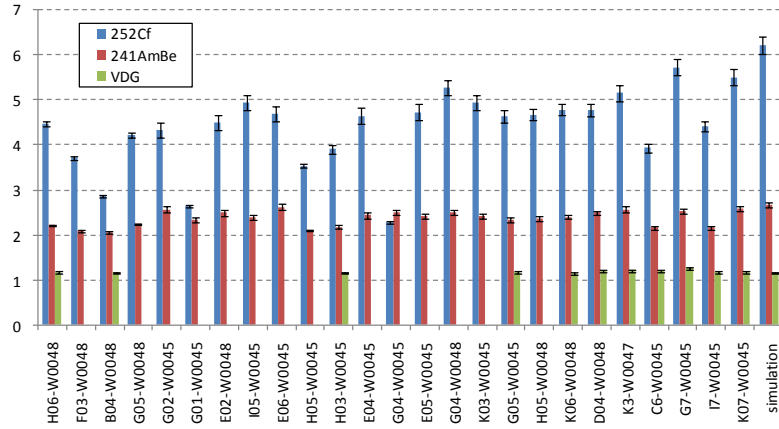
Figure 51. Event ratio between PE and PE+Al region (see Fig. 31). Mean value for [252]Cf is 4.37; tolerance 19%, for [241]AmBe it is 2.37; tolerance 7% and for 14 MeV neutrons the mean value is 1.19; tolerance 3% (note that not all the devices were calibrated with 14 MeV neutrons).

5.4 Dose rate calibration with ^{137}Cs and ^{60}Co gamma sources

Absorbed dose is a measure of the energy deposited in a medium by ionizing radiation per unit mass. It is commonly used in correlation with the level of damage of a material or equipment by influence of the radiation field. For the purposes of the radiation damage to equipment (especially electronic circuits) a quantity called Kerma[15] in air is used.

For the description of the radiation field for radiation protection purpose a quantity called photon ambient dose equivalent H*(10) is used. This measurable quantity is used in radiation protection surrogates describing the biological effectiveness of the absorbed dose in different human tissues.

For the purposes of the dose calibration the ATLAS-MPX detector of reference was exposed to [137]Cs (662 keV) and [60]Co (1173 keV and 1333 keV) photon sources of known ambient dose equivalent rate in separate measurements (see the response in Fig. 52). The measurements were performed for several ambient dose equivalent rates and under different angles. Average value of the calibration coefficients are presented below:

[137]Cs photon source
- Cluster composition: 38% curly tracks, 36% small blobs, 25% dots
- H*(10) rate: $(1.71 \pm 0.07) \times 10^{-10}$ Sv.event[-1]
- Kerma in air rate: $(1.42 \pm 0.06) \times 10^{-10}$ Gy.event[-1]

[60]Co photon source
- Cluster composition: 54% curly tracks, 28% small blobs, 17% dots
- H*(10) rate: $(2.26 \pm 0.19) \times 10^{-10}$ Sv.event[-1]
- Kerma in air rate: $(1.95 \pm 0.16) \times 10^{-10}$ Gy.event[-1]

---

[15] Kinetic Energy Released per unit Mass is the sum of the initial kinetic energies of all charged particles produced by uncharged ionizing radiation (i.e. photons and neutrons) in a sample of matter, divided by the mass of the sample.
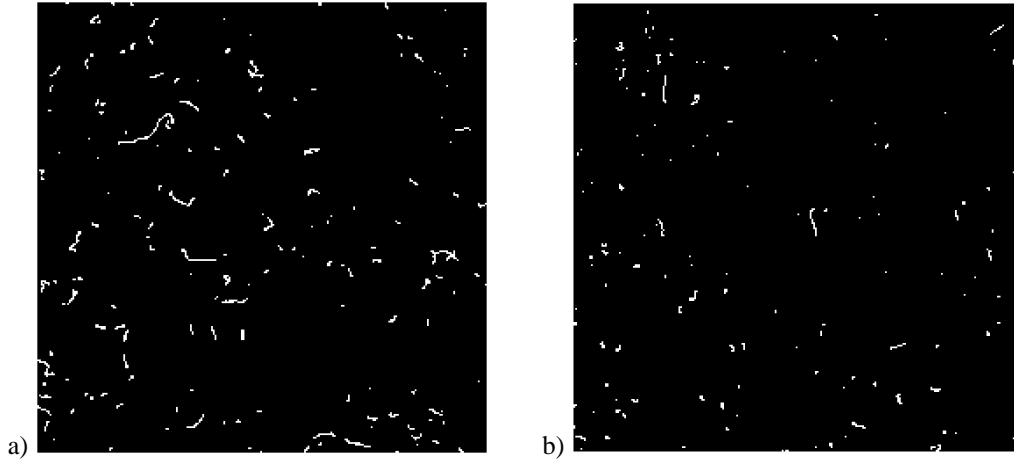
Figure 52. Response of the ATLAS-MPX detector of reference exposed to: a) ^{60}Co radiation source (1173 keV and 1333 keV photons), b) ^{137}Cs radiation source (662 keV photons). The mean length of the tracks is increasing with increasing incident photon energy.

5.5 Summary of the detection efficiency calibrations

The internal detection efficiency is defined as the probability that a particle which enters the detector volume generates an appropriate signal. The typical internal detection efficiencies of ATLAS-MPX devices with 300 μm thick silicon sensor for different radiation groups are:

- 100% for charged particles with energy deposition above ~8 keV per pixel (standard low threshold value).
- About 90% for 10 keV X-ray photons, 2% for 60 keV X-rays, 0.5% for 662 keV gamma-rays.
- About 0.1% for gamma photons with energy above 1 MeV.
- About 1% for slow neutrons of energy below 0.5 eV (given by the ^{6}LiF converter).
- About 0.1% for fast neutrons of energy in the 1 – 15 MeV range (given by the PE converter).
- 100% for minimum ionizing particles (MIPs). However, their correct categorization depends on the incidence angle. The minimal number of pixels in line necessary to be assigned to MIP depends on the track analysis algorithm.

5.6 Cluster analysis criteria

The correct recognition of the different species from the mixed radiation field depends also on the cluster analysis algorithm criteria. For the ATLAS-MPX experiment the criteria for cluster categories defined in subsection 3.4.1 were set as following:

- **Dot -** Clusters one pixel in size.
- **Small blob -** 2 - 4 pixel clusters with at most 2 pixels in line.
- **Heavy blob -** Cluster with at least one inner pixel and maximally 10% difference from ideal circle (radius calculated from the area and from the length of the border)

- **Heavy track -** Clusters with at least 3 inner pixels and 20% ratio between inner and border pixels.
- **Straight track -** Clusters with at least 20 pixels with at most 10% of pixel outside the track line.
- **Curly track -** All remaining clusters.

In some special cases the particle can generate cluster with the shape characteristic to the different particle species (i.e. electron can generate heavy blob cluster). The probability of such particle miscategorization was evaluated with ^{90}Sr electron source and ^{137}Cs and ^{60}Co gamma sources with the reference ATLAS-MPX device and is summarized in Tab. 4.

Source	Radiation type	Dot	Small blob	Curly track	Heavy blob	Heavy track	Straight track
^{90}Sr	Electrons	7%	22%	70%	1%	0%	0%
^{241}Am	Gamma	60%	39%	1%	0%	0%	0%
^{137}Cs	Gamma	25%	36%	38%	1%	0%	0%
^{60}Co	Gamma	17%	28%	54%	1%	0%	0%

Table 4. Automatic categorization for different radiation sources.

6. Evaluation of the ATLAS-MPX proton-proton collision data

This section summarizes the evaluation of the data measured by the ATLAS-MPX network during its operation from 2008 to 2011. Most of the results presented in this section are also part of the summary report prepared for submission as an internal note to the ATLAS community [32]. The data are being analyzed with the following aims:

- To separate the complex radiation field into several components.
- To understand and relate responses of all ATLAS-MPX detectors to the information on luminosity delivered by ATLAS.
- To analyze radiation background induced within collisions periods.
- To estimate level of radioactivity from the LHC operation.

6.1 History of ATLAS-MPX operation

The network of ATLAS-MPX detectors was installed in ATLAS UX15 experimental cavern in 2008. At that time, the network was consisting of 14 detectors. Since then, two more detectors were added to complete the present network of 16 devices.

6.1.1 Background radiation measurement

During 2008, before any collision period, measurements of background including cosmic muon clusters were performed to test the network operation stability. Fig. 53 shows the example of a background radiation measured in September 2008 with the MPX15 detector positioned close to LUCID[16] before any beam arrival. The number of different cluster type, as described in the subsection 3.4.1, per frame is shown as a function of time. The detector was operated in tracking mode with a threshold set at 10 keV and an exposure time of 600 s. Variations in cluster counts correspond to fluctuation of natural radioactivity and the average rate of all clusters was 2.6×10^{-2} s^{-1}.

---

[16] LUminosity measurement using a Cherenkov Integrating Detector
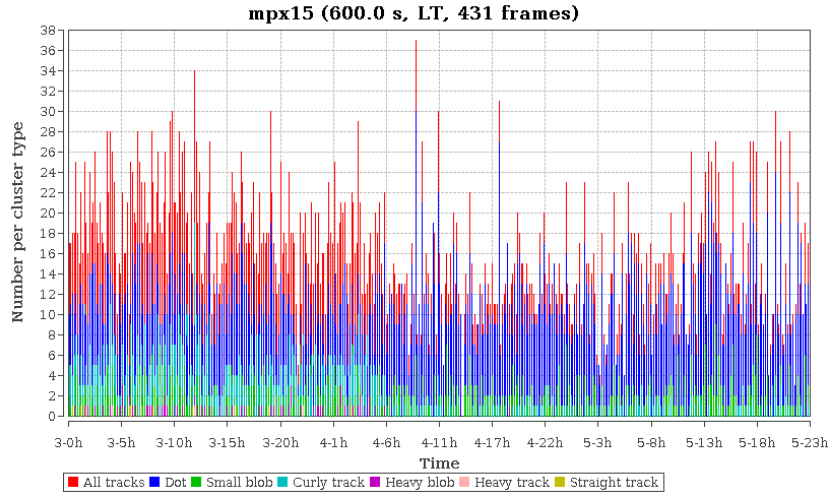
Figure 53. The background radiation in ATLAS measured with the MPX15 detector from 3rd to 6th September 2008 before any beam collisions period. The time scale is GMT.

6.1.2 First LHC beam arrivals

The correlation established between the recorded numbers of clusters of each species measured in ATLAS-MPX detectors and beam presence allows the direct observation with high sensitivity to any beam manipulation including arrival, set-up and adjustment. The first LHC beam arrival was in September 2008. The radiation level recorded by MPX15 on Wednesday 10th September 2008 is shown as a function of time in Fig. 54.
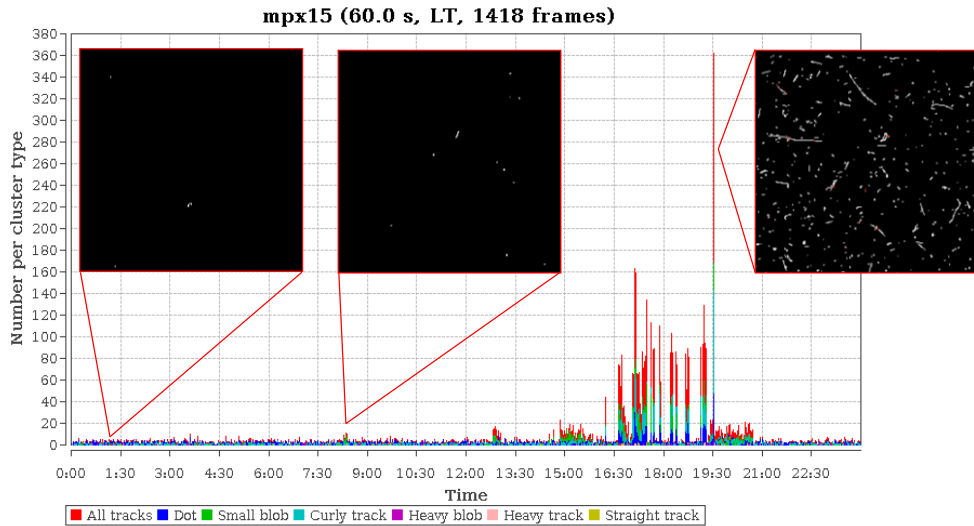
Figure 54. The first LHC beam arrival recorded by MPX15 on 10th September 2008. Three inserted images show in detail frames corresponding to no beam (left), a beam appearance (middle) and further increased cluster rate during beam operation (right). The exposure time was 60 s. The time scale is GMT.

The observation of clusters in MPX15 is correlated with beam arrival. The MPX15 was operated in tracking mode (low threshold of 10 keV and exposure time of 60 s). The

measured average count rate for all cluster types was 6.2×10^{-2} s^{-1} during the period 16:30 - 17:30 GMT what is twice higher than the average counting rate measured before any beam arrival. The detected number of clusters of all types measured on 10th September is shown as function of time with three inserts showing frames that correspond to no beam (background) and beam periods. The frame corresponding to beam period shows higher number of pixel hits with the occupancy so high that cluster overlapping already takes place (see red pixels in the Fig. 54 – right inserted image).

6.1.3 Collisions at 3.5 TeV

The first collisions at 3.5 TeV per beam were achieved on 30th March 2010. The response of MPX15 detector is shown in Fig. 55. The detector was operated with an exposure time of 30.0 s at low threshold which allowed the observation of all radiation species at this low luminosity regime.
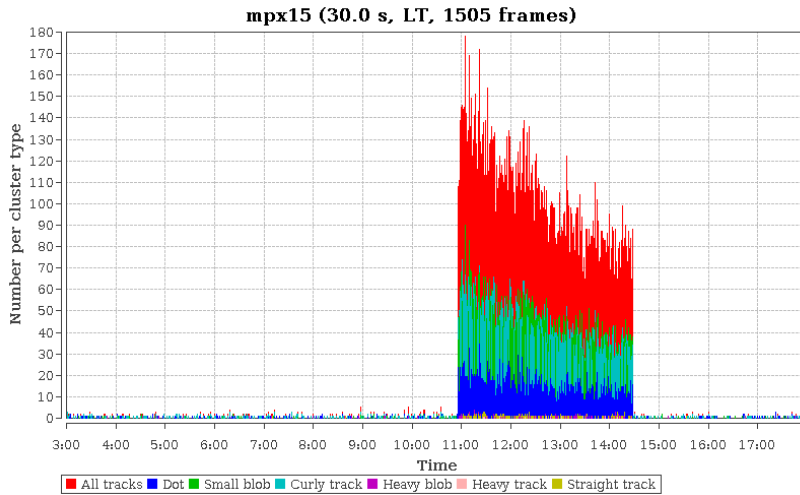
Figure 55. The first collisions at 3.5 TeV per beam on 30th March 2010 visualized with MPX15 (GMT scale).

6.1.4 Correlation of the cluster rate and the radiation intensity

The sensitivity of the ATLAS-MPX detectors to any LHC activities was demonstrated in previous subsections. Each ATLAS-MPX detector can measure in real-time at its position the radiation field that results from any proton-proton collision occurring at the ATLAS interaction point. Then, the detector response depends on the luminosity achieved by these collisions. The luminosity decay with time during a given run[17] shows a decreasing exponential behavior with a lifetime defined by various sources such as the decay of the intensities of the two beams, emittance growth and possible increase of the bunch length over the duration of the run. Then, the number of clusters per cm^2 counted with an ATLAS-MPX detector decreases with time following this exponential behavior from the time of the start until the end of the run.

---

[17] Run is the term used for specific collision period.

58

An example of the correlation between the response of the ATLAS-MPX detectors and the LHC luminosity is shown in Fig. 56a for the period from 21st April to 1st May 2011 and more detailed view in Fig. 56b for the period from 22nd May to 24th May 2011.

a)

b)
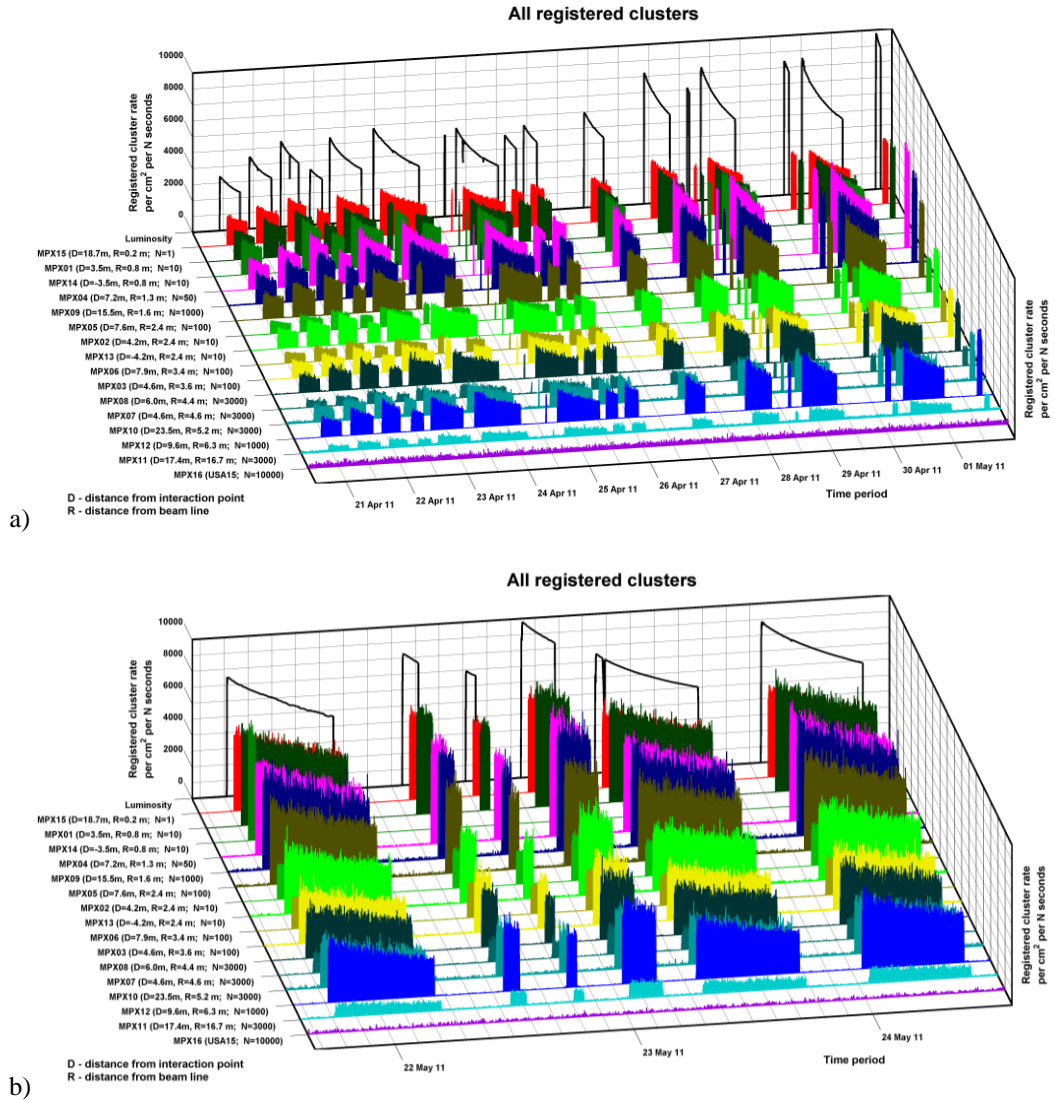
Figure 56. Registered clusters of all types (number of registered clusters per cm^2 per N seconds of measurement where N is stated in the plot) for all detectors with their positions given by their distance from beam line (R) and distance from the IP along the Z-axis (D). The black contours in the back plane of the figures indicate the LHC luminosity decreasing exponential behavior with time during the displayed selected periods of a) 21st April – 1st May 2011 and b) 22nd May – 24th May 2011.

The 3D plot of registered clusters of all types (number of registered clusters per cm^2) compares the response for all detectors with the luminosity achieved during the successive fills during this period. The black contours in the back plane of Fig. 56 indicate the LHC luminosity as measured by ATLAS.

6.2 Evaluation of the radiation field components in ATLAS

This subsection summarizes the evaluation of the complex radiation field in the UX15 cavern measured by ATLAS-MPX detectors. The original complex field has been separated into four main radiation categories as explained in section 3.4.1:

- **Low energy transfer particles (LETP)** are primarily photons and electrons visualized as dots, small blobs and curly tracks registered in the whole chip area.
- **High energy transfer particles (HETP)** are primarily protons and ions visualized as heavy blobs and heavy tracks registered in the whole chip area except for ^{6}LiF and border regions.
- **MIPs** are very energetic charged particles recognized as straight tracks registered in the whole chip area.
- **Thermal neutrons** are alpha particles and tritons identified as heavy blobs below the ^{6}LiF converter.

The values of the different radiation field components normalized per cm^2 and nb^{-1} are summarized in Tab. 5 and depicted in the Fig. 57-60.

Detector	Low energy transfer particles [clusters/cm².nb⁻¹]	High energy transfer particles [clusters/cm².nb⁻¹]	MIPs [clusters/cm².nb⁻¹]	Thermal neutron fluence [neutrons/cm².nb⁻¹]
MPX01	(5.98 ± 0.69) E+04	(6.68 ± 1.04) E+02	(1.21 ± 0.28) E+03	(4.59 ± 0.86) E+04
MPX02	(2.24 ± 0.19) E+02	(3.19 ± 0.29) E+00	(9.42 ± 0.85) E+00	(1.62 ± 0.17) E+03
MPX03	(3.08 ± 0.14) E+01	(4.84 ± 0.25) E-01	(8.88 ± 0.40) E-01	(2.73 ± 0.18) E+02
MPX04	(1.17 ± 0.05) E+02	(1.75 ± 0.07) E+00	(1.61 ± 0.13) E+00	(3.20 ± 0.18) E+03
MPX05	(4.77 ± 0.21) E+01	(5.03 ± 0.26) E-01	(4.79 ± 0.26) E-01	(7.36 ± 0.39) E+02
MPX06	(1.99 ± 0.10) E+01	(2.11 ± 0.14) E-01	(2.16 ± 0.17) E-01	(2.09 ± 0.12) E+02
MPX07	(4.44 ± 0.22) E-01	(4.14 ± 0.53) E-03	(9.39 ± 0.81) E-03	(6.58 ± 0.59) E+00
MPX08	(1.19 ± 0.06) E+00	(1.15 ± 0.10) E-02	(1.42 ± 0.14) E-02	(1.61 ± 0.09) E+01
MPX09	(5.86 ± 0.32) E+00	(8.64 ± 0.63) E-02	(2.45 ± 0.17) E-01	(2.84 ± 0.26) E+01
MPX10	(1.05 ± 0.06) E+00	(1.14 ± 0.09) E-02	(8.35 ± 0.76) E-03	(1.99 ± 0.13) E+01
MPX11	(3.02 ± 0.14) E-01	(6.31 ± 0.63) E-03	(2.39 ± 0.29) E-03	(2.86 ± 0.43) E+00
MPX12	(4.00 ± 0.19) E+00	(5.32 ± 0.33) E-02	(5.55 ± 0.51) E-02	(6.12 ± 0.32) E+01
MPX13	(3.75 ± 0.22) E+02	(5.27 ± 0.34) E+00	(1.46 ± 0.09) E+01	(2.69 ± 0.24) E+03
MPX14	(5.61 ± 0.65) E+04	(6.17 ± 0.81) E+02	(1.03 ± 0.16) E+03	(3.82 ± 1.21) E+04
MPX15	(2.59 ± 0.33) E+06	(1.20 ± 0.26) E+04	(1.57 ± 0.34) E+04	(3.81 ± 1.19) E+04
MPX16	(1.28 ± 0.94) E-03	(2.11 ± 1.38) E-04	(7.69 ± 4.63) E-05	(4.64 ± 4.72) E-02

Table 5. Radiation field components measured by ATLAS-MPX devices normalized to nb^{-1} as measured during operation in 2011. Low energy transfer particles represent primarily photons and electrons. High energy transfer particles represent primarily protons and ions.
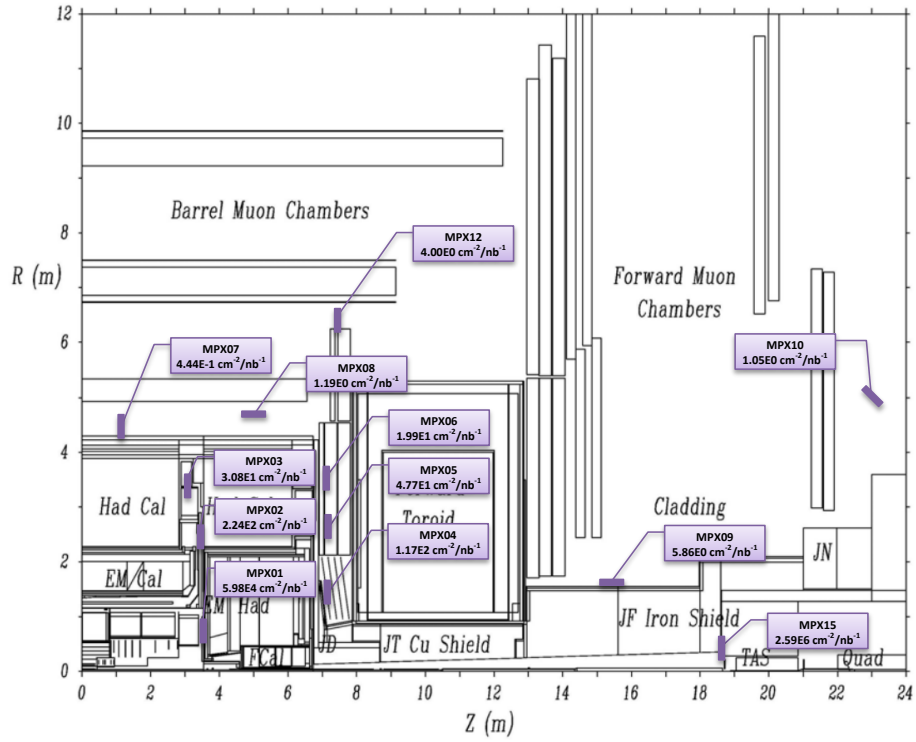
Figure 57. Map of the average cluster rate of low energy transfer particles (LETP) normalized per luminosity unit.
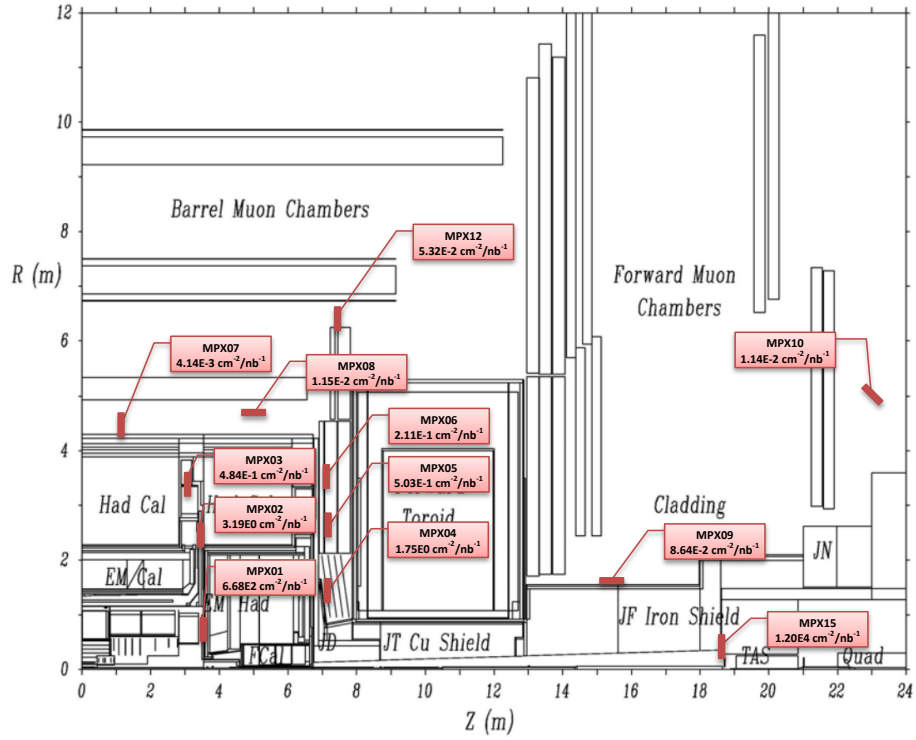
Figure 58. Map of the average cluster rate of high energy transfer particles (HETP) normalized per luminosity unit.
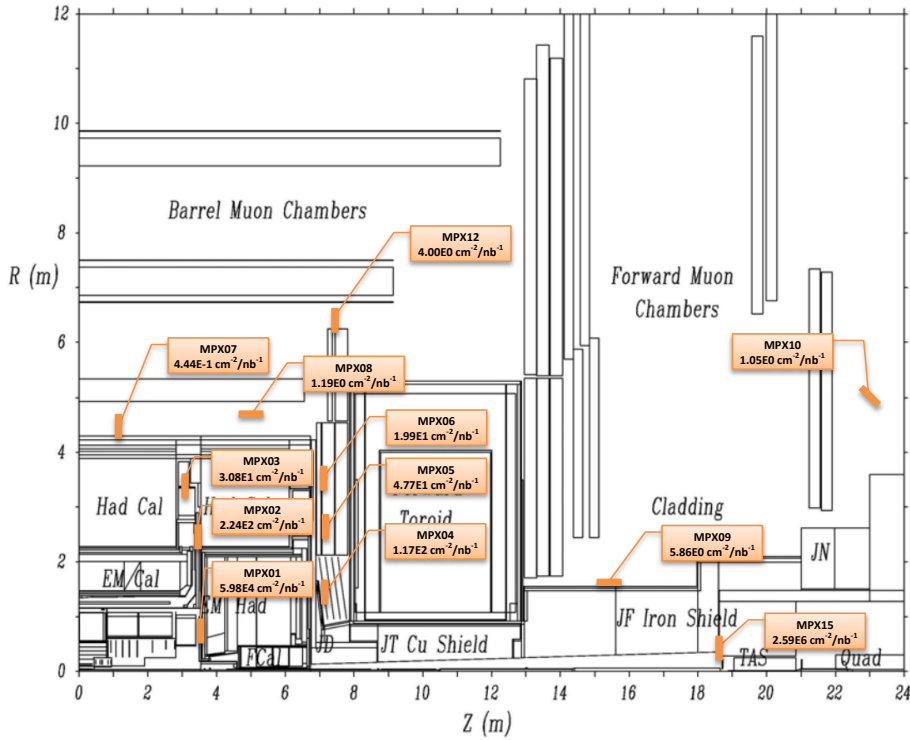
Figure 59. Map of the average cluster rate of minimum ionizing particles (MIP) normalized per luminosity unit.
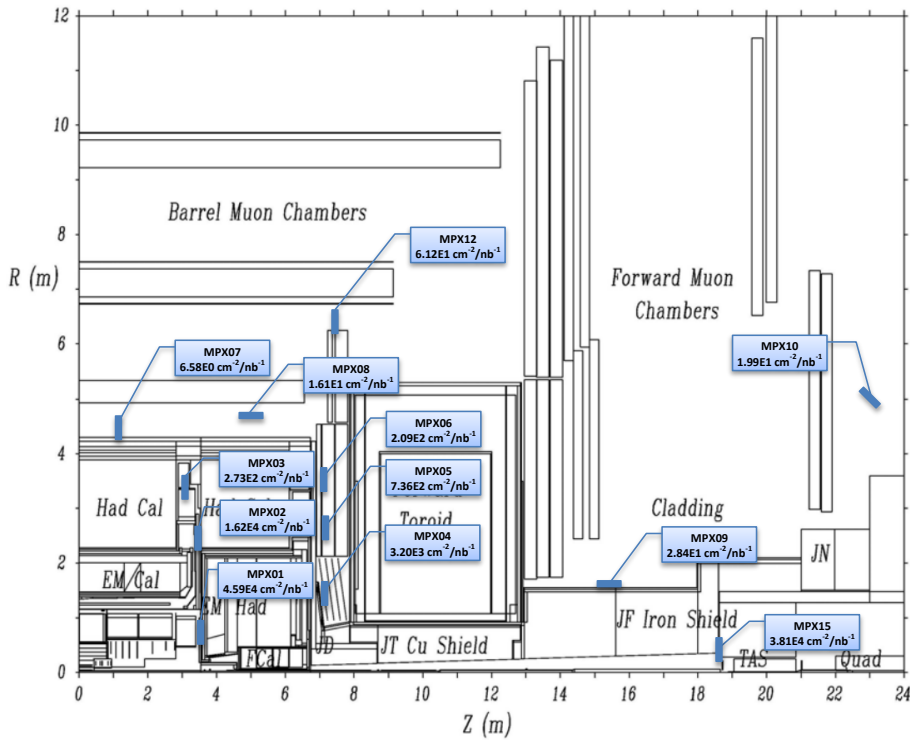
Figure 60. Map of the average thermal neutron fluence during collisions normalized per luminosity unit.

It is assumed that ratios of different radiation components are preserved in the wide range of luminosity with the corresponding fluxes or rates increasing linearly with luminosity. The thermal neutron fluence has been calculated under assumption of the isotropic thermalized field (except of MPX15) and the procedure is described in detail in subsection 7.5.

6.3 Dependence of the ATLAS-MPX detectors response on LHC luminosity

The data from 2010 and 2011 of the ATLAS-MPX network operation were analyzed with the aim to understand and relate responses of all ATLAS-MPX detectors to the information on luminosity delivered by LHC.

The luminosity $\mathcal{L}$ of a hadron collider can be determined from measured colliding beam parameters and expressed as:

$$\mathcal{L} = n_b n_1 n_2 \mathcal{L}_{spec} \tag{8}$$

where

$$\mathcal{L}_{spec} = \frac{f_r}{2\pi \Sigma_x \Sigma_y} \tag{9}$$

is the specific luminosity, n_b is the number of bunch crossings producing collisions per machine revolution, f_r is the machine revolution frequency (~11 kHz), n_1 and n_2 are the bunch populations (number of protons) in beam 1 and beam 2. Σ_x and Σ_y are the effective widths of the horizontal and vertical profiles of the colliding beams.

In the case of beam-beam collisions, one expects the ATLAS-MPX detector response to be proportional to the product intensity of the two bunch pairs collided in ATLAS interaction point (IP1). With proper calibration, ATLAS-MPX network is able to provide up to 15 independent luminosity measurements at different positions.

6.3.1 Luminosity measurement in tracking mode

Figure 61 show the MPX03 detector response during collisions. The detector was operated in the tracking mode with low energy threshold. Each point on the graph represents one run with the corresponding integral luminosity. The response (number of clusters $\times$ cm^{-2}) is a linear function of the integrated luminosity as measured by ATLAS detector for all cluster types.

The advantage of this evaluation method is that some particle types appears in significant amounts only during the collision period and therefore the signal to noise ratio (SNR) can be very high for this type of measurement. The drawback is the poor statistics because of the large dead time caused by the frequent data readout and short acquisition times (see section 4.3). These fact limits the usage of the cluster analysis for the measurement of the instantaneous luminosity as provided by several ATLAS luminosity detectors (LUCID[18], BCM[19]).

---

[18] LUminosity measurement using a Cherenkov Integrating Detector
[19] Beam Condition Monitor
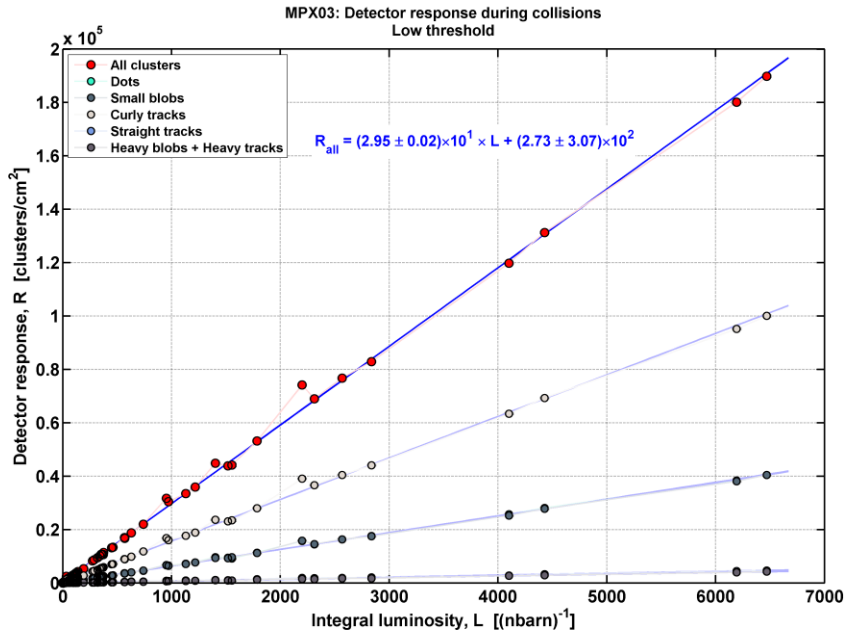
Figure 61. The MPX03 detector response recorded at low threshold (cluster $\times$ cm^{-2}) during collisions is shown as function of the integrated luminosity (nb^{-1}). The response recorded for the various types of clusters is a linear function of the integrated luminosity over a wide range of values.

To increase the statistic for the instantaneous luminosity measurements it is possible to analyze the collected frames in the counting mode. Instantaneous luminosity as measured by MPX02 using this method of data analysis compared to BCM data from run 189280 on 14th September 2011 is shown in Fig. 62. The statistics is still relatively low since the acquisition time of the MPX02 detector was only 200 ms what corresponds to the dead time of 97%. Large statistical fluctuations in the MPX02 data are clearly visible in Fig. 63 where the ratio of both luminosity measurements is presented.
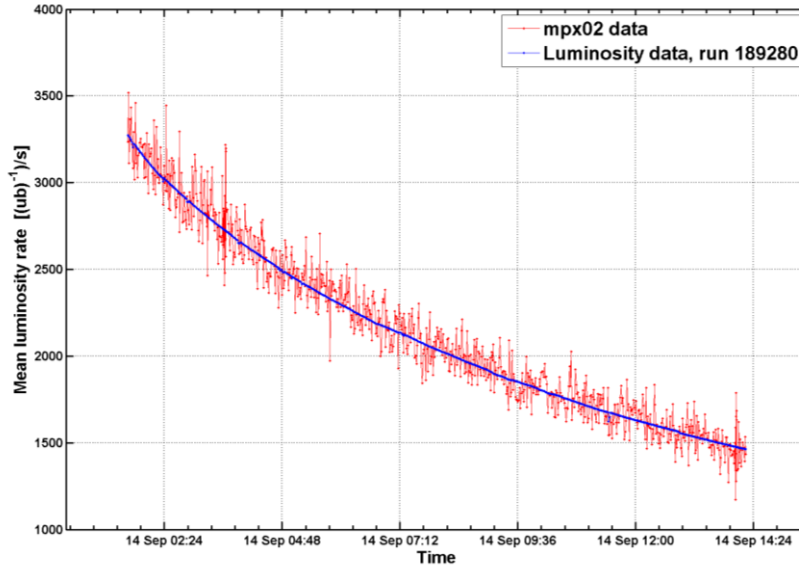
Figure 62. Comparison of the luminosity from run 189280 on 14th September 2011 as measured with MPX02 detector operating in the tracking mode with low threshold and BCM luminosity monitor. The acquisition time of the MPX02 was 200 ms, data were recalculated to the luminosity blocks and normalized to the luminosity block 433 (roughly in the middle of the curve).
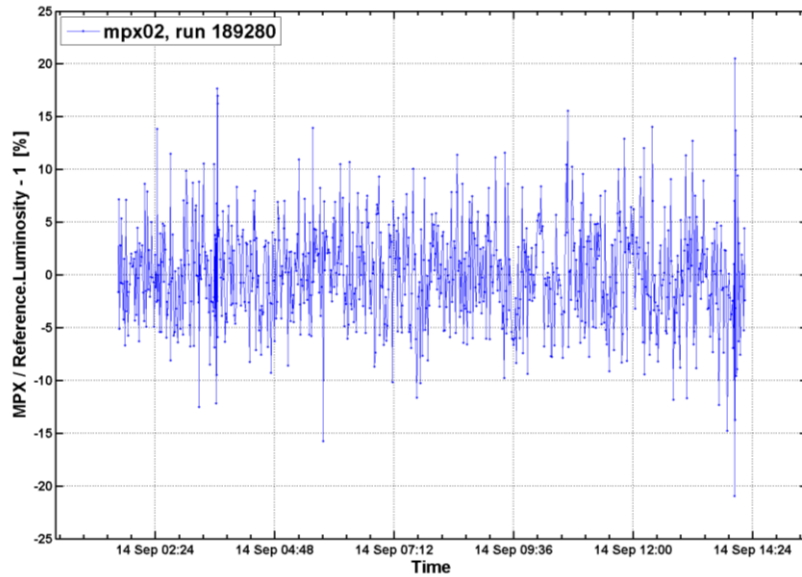
Figure 63. Ratio of the luminosity as measured with MPX02 detector and BCM luminosity monitor. Data comparison show large dispersion of ~20% because of the low statistic for MPX02.

6.3.2 Luminosity measurement in counting mode

Counting mode is the preferred operation mode in case of luminosity measurement. Instantaneous luminosity measured by MPX01 in counting mode with low threshold compared to BCM data from run 189280 on 14th September 2011 is shown in Fig. 64 with details visualized in Fig. 65. Several sharp drops in the instantaneous luminosity

demonstrate very good agreement of the ATLAS-MPX and BCM luminosity measurement.
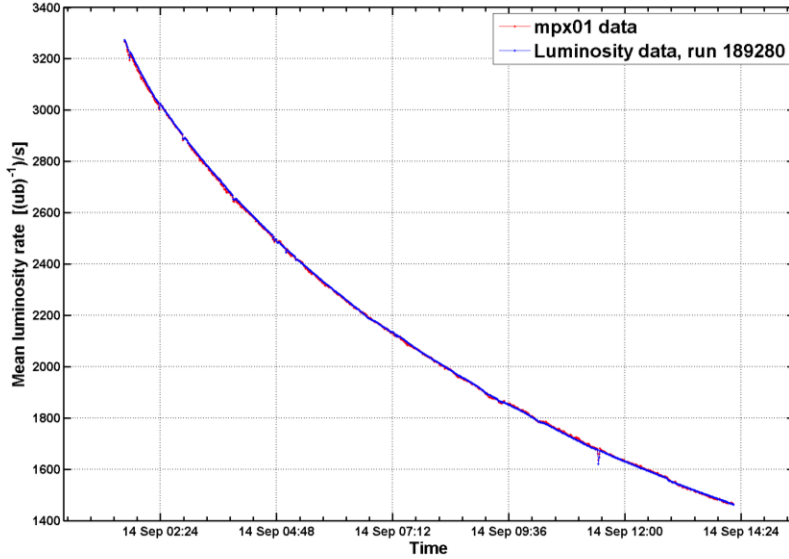
Figure 64. Comparison of the luminosity from run 189280 on 14th September 2011 as measured with MPX01 detector operating in the counting mode with low threshold and BCM luminosity monitor. The acquisition time of the MPX01 was 30 s, data were recalculated to the luminosity blocks and normalized to the luminosity block 433 (roughly in the middle of the curve).
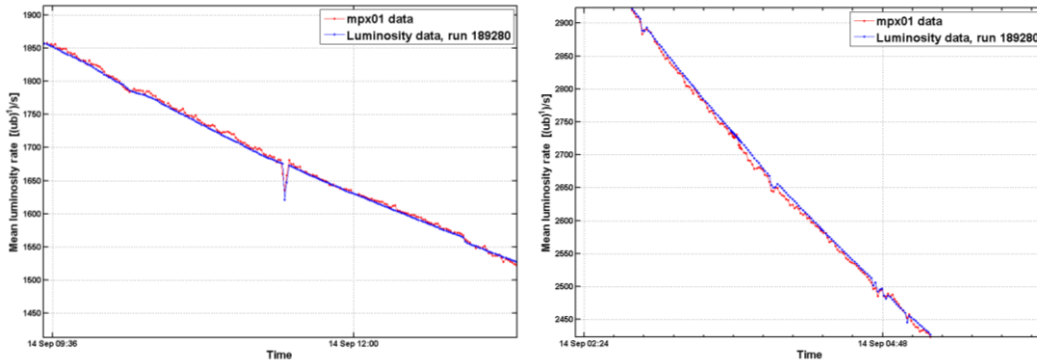
Figure 65. Details (zoom of Fig. 64) of the comparison of the luminosity from run 189280 as measured by MPX01 detector operating in the counting mode and BCM luminosity monitor. The acquisition time of the MPX01 was 30 s, data were recalculated to the luminosity blocks and normalized to the luminosity block 433.

The acquisition time of the MPX01 detector was only 30 s what corresponds to the dead time of 17%. The overall statistical fluctuations in the MPX02 data are below 1% as shown in Fig. 66. Such precise measurement allows investigating effects of higher orders like effect of induced radioactivity notable on the Fig. 66.
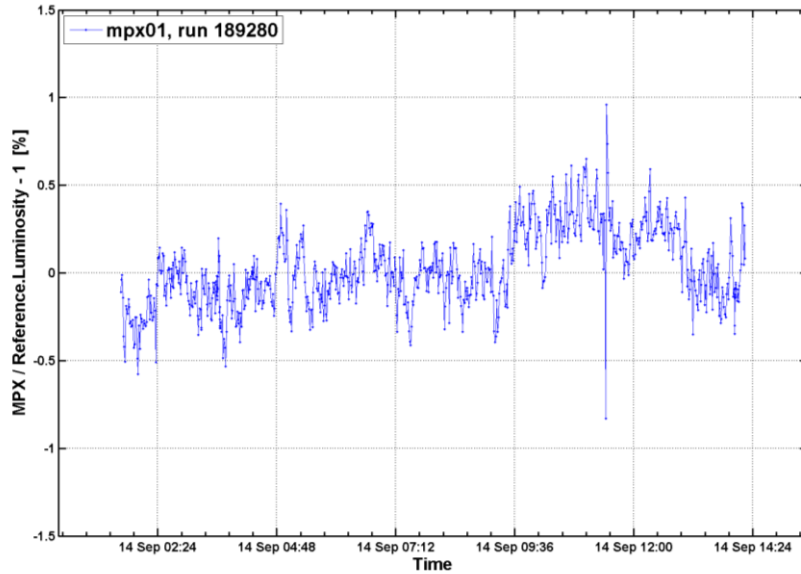
Figure 66. Ratio of the luminosity as measured with MPX01 detector and BCM luminosity monitor, respectively. The data of MPX01 detector has not been corrected for influence of induced radioactivity which is visible as decrease at the beginning of the plot and increase at the end of the plot. Data were recalculated to the luminosity blocks and normalized to the luminosity block 433 (roughly in the middle of the curve).

6.3.3 Observation of van der Meer scans

Van der Meer (VDM) scan is one of the key methods to determine absolute luminosity of the colliding beams by measuring the effective width of the horizontal and vertical profile of the beams Σ_x and Σ_y from the equation (9).

Measurement of these effective widths is done by recording the relative interaction rates as function of the transverse beam separation. At LHC, the scans are performed, at a given interaction point, by moving the beams step-wise with respect to each other in the two transverse planes, in horizontal (x) and in the vertical (y) direction. There were several VDM scans performed during the LHC operation in 2010 and 2011 as reported by the ATLAS Collaboration [33], [34].

ATLAS-MPX detectors positioned close to the beam axis, namely MPX01, MPX14 and MPX15, can directly visualize luminosity scans performed according to the VDM beam displacement method and permit an evaluation of the effective overlapping beam sizes and maximum collision rate. The cluster rates measured during these scans as a function of time appears as bell-shaped curves with their maximum achieved at a time corresponding to zero beam separation. Figure 67 shows, as a function of time, the clusters recorded with the MPX15 detector operating in the tracking mode at low threshold during luminosity scans done during fills 1059 (26th April 2010) and 1089 (9th May 2010). A horizontal scan followed by a vertical scan done during fill 1059 is observed in Fig. 67a. Figure 67b shows two horizontal scans followed by two vertical scans done during fill 1089.

a)

b)
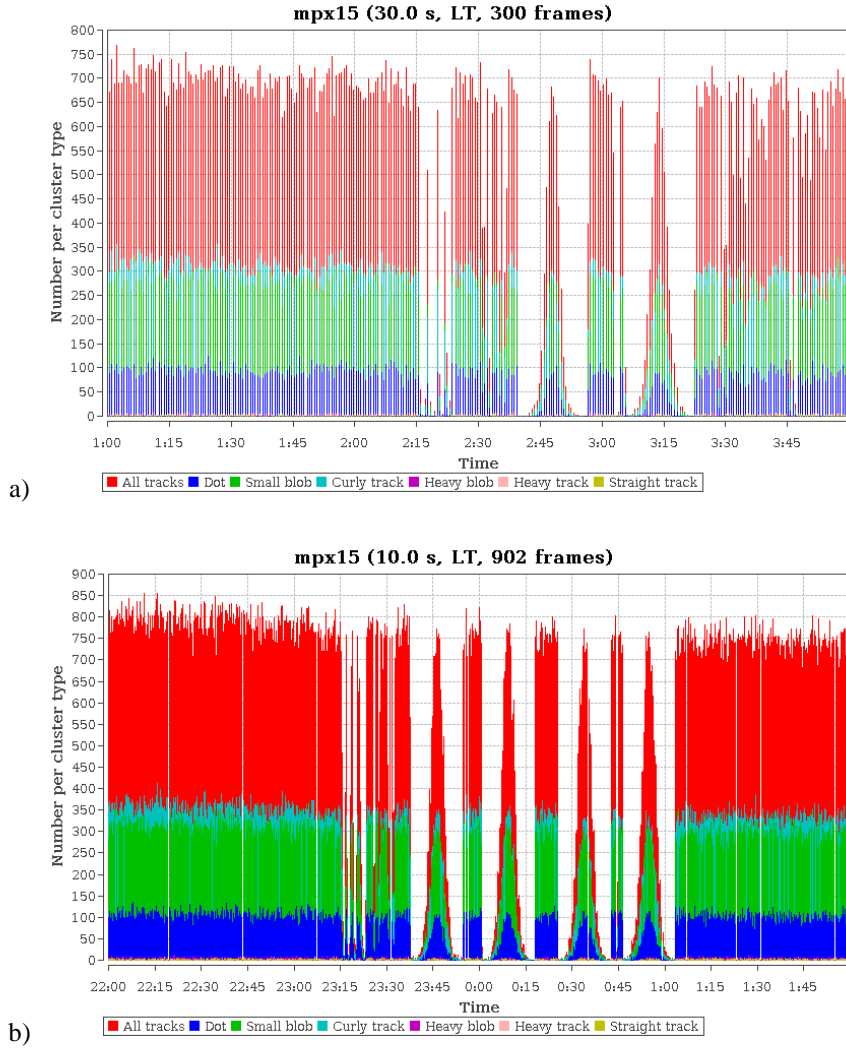
Figure 67. Van der Meer scans as observed with the detector MPX15 with threshold set at 10 keV. a) A horizontal scan followed by a vertical scan during fill 1059 on 26th April 2010 (GMT) with an acquisition time of 30 s. b) Two horizontal scans followed by two vertical scans during fill 1089 on 9th May 2010 (GMT) with an acquisition time of 10 s.

Gaussian fit of the first horizontal VDM scan of fill 1059 is shown in Fig. 68. Application of the fit procedure, gives the value of the effective horizontal profile σ_x of the overlapping beams in units of seconds (Fig. 68). The VDM luminosity scans method is measuring interaction rates as function of the beam separation (expressed in microns), so the σ_x measurement can be translated from time units into length units expressing beam separation Σ_x from the equation (9). Values of Σ_x obtained from horizontal scan and Σ_y from the vertical scan can be used to calculate the luminosity $\mathcal{L}$ of the collider using equations (8) and (9). However, detailed evaluation of the VDM scans is outside the scope of this thesis and it is presented in the comprehensive ATLAS-MPX summary report [32].
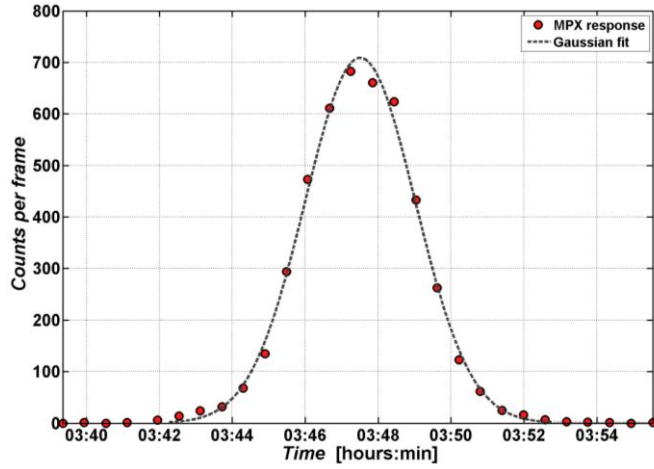
Figure 68. Gaussian fitted to the cluster rates measured with MPX15 as function of time during first horizontal VDM scan of fill 1059.

With the continuing increase of bunches in the accelerated beams, the ATLAS-MPX detectors exposure time had to be shortened in order to avoid cluster overlapping in the tracking mode data. This leads to very short exposure time and large dead time. Moreover, for the luminosity evaluation the information on the radiation composition is not needed and therefore it is better to use counting mode of operation to increase the measurement statistics.

For this reason the MPX15 detector was set to counting mode (low threshold with 10 s exposure time) during the van der Meer luminosity scan on 15th May 2011. Figure 69 shows measured counting rates (sum of the pixel counts for whole detector) with very good statistics. Corresponding Gaussian fit of the first vertical VDM scan is depicted in Fig. 70.
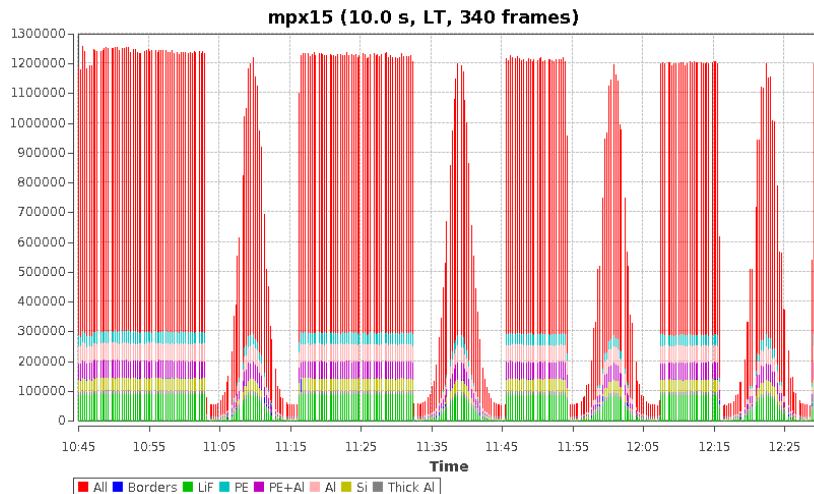
Figure 69. Van der Meer scans as observed with the detector MPX15 running in counting mode during fill 1783. The scans were done on 15th May 2011. Two horizontal and two vertical scans are visualized. The detector threshold was set at 10 keV and measurements were performed with a frame length time of 10 s.

69
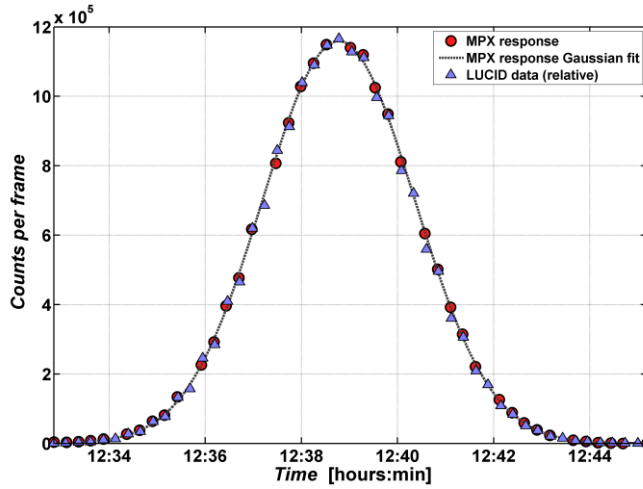
Figure 70. Gaussian fitted to the count rates measured with MPX15 as function of time during first vertical VDM scan of fill 1783. Scaled LUCID readings (blue triangles) are compared to MPX15 data (red circles).

6.4 Activation of the environment

The interactions of primary and secondary particles with materials in the environment of the ATLAS experiment produce large amounts of neutrons and material activation, including detectors and their electronics. The size and effective duration of the generated activation depends on the activation cross sections, radionuclides half-life and their decay branching ratios, mainly gamma emissions. The activation of particular objects depends on their material composition as well as on their geometry and location within the ATLAS environment. The activation is expected to grow with machine luminosity and duration of LHC operation. Due to their sensitivity to electrons and gamma-rays, ATLAS-MPX detectors can measure the radioactive decays and activation is observed at the end of fills with most ATLAS-MPX detectors.

The ATLAS-MPX detectors become themselves activated as the result of the interaction of particles with the silicon layer, surrounding electronic components and duralumin protective box. However, ATLAS-MPX devices are, in most cases, surrounded by a large amount of material and therefore self-activation contribution is negligible. Precise evaluation of the self-activation will be done experimentally in reactor during foreseen LHC shutdown when there will be possibility to remove some devices from the UX15 cavern.

Figure 71a shows the measured rate of different cluster types as measured with the MPX04 detector between 20th April 2011 and 6th May 2011. Figure 71b shows the detail of Fig. 71a. Both exponential increase of a long decay component of induced activity due to the first fill and decrease after the last fill (highlighted with a black curve in Fig. 71b of the selected period are clearly visible.
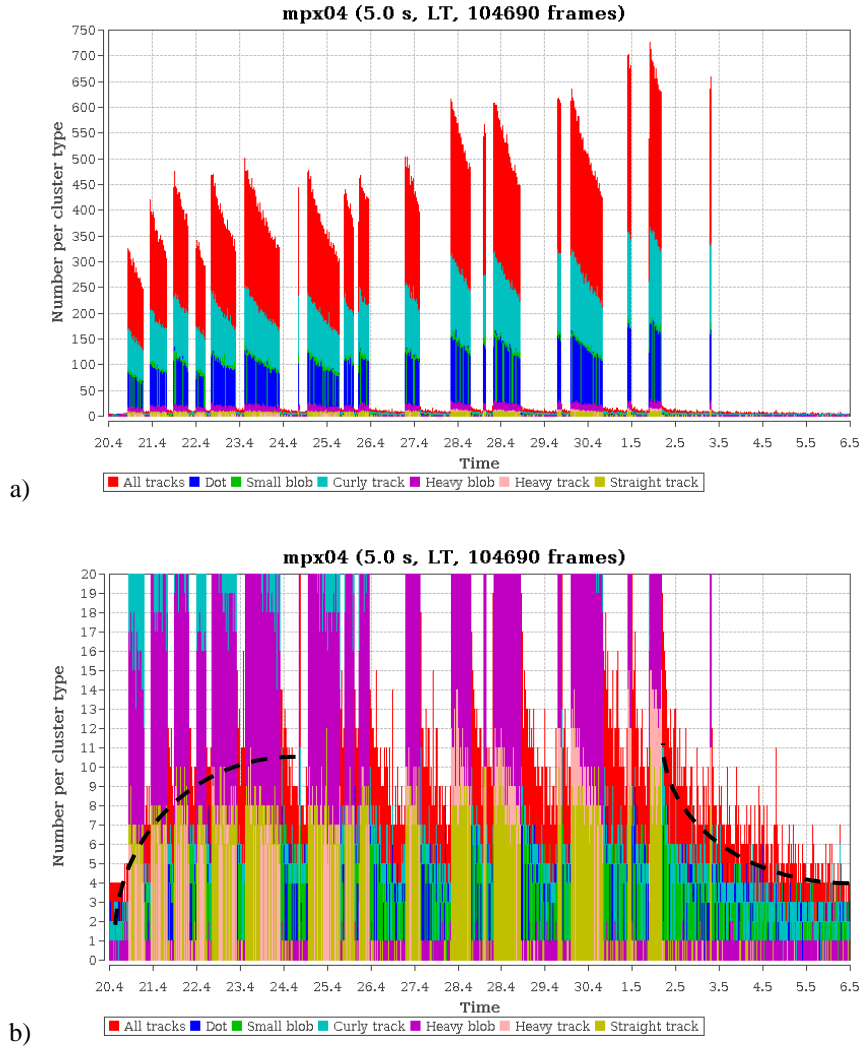
Figure 71. a) Cluster rate of different cluster types as measured with MPX04 device between 20th April and 6th May 2011. b) Detail of the previous figure. The exponential increase of induced activity of the long decay component due to the first fills and decrease after the last fills are clearly visible (highlighted by black dashed curve).

The detailed composition of the measured rate of the different cluster types recorded by MPX04 is shown in Fig. 72 for 7 runs performed during the period from 27th May 2011 (12:00) to 31st May.2011 (12:00). On 30th May 2011 from 10:00 to 24:00 (5484 frames between run 5 and 6 shown on the Fig. 72) the MPX04 detector measured 2694 dots, 2554 small blobs and 3323 curly tracks but only 82 heavy blobs, 2 heavy tracks and 6 straight tracks. From this figures, it is observed that the signal measured in between beam collision periods is caused almost solely by electrons and photons.
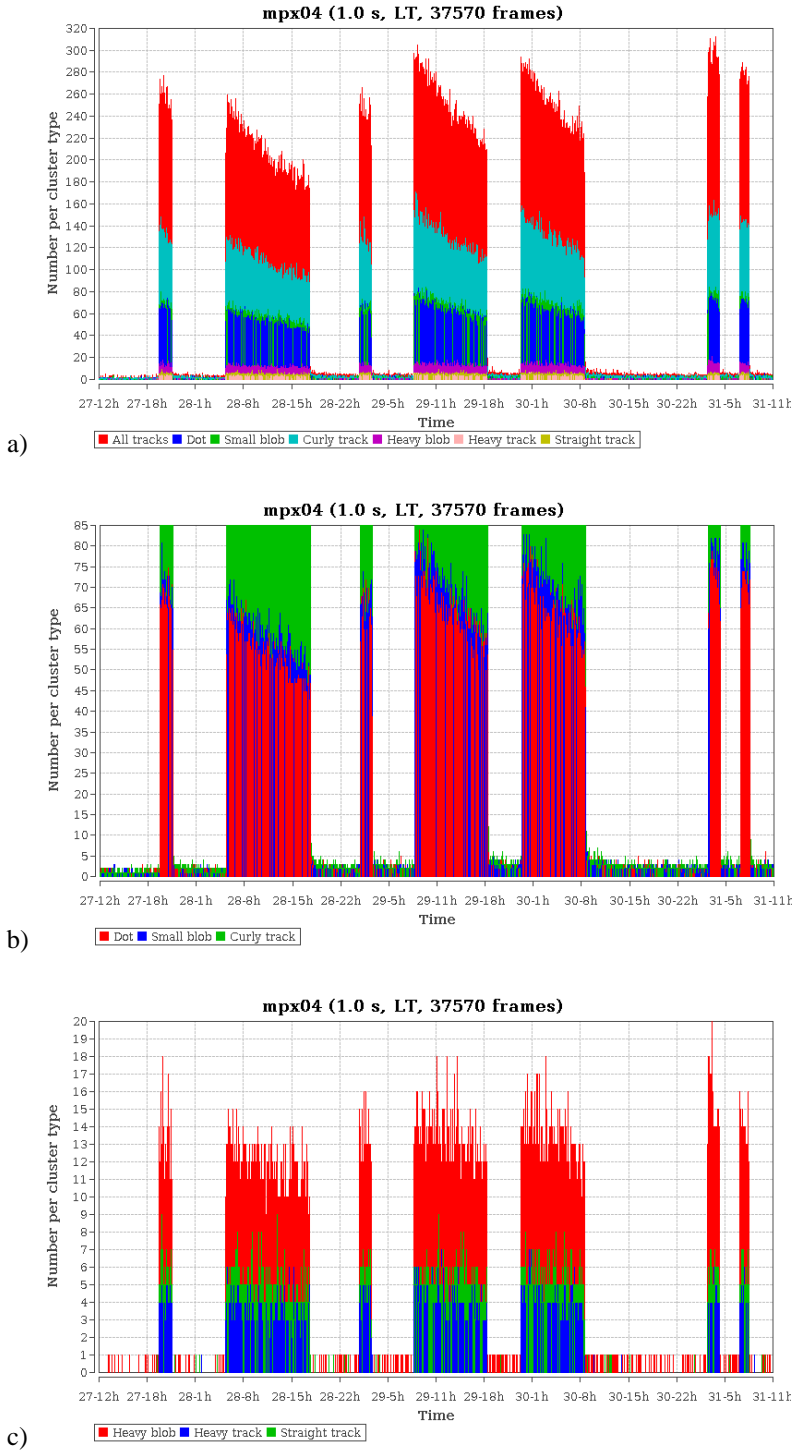
Figure 72. Cluster rates of different cluster types measured by MPX04 between 27th May 2011 (12:00) and 31st May 2011 (12:00). Seven runs were observed during this time period corresponding to 7 columns in each figure. a) All clusters types. b) Clusters from low energy transfer particles. c) Clusters from high energy transfer and MIP particles. Signal outside the collision period is caused almost only by low energy transfer particles (photons and electrons).

6.4.1 Evaluation of the decay components

The induced activation as measured with an MPX detector can be further analyzed in terms of short and long decay components. Induced radiation background level generally depends on the luminosity rate, the integrated luminosity, and the total time over which the luminosity is integrated. An example of activation seen in detector MPX04 is shown in Fig. 73 with the count rates measured after the end of collisions.
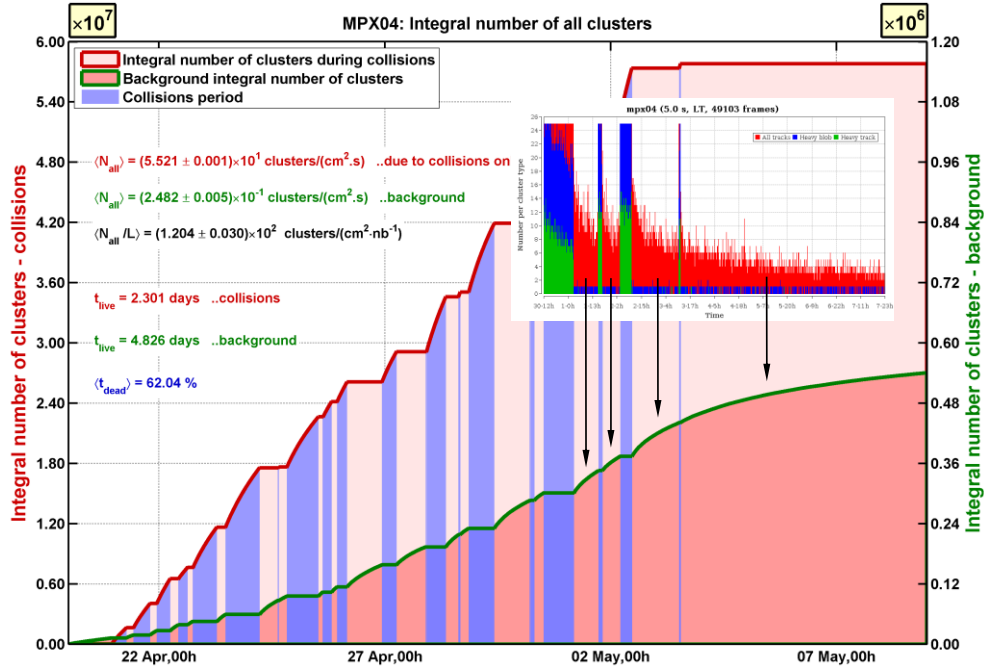
Figure 73. Example of environment activation observed in MPX04 in April and May 2011 as shown on measured cluster rate (inserted frame) and in a plot representing the integral number of clusters measured during no-beam periods (green line). Beam periods are highlighted by blue columns. The observed activation corresponds to an integrated luminosity of 230 pb^{-1} with mean luminosity rate of 0.5 nb^{-1}.s^{-1} (between 20th April – 3rd May 2011).

More detailed look on the cluster rates measured by MPX04 after 2nd May 2011 depicted in Fig. 74 show three main decay components:

1) **Very short component** is visible in first minutes just after the end of collisions during fills 1755 and especially 1756 as demonstrated in two detailed figures in Fig. 74. Along the fast component, the count rate is initially two orders of magnitude higher than the background count rate as measured before any collision in 2008 with the same detectors.

2) **Short component** is observable during couple hours after and of collisions during fill 1755

3) **Long component** decays over days after the end of collisions during fills 1755 and 1756.
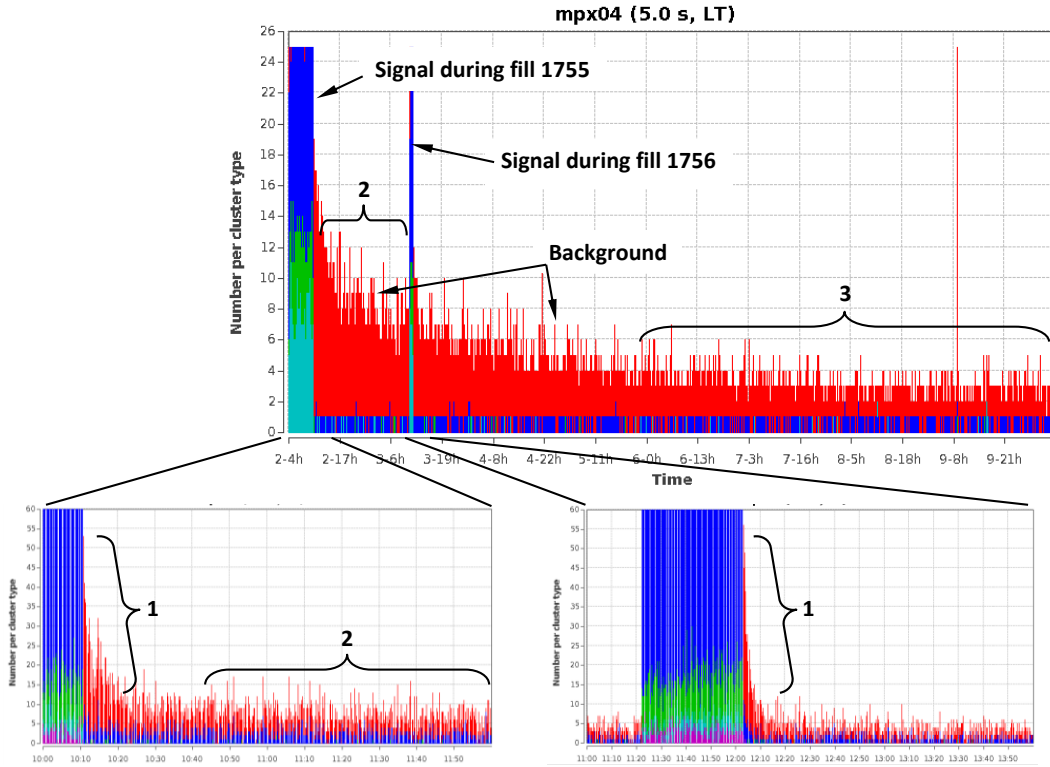
Figure 74. Measured background signal in MPX04 from the end of fill 1755 on 2nd May to 10th May 2011. Two detailed figures show the signal measured just after the end of beam collisions (fills 1755 and 1756). The shortest decay component numbered by 1 is especially visible just after the very short fill 1756 where radionuclides with a longer half-life have not yet been created with large activity (fill 1756 length 43 min, integrated luminosity 1590 nb[-1], mean luminosity rate 0.62 nb[-1].s[-1]). Colors represent different cluster types to visually distinguish collision periods (blue/green columns over the whole height of the plots) from background signal produced by X-rays, gamma-rays and electrons (red color).

Different decay components as labeled above are fitted by exponential function

$$f = B + C.e^{-\lambda t} \tag{10}$$

where $\lambda = \ln 2/T_{1/2}$, B is a constant background level, C is a normalization constant, f is a mean number of clusters per frame and $T_{1/2}$ is the half-life. The results of the fits are shown in Fig. 75. Beside this, in MPX15 measurements, the additional very long decay component is visible with the half-life more than 50 days (see Fig. 75d). The half-lives of the different decay components as observed on the position of MPX04 and MPX15 detector are following:

1) **Very short component** - 1.6 min
2) **Short component** - 4 hours
3) **Long component** - 32 hours
4) **Very long component** - 50 days (observed with MPX15)
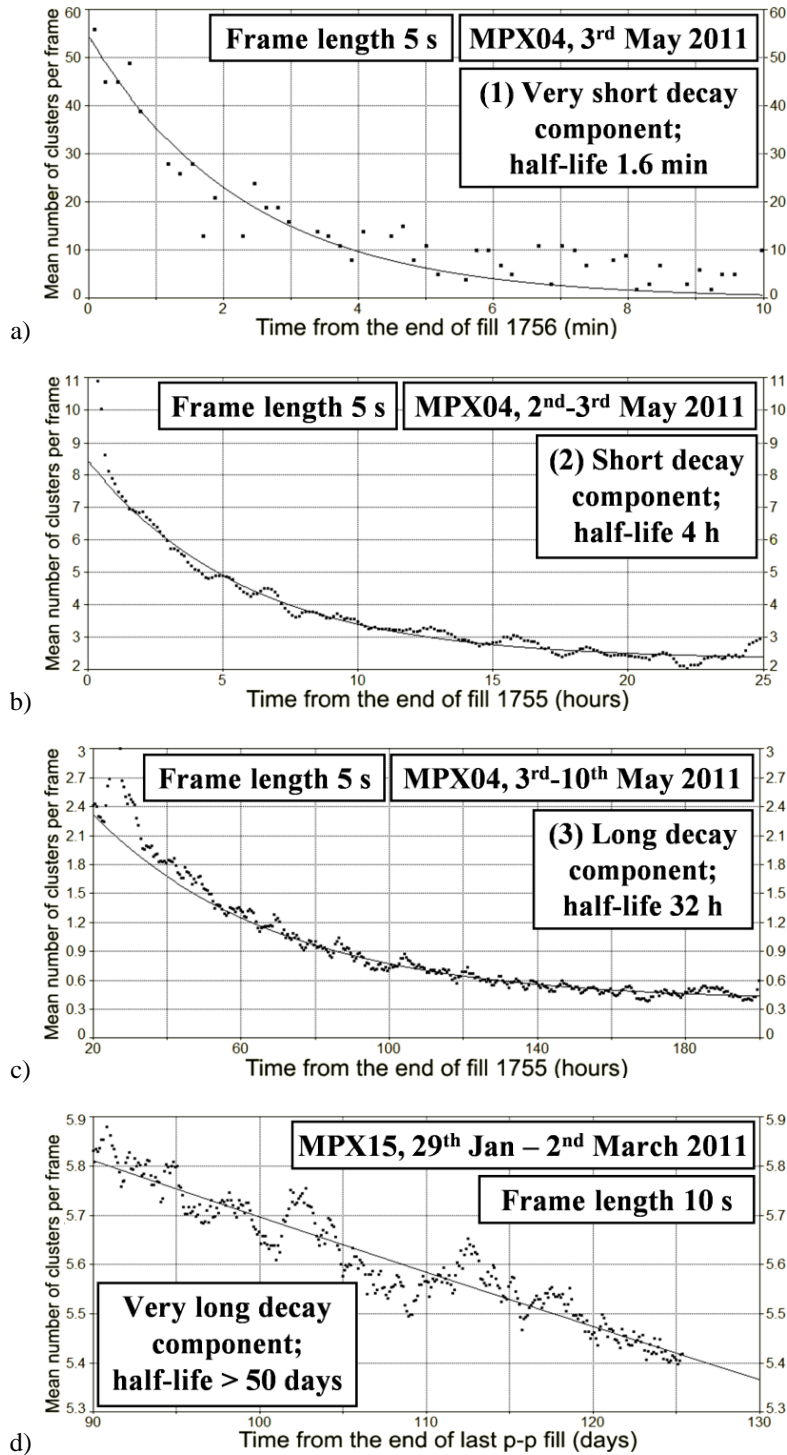
Figure 75. Exponential fits to the measured individual radionuclide decay components. Figures a), b) and c) present fits of components highlighted by 1), 2) and 3) in Fig. 74 as measured by MPX04 between 2nd May and 10th May 2011. In figure d) the MPX15 measurement of background during no-beam period between 29th January and 2nd March 2011 shows the very long radionuclide decay component. Measured signal in figures b), c) and d) has been smoothed (arithmetic mean of measured cluster rate).

6.5 Evaluation of the dose rate from induced radiation

For the purposes of radiation protection in ATLAS it is necessary to have quantitative estimation of the induced radiation background. To estimate the conversion factor between measured rate of clusters to the rate of ambient dose equivalent H*(10) used in the radiation protection the ATLAS-MPX reference detectors were exposed to ^{137}Cs (energy 662 keV) and ^{60}Co (energies of 1173 keV and 1332 keV) photon sources in separate measurements as described in subsection 5.4.

Figure 76 illustrates the increase of the radiation background as measured by MPX01 after fill 1309 on 30th August 2010.
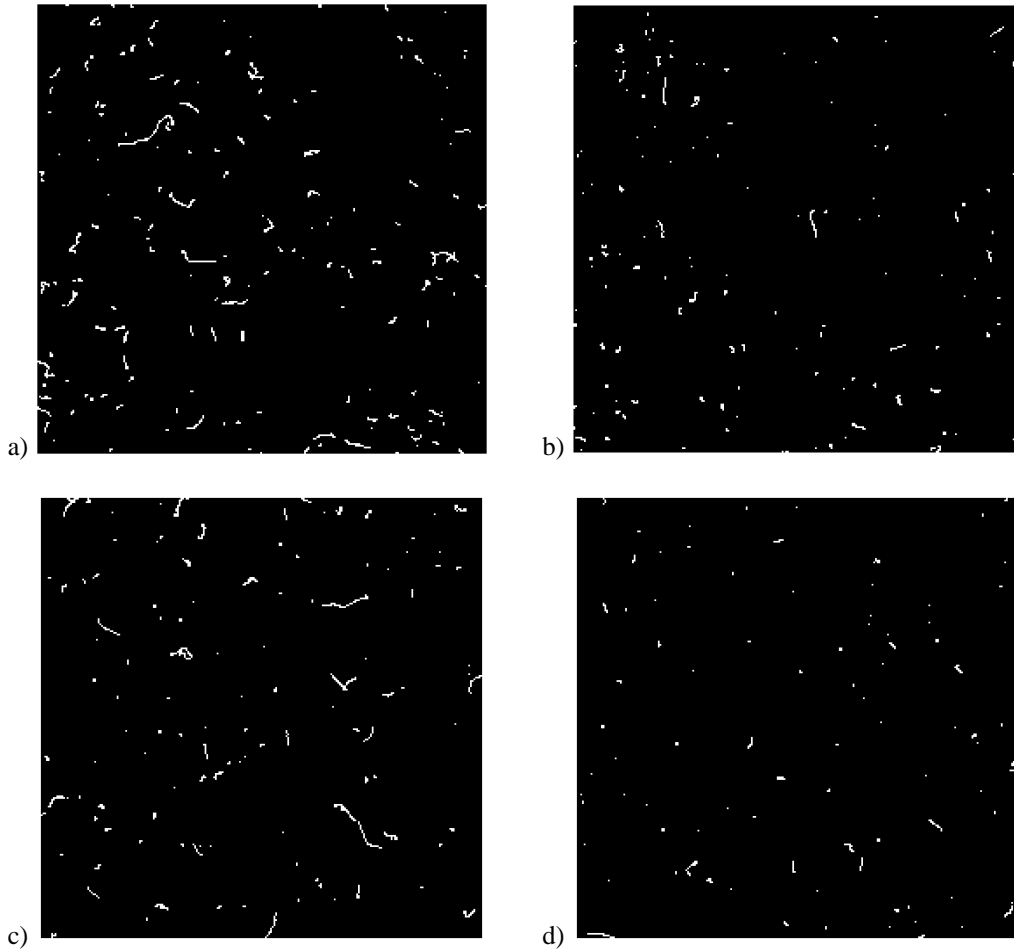
Figure 76. Response of an ATLAS-MPX detector of reference exposed to: a) ^{60}Co radiation source (1173 keV and 1333 keV photons), b) ^{137}Cs radiation source (662 keV photons). The mean length of the tracks is increasing with increasing incident photon energy. Comparison with the response of the MPX01 device recorded after end of collisions (fill 1309 on 30th August 2010). c) Integration during first 15 min after the collision (1 min lifetime) shows composition similar to the ^{60}Co. d) Integration during next 15 min (1 min lifetime) shows composition similar to the ^{137}Cs.

By applying the pattern recognition procedure during the first 15 minutes after the end of collisions (see Fig. 76c) it was observed that 54% of events measured with MPX01 consist of dots and small blobs and 46% of events correspond to curly tracks. By

comparing this ratio with the ^{60}Co calibration test measurements summarized in Tab. 4, one can see that the MPX01 track composition is similar to the response of the ATLAS-MPX detector of reference exposed to the ^{60}Co source (Fig. 76a). Using the ^{60}Co calibration coefficient the resulting mean H*(10) rate is 1.53 µSv.h^{-1}.

During second period of 15 minutes after the end of collisions the composition of the clusters measured by MPX01 consists of 72% dots and small blobs and 28% of curly tracks similarly to the ^{137}Cs response. Using the ^{137}Cs calibration coefficient the mean H*(10) rate for MPX01 detector during this time period is estimated to be 0.78 µSv.h^{-1}.

Figure 77 shows the decrease of the ambient dose rate equivalent as measured by MPX02 during a period of 13 days after the end of fill 1901 (integrated luminosity 46.5 pb^{-1}, mean luminosity rate 3.4 pb^{-1}.h^{-1}).
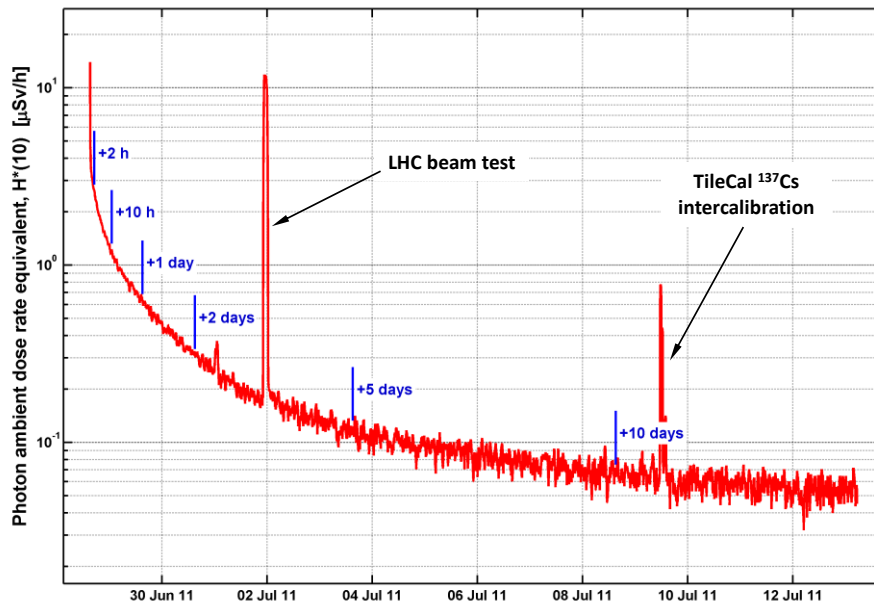
Figure 77. Decrease of the ambient dose rate equivalent as measured by MPX02 during 13 day period after the end of fill 1901 (integrated luminosity 46.5 pb^{-1}, mean luminosity rate 3.4 pb^{-1}.h^{-1}). Marks represent time from the end of the fill.

6.5.1 Ambient dose equivalent rate in ATLAS after 2 days of cool down

This subsection summarizes the dose equivalent rate H*(10) (see Appendix B) caused by induced activity as determined with ATLAS-MPX detectors during 10 hours between 19th – 20th October 2011 after fill 2222 with the integrated luminosity of 4.2×10^{4} nb^{-1} and mean luminosity rate 10.3 pb^{-1}.h^{-1}. Total integrated luminosity from first collisions in 2010 till the end of fill 2222 was 5.3 fb^{-1}.

The average value of 2.0×10^{-10} Sv.cluster^{-1}, calculated from the calibration coefficients from subsection 5.4, was used to convert measured cluster rate into H*(10) rate presented in Tab. 6 and Fig. 78. Note that the natural radiation background measured by all ATLAS-MPX detectors in September 2008 was ranging from 0.01 to 0.04 µSv.h^{-1}.

Detector	H*(10) rate [μSv/h]	Detector	H*(10) rate [μSv/h]
MPX01	34.3	MPX09	0.082
MPX02	0.72	MPX10	0.047
MPX03	0.17	MPX11	0.048
MPX04	NA*	MPX12	0.044
MPX05	0.37	MPX13	1.25
MPX06	0.16	MPX14	NA*
MPX07	0.015	MPX15	NA*
MPX08	0.014	MPX16	0.023

*These devices were set to high threshold mode of operation being insensitive to low energy transfer particles.

Table 6. Mean ambient dose equivalent rate H*(10) as measured by ATLAS-MPX detector network after a 2 days period of cool down (averaged in the period of 10 hours during 19th-20th October 2011).
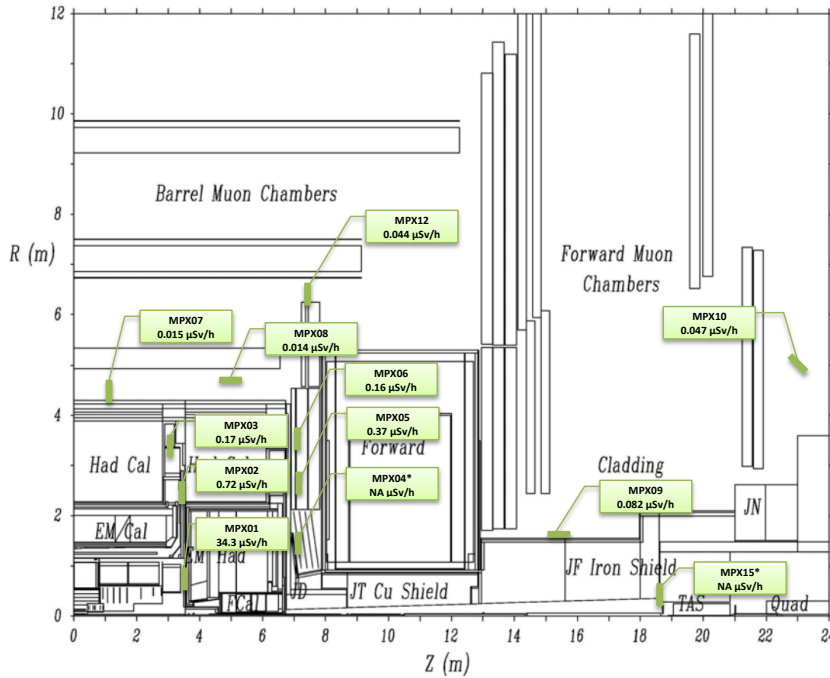
Figure 78. Mean ambient dose equivalent rate H*(10) map as measured by ATLAS-MPX detector network after a 2 days period of cool down (averaged in the period of 10 hours during 19th-20th October 2011). Devices marked with * were set to high threshold mode of operation being insensitive to low energy transfer particles

7. Comparison of the ATLAS-MPX measurements with simulations

This section presents the first comparison of the measurements obtained by operating the ATLAS-MPX detectors in tracking mode at low threshold and Monte Carlo simulations. This comparison is presented in more detail also as a part of the comprehensive report submitted as an internal note to the ATLAS community [32]. The comparison has been done for the four main particle categories which have been introduced before (see section 3.4.1 for detailed description):

- **Low energy transfer particles (LETP)** are visualized as sum of dots, small blobs and curly tracks registered in the whole chip area.
- **High energy transfer particles (HETP)** are visualized as heavy blobs and heavy tracks registered in the whole chip area except for ^{6}LiF and border regions.
- **MIPs** are recognized as sum of straight tracks registered in the whole chip area.
- **Thermal neutrons** are identified by heavy blobs below the ^{6}LiF converter.

ATLAS-MPX results obtained during collisions are normalized to the luminosity unit (nb^{-1}). The luminosity data used for the normalization comes from the LUCID and BCM measurements as an ATLAS preferred luminosity monitors.

7.1 Monte Carlo calculations

ATLAS-MPX measurements were compared to two different Monte Carlo simulations. The first Monte Carlo simulated data were obtained from the Radiation Background Task Force web page [35]. The simulations were done in 2003 using GCALOR package for GEANT3 with the Baseline Shielding Layout geometry of January 2003 and resulted in 2D maps of flux of different types of particle in ATLAS detector. These simulated 2D distributions were compared to the interpolated ATLAS-MPX measurement data to graphically visualize the match between both results.

The second Monte Carlo data were obtained from Mike Shupe in 2010 [36]. Simulations were performed with a PHOJET Geant3/GCALOR Monte Carlo code especially for ATLAS-MPX detectors locations. The simulations followed all particles

created in proton-proton interactions at $\sqrt{s} = 7$ TeV and any subsequent interactions along their path through the ATLAS cavern up to their absorption. Every particle crossing the scoring volume was recorded and its type, energy, position and direction vector were stored in a file. Thermal neutron flux and neutron spectral flux distribution presented in this section were obtained from information stored in these files. Data obtained from these simulations were used for comparison with measurement results of each individual ATLAS-MPX detector.

7.2 Low energy transfer particles

The spatial distribution of low energy transfer particles (LETP) cluster rate per luminosity unit as measured with the ATLAS-MPX detectors is shown in Fig. 79a as a function of the distance R from the beam axis and the coordinate Z along the beam axis, from the interaction point (IP1). The lowest cluster rate per luminosity unit is recorded with the detector MPX11 which is located on the UX15 cavern wall (see Tab. 2). The highest cluster rate per luminosity unit is recorded with MPX15 (closest to the beam axis, along LUCID).

Fig. 79b shows the distribution of electrons determined by GCALOR simulations. Only a rough comparison with simulated data can be done because the LETP particles measured with ATLAS-MPX detectors include signal from electrons and signal from gamma and X-rays interacting is the ATLAS-MPX sensor as well as contribution from MIPs hitting the sensor surface perpendicularly. Especially the photon contribution cannot be distinguished correctly without additional MC simulations.

To include roughly the contribution of photons in the LETP comparison a 1% photon detection efficiency (rough average estimate through the whole photon energy spectrum – see section 5.2) is assumed. The summary of ATLAS-MPX measurements compared to GCALOR simulations is presented in Tab. 7. It can be said that the measured LETP average cluster rate is in fair agreement with the GCALOR prediction of electron and photon currents.
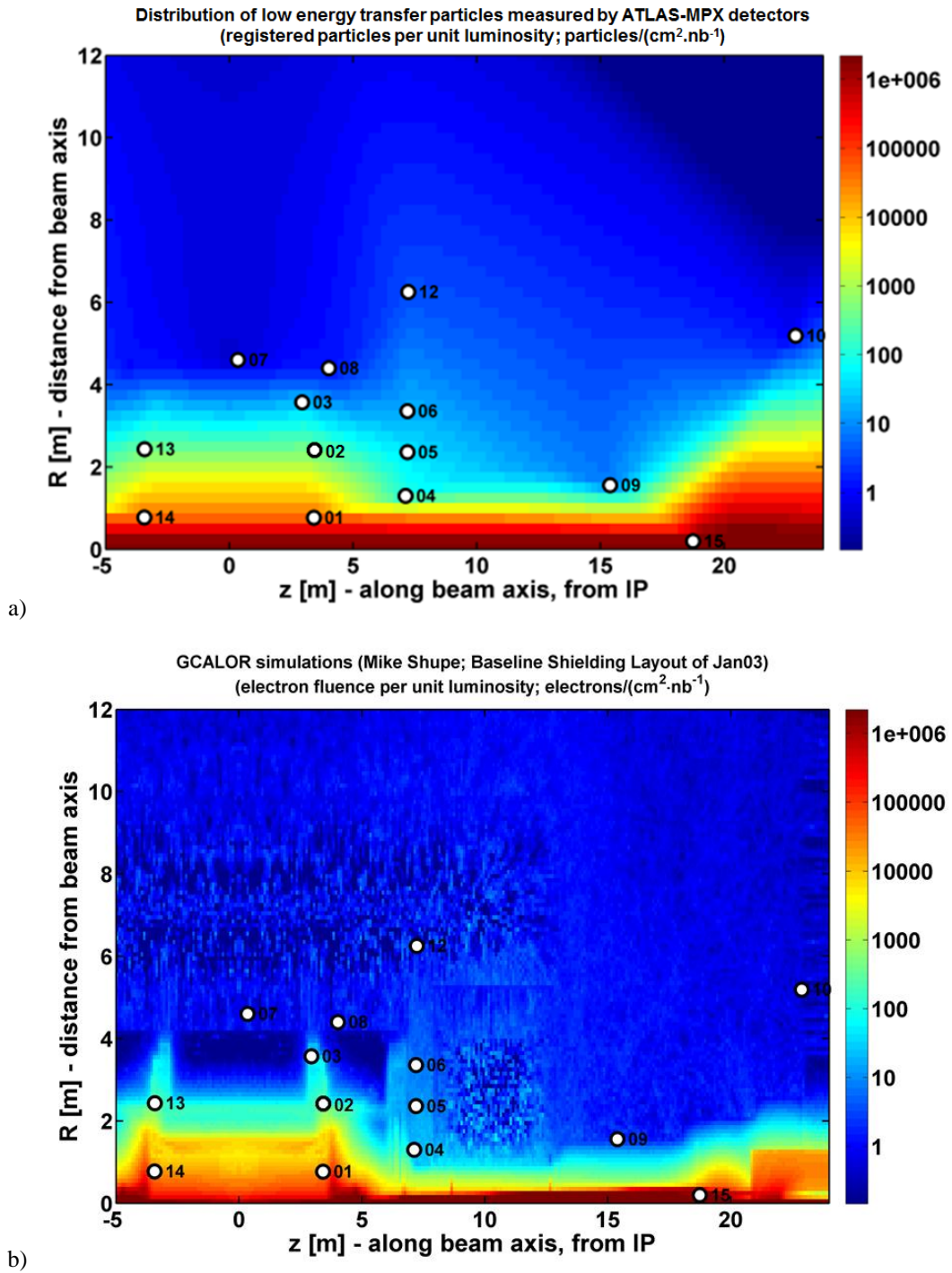
Figure 79. a) Spatial distribution of low energy transfer particles interpolated from data obtained from ATLAS-MPX network measurements in 2010. b) Calculated spatial distribution of electrons. The detector MPX11 is not shown on the figure as its coordinates (Z = 4.86 m, R = 16.69 m) do not match the y-scale used for the display of the simulated distribution of electrons.

Detector	ATLAS-MPX average LETP background cluster rate per second [cm^{-2}.s^{-1}]	ATLAS-MPX average LETP cluster rate per luminosity unit [cm^{-2}/nb^{-1}]	GCALOR electron current per luminosity unit [cm^{-2}/nb^{-1}]	GCALOR photon current per luminosity unit [cm^{-2}/nb^{-1}]	GCALOR ratio photons/ electrons	Ratio*
MPX01	(1.77 ± 0.01) E-02	(5.98 ± 0.69) E+04	(1.93 ± 0.01) E+04	(4.48 ± 0.01) E+05	23	0.40 ± 0.05
MPX02	(2.31 ± 0.01) E-02	(2.24 ± 0.19) E+02	(6.82 ± 0.27) E+01	(6.22 ± 0.02) E+03	91	0.58 ± 0.05
MPX03	(1.57 ± 0.01) E-02	(3.08 ± 0.14) E+01	(1.64 ± 0.11) E+01	(9.22 ± 0.08) E+02	56	0.83 ± 0.05
MPX04	(1.98 ± 0.01) E-02	(1.17 ± 0.05) E+02	(6.24 ± 0.36) E+01	(6.52 ± 0.04) E+03	104	1.09 ± 0.06
MPX05	(8.80 ± 0.01) E-03	(4.77 ± 0.21) E+01	(1.58 ± 0.13) E+01	(1.37 ± 0.01) E+03	87	0.62 ± 0.04
MPX06	(1.08 ± 0.01) E-02	(1.99 ± 0.10) E+01	(6.74 ± 0.73) E+00	(7.45 ± 0.07) E+02	111	0.71 ± 0.05
MPX07	(9.22 ± 0.01) E-03	(4.44 ± 0.22) E-01	(8.35 ± 0.98) E-01	(5.92 ± 0.08) E+01	71	3.21 ± 0.27
MPX08	(5.61 ± 0.01) E-03	(1.19 ± 0.06) E+00	(5.69 ± 0.83) E-01	(4.37 ± 0.07) E+01	77	0.85 ± 0.08
MPX09	(1.42 ± 0.01) E-02	(5.86 ± 0.32) E+00	(1.42 ± 0.22) E+00	(1.56 ± 0.02) E+02	110	0.51 ± 0.05
MPX10	(2.87 ± 0.01) E-02	(1.05 ± 0.06) E+00	(3.38 ± 0.59) E-01	(4.28 ± 0.06) E+01	127	0.73 ± 0.07
MPX11	(2.77 ± 0.01) E-02	(3.02 ± 0.14) E-01	(3.33 ± 0.32) E-01	(5.04 ± 0.04) E+01	151	2.77 ± 0.17
MPX12	(1.25 ± 0.01) E-02	(4.00 ± 0.19) E+00	(4.67 ± 0.63) E-01	(2.03 ± 0.01) E+02	434	0.62 ± 0.03
MPX13	(2.09 ± 0.01) E-02	(3.75 ± 0.22) E+02	(6.82 ± 0.27) E+01	(6.22 ± 0.02) E+03	91	0.35 ± 0.02
MPX14	(1.53 ± 0.01) E-02	(5.61 ± 0.65) E+04	(1.93 ± 0.01) E+04	(4.48 ± 0.01) E+05	23	0.42 ± 0.05
MPX15	(1.74 ± 0.01) E-02	(2.59 ± 0.33) E+06	(2.49 ± 0.01) E+06	(4.47 ± 0.01) E+07	18	1.13 ± 0.14
MPX16	(1.80 ± 0.01) E-02	(1.28 ± 0.94) E-03	-	-	-	-

* Ratio of the column (4 + 5 × 1%) and 3 – („GCALOR electron current per luminosity unit" + "GCALOR photon current per luminosity unit " / 100) / "ATLAS-MPX average LETP cluster rate per luminosity unit"

Table 7. Average LETP cluster rate during background (no collisions period) and the average LETP cluster rate per luminosity unit during collisions as measured by ATLAS-MPX detectors. The background LETP cluster rates are related to measurements done during 2010 (before the strong activation caused by high luminosity runs in 2011). On the other hand, the LETP cluster rate during collisions was determined from runs in 2011 (except for detectors MPX01, MPX14 and MPX15 operating in high threshold in 2011). For comparison, GCALOR calculated electron and photon currents are stated as well. Measured collision cluster rate for ATLAS-MPX data is the mean of individual cluster rate values obtained separately for each fill. Measurement uncertainty is the dispersion of the individual values of cluster rate around the mean and it does not represent the measurement statistics.

7.3 High energy transfer particles

The spatial distribution of high energy transfer particles (HETP) cluster rate per luminosity unit as measured with the ATLAS-MPX detectors is shown in Fig. 80a as a function of the distance R from the beam axis and the coordinate Z along the beam axis, from the interaction point (IP1). The lowest cluster rate is recorded with the detector MPX11 which is located on the UX15 cavern wall (see Tab. 2). The highest cluster rate is recorded with MPX15 (closest to the beam axis, along LUCID). Fig. 80b shows the distribution of protons calculated with GCALOR simulations. The summary of ATLAS-MPX measurements compared to GCALOR simulations is presented in Tab. 8.

a)

b)
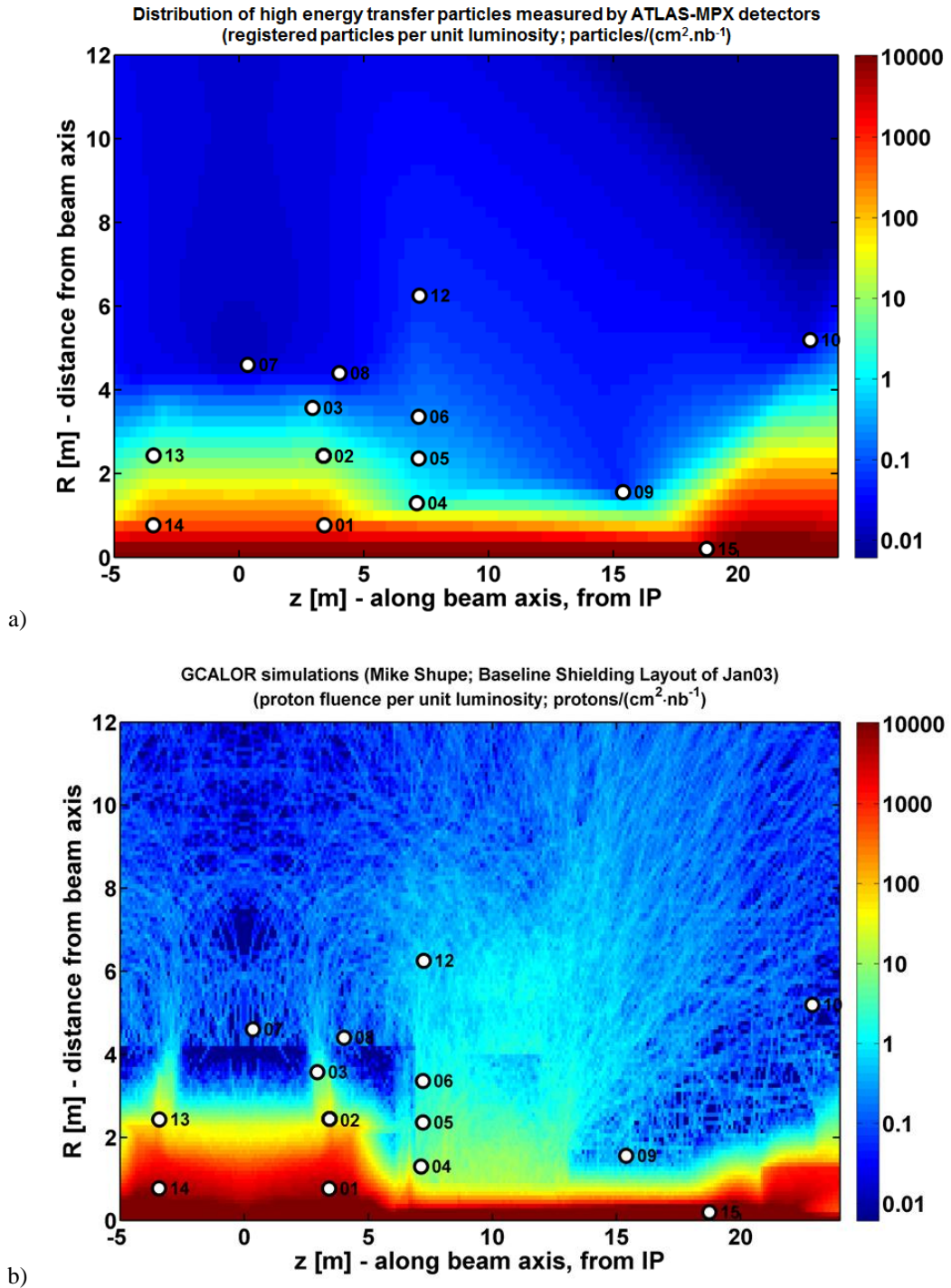
Figure 80. a) Spatial distribution of high energy transfer particles (HETP) interpolated from data obtained from ATLAS-MPX network measurements in 2010. b) Calculated spatial distribution of protons. The detector MPX11 is not shown on the figure as its coordinates (Z = 4.86 m, R = 16.69 m) do not match the y-scale used for the display of the simulated distribution of protons.

Detector	ATLAS-MPX average HETP background cluster rate per second [cm^{-2}.s^{-1}]	ATLAS-MPX average HETP cluster rate per luminosity unit [cm^{-2}/nb^{-1}]	GCALOR proton current per luminosity unit [cm^{-2}/nb^{-1}]	Ratio*
MPX01	(3.10 ± 0.05) E-04	(6.68 ± 1.04) E+02	(4.43 ± 0.04) E+03	6.63 ± 1.03
MPX02	(1.13 ± 0.03) E-03	(3.19 ± 0.29) E+00	(1.26 ± 0.12) E+01	3.97 ± 0.51
MPX03	(2.69 ± 0.03) E-04	(4.84 ± 0.25) E-01	(1.11 ± 0.29) E+00	2.28 ± 0.60
MPX04	(1.21 ± 0.01) E-03	(1.75 ± 0.07) E+00	(8.23 ± 1.28) E+00	4.70 ± 0.76
MPX05	(3.18 ± 0.04) E-04	(5.03 ± 0.26) E-01	(5.99 ± 2.45) E-01	1.19 ± 0.49
MPX06	(2.97 ± 0.04) E-04	(2.11 ± 0.14) E-01	(3.92 ± 1.75) E-01	1.86 ± 0.84
MPX07	(2.72 ± 0.03) E-04	(4.14 ± 0.53) E-03	(9.16 ± 3.24) E-02	22.10 ± 8.31
MPX08	(2.50 ± 0.03) E-04	(1.15 ± 0.10) E-02	(1.21 ± 1.21) E-02	1.06 ± 1.06
MPX09	(1.41 ± 0.02) E-04	(8.64 ± 0.63) E-02	(4.16 ± 1.20) E-01	4.82 ± 1.44
MPX10	(3.87 ± 0.04) E-04	(1.14 ± 0.09) E-02	(5.12 ± 2.29) E-02	4.51 ± 2.04
MPX11	(4.23 ± 0.04) E-04	(6.31 ± 0.63) E-03	(1.26 ± 0.63) E-02	1.99 ± 1.02
MPX12	(2.76 ± 0.03) E-04	(5.32 ± 0.33) E-02	(4.42 ± 0.61) E-01	8.32 ± 1.25
MPX13	(2.94 ± 0.04) E-04	(5.27 ± 0.34) E+00	(1.26 ± 0.12) E+01	2.40 ± 0.27
MPX14	(3.13 ± 0.06) E-04	(6.17 ± 0.81) E+02	(4.43 ± 0.04) E+03	7.18 ± 0.94
MPX15	(3.34 ± 0.07) E-04	(1.20 ± 0.26) E+04	(5.17 ± 0.16) E+04	4.32 ± 0.94
MPX16	(3.78 ± 0.04) E-04	(2.11 ± 1.38) E-04	-	-

*Ratio of the column 4 and 3 - „GCALOR proton current per luminosity unit" / "ATLAS-MPX average HETP cluster rate per luminosity unit"

Table 8. Average HETP cluster rate during background (no collisions period) and the average HETP cluster rate per luminosity unit during collisions as measured by ATLAS-MPX detectors. The background HETP cluster rates are related all measurements. The HETP cluster rate during collisions was determined from runs in 2011 (except for detectors MPX01, MPX14 and MPX15 operating in high threshold in 2011). For comparison, GCALOR calculated proton current is stated as well. Measured collision cluster rate for ATLAS-MPX data is the mean of individual cluster rate values obtained separately for each fill. Measurement uncertainty is the dispersion of the individual values of cluster rate around the mean and it does not represent the measurement statistics.

Only a rough comparison with simulated data can be done because the HETP particles measured with ATLAS-MPX detectors include signal from protons and heavy charged particles coming from outside the ATLAS-MPX detector, signal from protons created by neutron recoils in polyethylene convertor above the sensor and entering the sensor and signal from atomic nuclei recoiled by neutron interactions inside the sensor. These three components cannot be distinguished without additional Monte Carlo calculations. As seen from Tab. 8, there is a significant difference between simulated proton current and HETP measurement which has to be further studied with detailed Monte Carlo simulations.

7.4 Minimum ionizing particles

The spatial distribution of MIP cluster rate per luminosity unit as measured with the ATLAS-MPX detectors is shown in Fig. 81a as a function of the distance R from the beam axis and the coordinate Z along the beam axis, from the interaction point (IP1). The lowest MIP cluster rate is recorded with the detector MPX11 which is located on the cavern wall USA HS (level 4 – side A, see Tab. 2). The highest number of MIP cluster rate is recorded with MPX15 (closest to the beam axis, along LUCID).

The detectors MPX15, MPX14 and MPX01 are recording a much higher MIP cluster rate than other ATLAS-MPX devices (see the summary in Tab. 9). The number of recognized MIP tracks depends on the ATLAS-MPX detector orientation and position with respect to the beam axis. Being closer to the beam axis, MPX01, MPX14 and MPX15 are sensitive to MIPs produced from the interaction point. Fig. 81b shows the distribution of muons calculated with GCALOR simulations for comparison.

Detector	ATLAS-MPX average MIP background cluster rate per second [$cm^{-2}.s^{-1}$]	ATLAS-MPX average MIP cluster rate per luminosity unit [cm^{-2}/nb^{-1}]	GCALOR muon current per luminosity unit [cm^{-2}/nb^{-1}]	Ratio*
MPX01	(5.94 ± 0.18) E-05	(1.21 ± 0.28) E+03	(2.46 ± 0.03) E+03	2.03 ± 0.47
MPX02	(9.27 ± 0.22) E-05	(9.42 ± 0.85) E+00	(5.15 ± 0.74) E+00	0.55 ± 0.09
MPX03	(4.09 ± 0.12) E-05	(8.88 ± 0.40) E-01	(2.95 ± 1.47) E-01	0.33 ± 0.17
MPX04	(3.98 ± 0.12) E-05	(1.61 ± 0.13) E+00	(1.12 ± 0.15) E+01	6.97 ± 1.09
MPX05	(4.24 ± 0.12) E-05	(4.79 ± 0.26) E-01	(1.90 ± 0.43) E+00	3.96 ± 0.93
MPX06	(4.21 ± 0.12) E-05	(2.16 ± 0.17) E-01	(8.62 ± 2.60) E-01	3.99 ± 1.24
MPX07	(1.33 ± 0.06) E-05	(9.39 ± 0.81) E-03	(2.40 ± 0.52) E-01	25.59 ± 6.00
MPX08	(4.73 ± 0.12) E-05	(1.42 ± 0.14) E-02	(3.39 ± 0.64) E-01	23.89 ± 5.08
MPX09	(6.78 ± 1.52) E-07	(2.45 ± 0.17) E-01	(1.74 ± 0.78) E-01	0.71 ± 0.32
MPX10	(3.16 ± 0.10) E-05	(8.35 ± 0.76) E-03	(8.20 ± 2.90) E-02	9.81 ± 3.59
MPX11	(5.39 ± 0.13) E-05	(2.39 ± 0.29) E-03	(9.44 ± 5.45) E-03	3.94 ± 2.32
MPX12	(5.71 ± 0.13) E-05	(5.55 ± 0.51) E-02	(1.17 ± 0.31) E-01	2.10 ± 0.59
MPX13	(3.61 ± 0.12) E-05	(1.46 ± 0.09) E+01	(5.15 ± 0.74) E+00	0.35 ± 0.06
MPX14	(3.98 ± 0.19) E-05	(1.03 ± 0.16) E+03	(2.46 ± 0.03) E+03	2.39 ± 0.36
MPX15	(6.79 ± 0.27) E-05	(1.57 ± 0.34) E+04	(6.18 ± 0.53) E+03	0.39 ± 0.09
MPX16	(1.74 ± 0.07) E-05	(7.69 ± 4.63) E-05	-	-

*Ratio of the column 4 and 3 - „GCALOR muon current per luminosity unit" / "ATLAS-MPX average MIP cluster rate per luminosity unit"

Table 9. Average MIP cluster rate during background (no collisions period) and the average MIP cluster rate per luminosity unit during collisions as measured by ATLAS-MPX detectors. The average background MIP cluster rates are calculated from all measurements. The MIP cluster rate during collisions was determined from runs in 2011 (except for detectors MPX01, MPX14 and MPX15 operating in high threshold in 2011). Measured collision cluster rate is the mean of individual cluster rate values obtained separately for each fill. Measurement uncertainty is the dispersion of the individual values of cluster rate around the mean and it does not represent the measurement statistics.

a)

b)
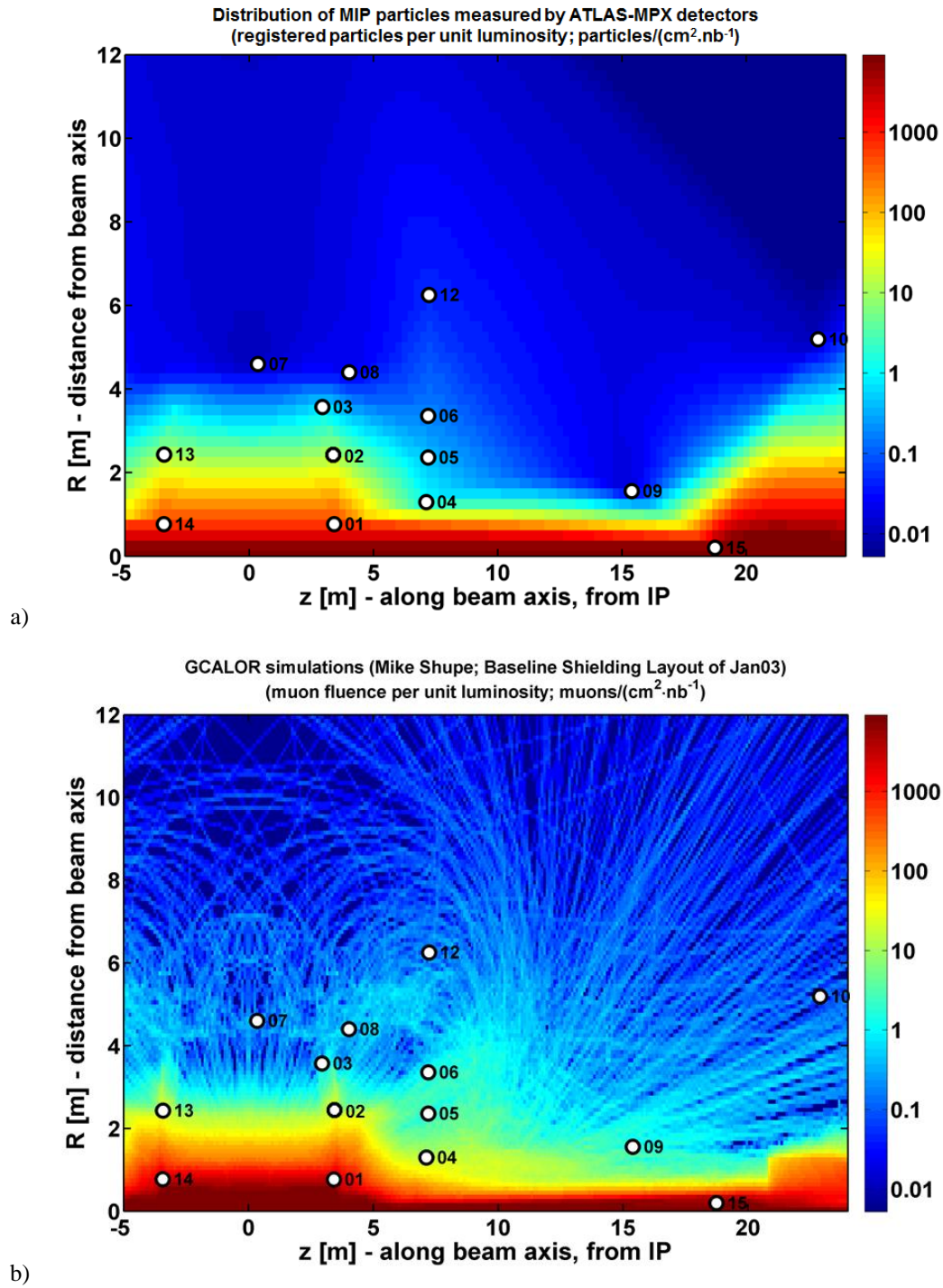
Figure 81. a) Spatial distribution of MIPs interpolated from data obtained from ATLAS-MPX measurements in 2010. b) Calculated spatial distribution of muons. The detector MPX11 is not shown on the figure as its coordinates (Z = 4.86 m, R = 16.69 m) do not match the y-scale used for the display of the simulated distribution of protons.

Similarly to HETP particles, only a rough comparison of measured MIPs with simulated data can be done because the MIPs measured with ATLAS-MPX detectors

include signal from all ionizing particles which create a thin straight track in the detector with a 20 pixel length (see section 3.4.1). The "thin track" means that the deposited energy is at maximum several tens of keV per pixel, i.e., high energy protons will be registered as MIPs as well.

As seen from Tab. 9, there is a significant difference between simulated muon current and MIPs measurement. The reason is that the most of the ATLAS-MPX devices are oriented perpendicularly to the beam direction causing the assignment of the MIP signal in the different category (dot or small blob). It has to be further studied with detailed Monte Carlo simulations.

7.5 Thermal neutron flux

Neutrons produced by the interactions of particles yielded by the collisions of protons with surrounding materials, cover a large range of energies. These fast neutrons are slowed down by means of interaction in light materials (copper, hydrogen, carbon and other light elements) present within the ATLAS detector volume. Thermalization of fast neutrons increases the thermal neutron flux by an amount which depends on the quantity of material in the environment of a given ATLAS-MPX unit.

Thermal neutrons are detected effectively via charged ions produced in silicon from the nuclear reaction:

$$n + {}^6Li \rightarrow \alpha \ (2.05 \ MeV) + {}^3H \ (2.73 \ MeV); \quad \sigma \ (25 \ meV) = 940 \ b$$
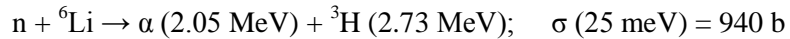
in the ATLAS-MPX detector area covered with a ${}^6LiF$ layer (see the region maps in Fig. 31). The lowest thermal neutron flux is recorded with the detector MPX11 which is located far from the beam axis and surrounded with less light material. The detectors MPX01, MPX14 and MPX15, close to the beam axis and surrounded by large amount of light materials, are recording a much higher thermal neutron interactions.

7.5.1 Correction of ${}^6Li$ measured signal to contribution of epithermal neutrons

As mentioned before, ATLAS-MPX detectors register thermal neutrons using nuclear interaction with ${}^6Li$. The nucleus disintegrates into two heavy charged particles (triton and alpha particle) which can subsequently enter the sensor chip and cause signal. Although the interaction cross section is very high for thermal neutrons, it is not zero for higher neutron energies and hence the measured signal can be caused by epithermal and fast neutrons as well (see Fig. 8 for ${}^6Li(n,\alpha)$ interaction cross section). This can cause overestimate of thermal neutron flux especially in untypical neutron fields where the thermal component is missing or it significantly differs from the thermal neutron calibration field used for ATLAS-MPX detectors calibration (see subsection 5.3). Such special case occurs inside the neutron shielding in the position where MPX15 is located (see Fig. 35 and Tab. 2) as can be seen from GCALOR simulated neutron spectra depicted in Fig. 82.
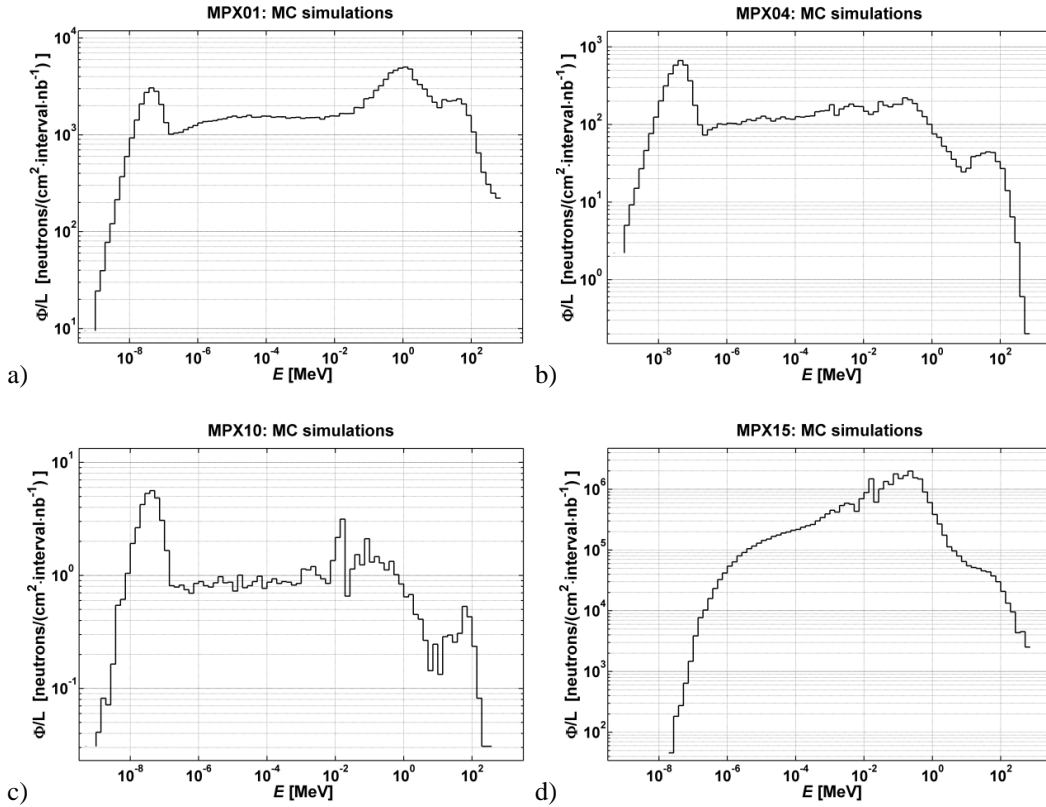
Figure 82. a) Spectral fluence distribution of neutrons at locations of MPX01, b) MPX04, c) MPX10 and d) MPX15 obtained from GCALOR simulations. It can be seen that with increasing distance from the interaction point (MPX01 – MPX04 – MPX10) the thermal neutron component of the spectra is increasing relatively to the fast neutron component. Neutron spectrum at MPX15 position absolutely lacks thermal neutron component.

Correction of the measured thermal neutron fluxes to the signal caused by non-thermal neutrons was performed using resonance integrals. This correction is described in the Appendix B in more detail. The correction is at level of 3 - 7% for all ATLAS-MPX detectors except for MPX15 where the correction reaches 82%.

7.5.2 Spatial distribution of thermal neutrons

Spatial distribution of thermal neutron fluence per luminosity unit as measured with the ATLAS-MPX detectors is shown in Fig. 83 as a function of the distance R from the beam axis and the coordinate Z along the beam axis, from the interaction point (IP) together with the distribution calculated by GCALOR simulations. The results of thermal neutron flux measurements are summarized in Tab. 10.

a)

b)
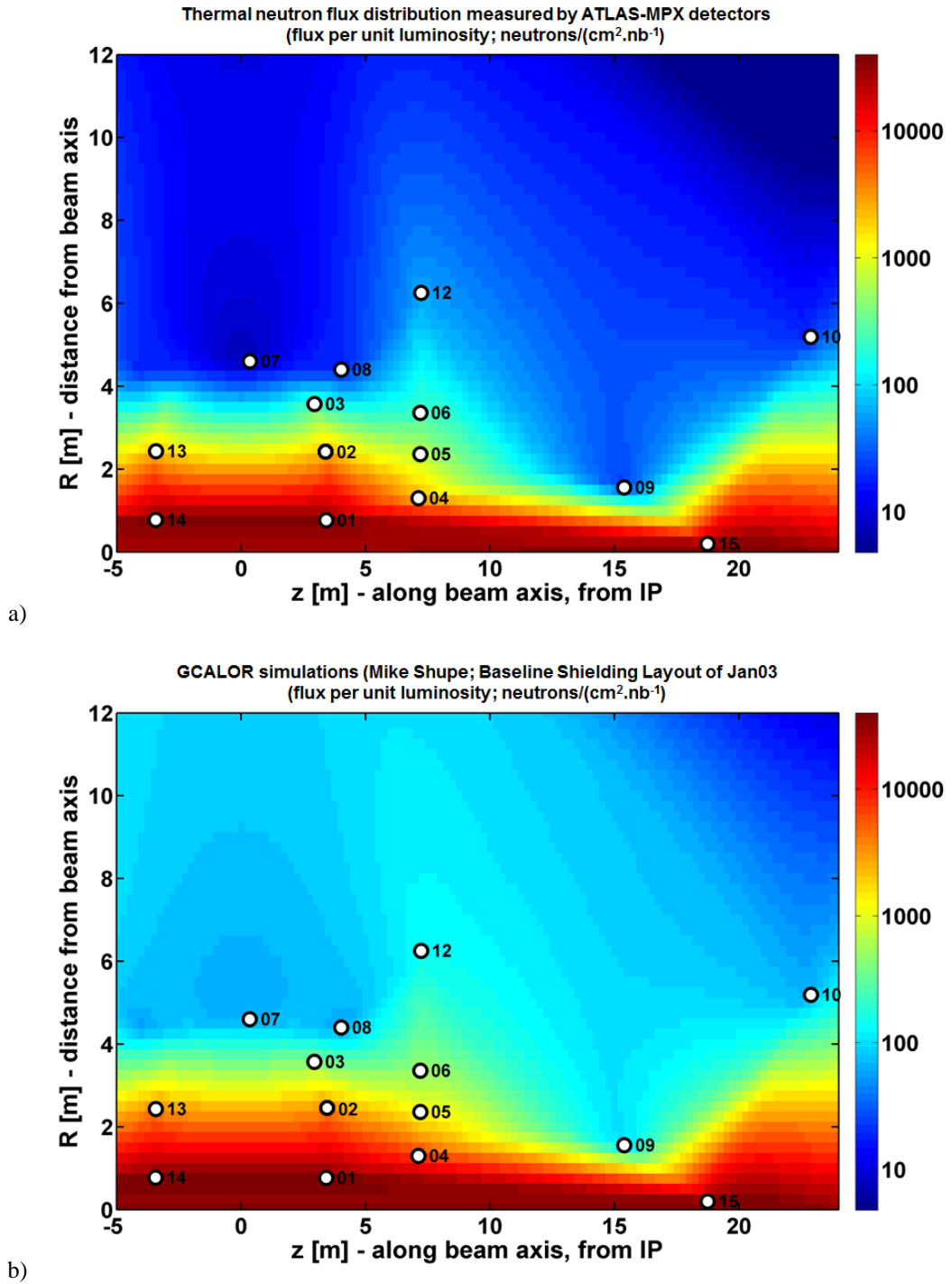
Figure 83. a) Spatial distribution of thermal neutron flux normalized per luminosity unit interpolated from data obtained from ATLAS-MPX network measurements in 2010. b) Spatial distribution of thermal neutron fluence per luminosity unit as calculated by GCALOR simulations. The detector MPX11 is not shown on the figure as its coordinates (Z = 4.86 m, R = 16.69 m) do not match the y-scale used for the display of the simulated distribution of thermal neutrons.

Detector	ATLAS-MPX average thermal neutron background flux [cm^{-2}.s^{-1}]	ATLAS-MPX average thermal neutron fluence per luminosity unit [cm^{-2}/nb^{-1}]	GCALOR thermal neutron fluence per luminosity unit [cm^{-2}/nb^{-1}]	Ratio*
MPX01	(1.38 ± 2.65) E-02	(4.59 ± 0.86) E+04	(3.86 ± 0.02) E+4	0.84 ± 0.16
MPX02	(-1.74 ± 3.68) E-03	(1.62 ± 0.17) E+03	(3.84 ± 0.03) E+3	2.36 ± 0.25
MPX03	(-3.41 ± 2.85) E-03	(2.73 ± 0.18) E+02	(4.59 ± 0.09) E+2	1.68 ± 0.11
MPX04	(-3.74 ± 0.21) E-01	(3.20 ± 0.18) E+03	(7.55 ± 0.06) E+3	2.36 ± 0.14
MPX05	(2.47 ± 1.95) E-03	(7.36 ± 0.39) E+02	(1.03 ± 0.02) E+3	1.40 ± 0.08
MPX06	(-6.10 ± 21.57) E-04	(2.09 ± 0.12) E+02	(5.21 ± 0.10) E+2	2.50 ± 0.15
MPX07	(2.23 ± 1.52) E-03	(6.58 ± 0.59) E+00	(6.30 ± 0.14) E+1	9.50 ± 0.86
MPX08	(-1.41 ± 1.17) E-03	(1.61 ± 0.09) E+01	(5.60 ± 0.13) E+1	3.47 ± 0.22
MPX09	(-2.45 ± 1.37) E-03	(2.84 ± 0.26) E+01	(1.00 ± 0.03) E+2	3.54 ± 0.33
MPX10	(-4.58 ± 18.23) E-04	(1.99 ± 0.13) E+01	(6.60 ± 0.13) E+1	3.31 ± 0.22
MPX11	(-1.78 ± 2.25) E-03	(2.86 ± 0.43) E+00	(9.60 ± 0.09) E+1	33.50 ± 5.01
MPX12	(-2.22 ± 1.35) E-03	(6.12 ± 0.32) E+01	(1.40 ± 0.02) E+2	2.29 ± 0.12
MPX13	(5.88 ± 4.43) E-03	(2.69 ± 0.24) E+03	(3.84 ± 0.03) E+3	1.42 ± 0.13
MPX14	(1.19 ± 1.19) E-02	(3.82 ± 1.21) E+04	(3.86 ± 0.02) E+4	1.01 ± 0.32
MPX15	(6.76 ± 2.40) E-02	(3.81 ± 1.19) E+04	(3.34 ± 0.67) E+4	0.88 ± 0.28
MPX16	(9.62 ± 17.77) E-04	(4.64 ± 4.72) E-02	-	-

*Ratio of the column 4 and 3 - „GCALOR thermal neutron fluence per luminosity unit" / "ATLAS-MPX average thermal neutron fluence per luminosity unit"

Table 10. Average thermal neutron flux during background and average thermal neutron fluence per luminosity unit during collisions as measured by ATLAS-MPX detectors and comparison with GCALOR simulations. The background thermal neutron fluxes are related all measurements. The thermal neutron fluence during collisions was determined from runs in 2011 (except for detectors MPX01, MPX14 and MPX15 operating in high threshold in 2011). Measured collision cluster rate is the mean of individual cluster rate values obtained separately for each fill. Measurement uncertainty is the dispersion of the individual values of cluster rate around the mean and it does not represent the measurement statistics.

It can be seen that the background neutron flux of nearly all detectors is not statistically distinguishable from zero. The only exception is the detector MPX04 accidentally contaminated at one single point of the sensor chip by an alpha-emitter with long half-life. Hence the increased background of this detector is not related to the outer influence.

The comparison with Monte Carlo simulations shows a fair agreement within a factor of two. Significant deviations are observed in the low intensity region of the caverns (MPX07 and MPX11) where the measured thermal neutron flux is found to be lower than simulated. The added neutron shielding may explain this reduction.

8. ATLAS-MPX network upgrade

The successful operation of the ATLAS-MPX network and new technologies available leads to the proposal of the network upgrade planned for the LHC upgrade shutdown in 2013 and 2014. Reconciliation of simulated proton and muon currents with HETP and MIPs measurement, respectively, requires further studies with detailed Monte Carlo simulations and removal of ambiguity between energetic protons and neutron signals, better determination of the direction of entering MIPs on a sensor area and, as mentioned above, discrimination of orthogonally incident MIPs from low energy electrons and photons. This can be possibly achieved by adding Timepix detectors [37] to the network of ATLAS-MPX detectors. The Timepix detector with its time over threshold (TOT) capability is analogous to a Wilkinson type ADC and allows direct energy measurement in each pixel. It will possibly provide measurement of absolute fluxes of fast neutrons and allow distinguishing directionality (backward from forward) of neutron motion at their position. This upgraded network will contribute further to estimates of SEE effects affecting the ATLAS and LHC machine electronic devices. The Timepix detectors positioned close to Tile and Liquid Argon calorimeters could provide measurement of the missing transverse energy and study of hadron leakage into the muon detector system. In addition, an increase of the data readout speed by factor of 50 is foreseen [19], thus reducing the measurements dead time significantly. This improved readout system will use a single-wire communication, simplifying the present cable structure. The main aim of the upgrade can be summarized to following highlights:

- Usage of Timepix detectors
- Multilayer detector structure
- New positions of the devices according to the specific measurement needs
- Faster readout interface (decrease the readout time by factor 50)
- Single-wire data readout
- Revision of data processing and visualization

8.1 Timepix pixel detector

Timepix pixel ASIC has been developed on basis of the successful Medipix2 MXR chip introducing the possibility of measurement of the time of arrival (TOA), time over

threshold (TOT) or event counting independently in each pixel. The chip has the same dimensions, floor plan and readout architecture as its predecessor Medipix2 (see subsection 3.1.1) allowing almost full backward compatibility with all existing readout interfaces as described in subsection 3.2. The main differences are in the pixel cell architecture.

8.1.1 Timepix pixel cell architecture

The Timepix cell covers the same area of 55×55 μm^2 like Medipix2 chip and consists of ~550 transistors. It can be divided as well into an analog and a digital part as shown in Fig. 84. Both parts operate at 2.2 V independent power supplies. The static analog power consumption is about 6.5 µW per pixel and the digital part consumes ~7 µW in data acquisition state running at 80 MHz.
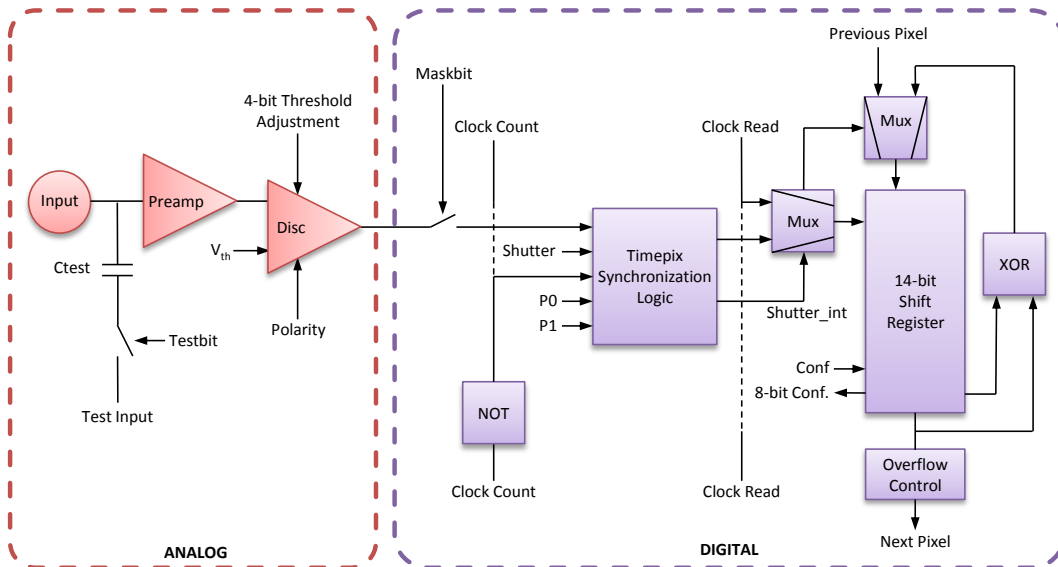
Figure 84. Timepix pixel cell block diagram. In red is the analog part of the pixel and in violet the digital side.

In comparison to the Medipix2 chip (see Fig. 16) there are three main differences in the Timepix architecture:
- Single analog discriminator with the 4-bit threshold adjustment.
- Each pixel can be configured independently into three different operation modes (TOT, TOA, event counting) with the configuration bits P0 and P1.
- There is a clock signal (*Clock Count*) distributed to the entire pixel matrix for the purposes of TOT and TOA measurements. The maximum frequency of this clock signal is roughly 100 MHz.

Similarly to the Medipix2, the Timepix pixel cell has two different working modes depending on the CMOS input *Shutter* state.

Data acquisition mode

With the *Shutter* signal low the pixel works in the data acquisition mode. In this case the 14-bit shift register serves as a pseudo-random counter with dynamic range of 11810 counts. Analog signal from the preamplifier is compared with the pre-set threshold level and the output of the comparator is connected to the Timepix Synchronization Logic unit which generates the clock signals for the counter in one of the three operating modes controlled by bits P0 and P1:

- **Event counting mode (P0 = 0 and P1 = 0):** Each interaction above the analog threshold level increment the counter value by 1. This mode is also called "Medipix2 mode".

- **Time over Threshold (TOT) mode (P0 = 1 and P1 = 0):** In this mode the counter is incremented, with the speed of *Clock Count* input signal, during whole time when the analog pulse is above the threshold level. Since the width of the analog output of the preamplifier grows linearly with the input charge the counter value is proportional to energy deposited in the pixel.

- **Time of Arrival (TOA) mode (P0 = 1 and P1 = 1):** In this mode the counter is incremented, with the speed of *Clock Count* input signal, from the first moment of the discriminator activation until the global *Shutter* signal goes high. By comparing the content of the counter of two different pixels one can measure directly the time difference between those two interactions. The dynamic range of this measurement is limited by the counter depth. With commonly used 10 MHz clock the maximum time interval measured in each pixel is 1.18 ms.

Readout/settings mode

When the *Shutter* signal is high the pixel readout/setting mode can be initialized. In this mode the 14-bit shift register of each pixel is connected to the next and previous to form a 3584-bit shift register in the same way like in Medipix2 as shown in Fig. 15.

8.1.2 Timepix enhanced pattern recognition capability

New information obtained with Timepix chip in either TOT or TOA modes can be effectively used to increase the sensitivity of the characteristic pattern recognition algorithm [22]. The example showing the difference between TOT and TOA response of the Timepix detector operating in low threshold (10 keV) to the ^{226}Ra source is presented in Fig. 85.

In the TOA mode (see Fig. 85a) the different colors of the tracks in the image correspond to the difference in the time of arrival of the individual interactions. In this mode overlapping tracks can be effectively recognized and separated during the pattern recognition procedure as depicted in the cut of the image. One can clearly distinguish that two of the three clusters are overlap of the three individual interactions.

With the maximum time resolution of 10 ns and acquisition time of 100 μs it is possible to distinguish reliably as much as 10^6 interactions.cm^{-2}.s^{-1}. The time resolution has to be reduced for longer acquisition times, so the counter depth of 11810 counts will be able to cover the full acquisition time window.
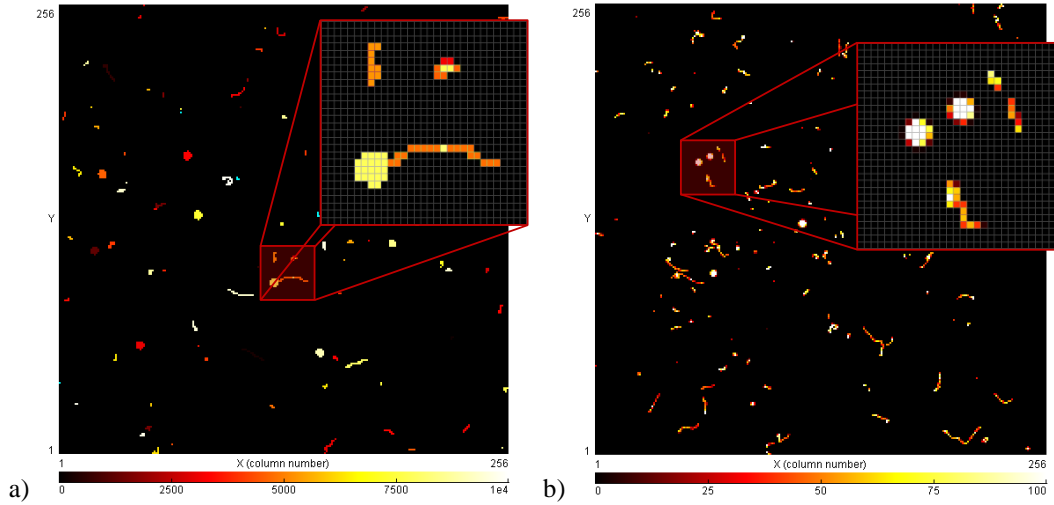
Figure 85. Response of the Timepix detector irradiated by [226]Ra source. a) Detector is operating in TOA mode (10 keV threshold, 10 MHz frequency). Different colors represent the time shift between individual interactions. Because the charge collection in silicon is far below the 100 ns time resolution used for this measurement the time information within the individual clusters is lost. b) Detector is operating in the TOT mode (10 keV threshold, 10 MHz frequency). Colors correspond to the deposited energy. Highly ionizing alpha particles can be seen as a round clusters with high central energy deposition.

In the TOT mode (see Fig. 85b) the different colors of the pixels within the clusters correspond to the local energy deposition. As shown in the cut of the image electrons, and particles with low energy transfer in general, show the per pixel energy deposition in the order of 50 TOT counts while the central pixels of the alpha particle clusters can have more than 1000 TOT counts.

In order to evaluate the potential of the TOT information for the radiation field measurements the differences in the response of the individual pixels has to be considered and the detector has to be calibrated to convert the TOT counts into the energy units. The calibration was done on the per pixel basis using the procedure described by Jan Jakubek in [29]. Four different radiation sources have been used in this experiment:

- [241]Am - 5.48 MeV alpha particles, 59.5 keV gamma and 17.8 keV X-ray photons
- [90]Sr - 196 keV and 934 keV electrons (average energy of the beta spectrum)
- [137]Cs - 662 keV photons
- [60]Co - 1.17 MeV and 1.33 MeV photons

The cluster spectra from abovementioned sources are shown in Fig. 86. There is a large amount of the clusters from the electron and gamma sources with the size between 5 and 40 (see Fig. 86a). These are, with ~1% probability for ATLAS-MPX criteria, miscategorized by the pattern recognition algorithm as a heavy blobs (see subsection 5.6). By using additional information about the cluster height (see Fig. 86b) and selecting only clusters with height > 500 into the heavy blob category it is possible to decrease the heavy blob miscategorization probability by more than 2 orders of magnitude. Further information can be obtained from the cluster volume e.g. overlapping of two or three alpha interactions (see Fig. 86c).

94
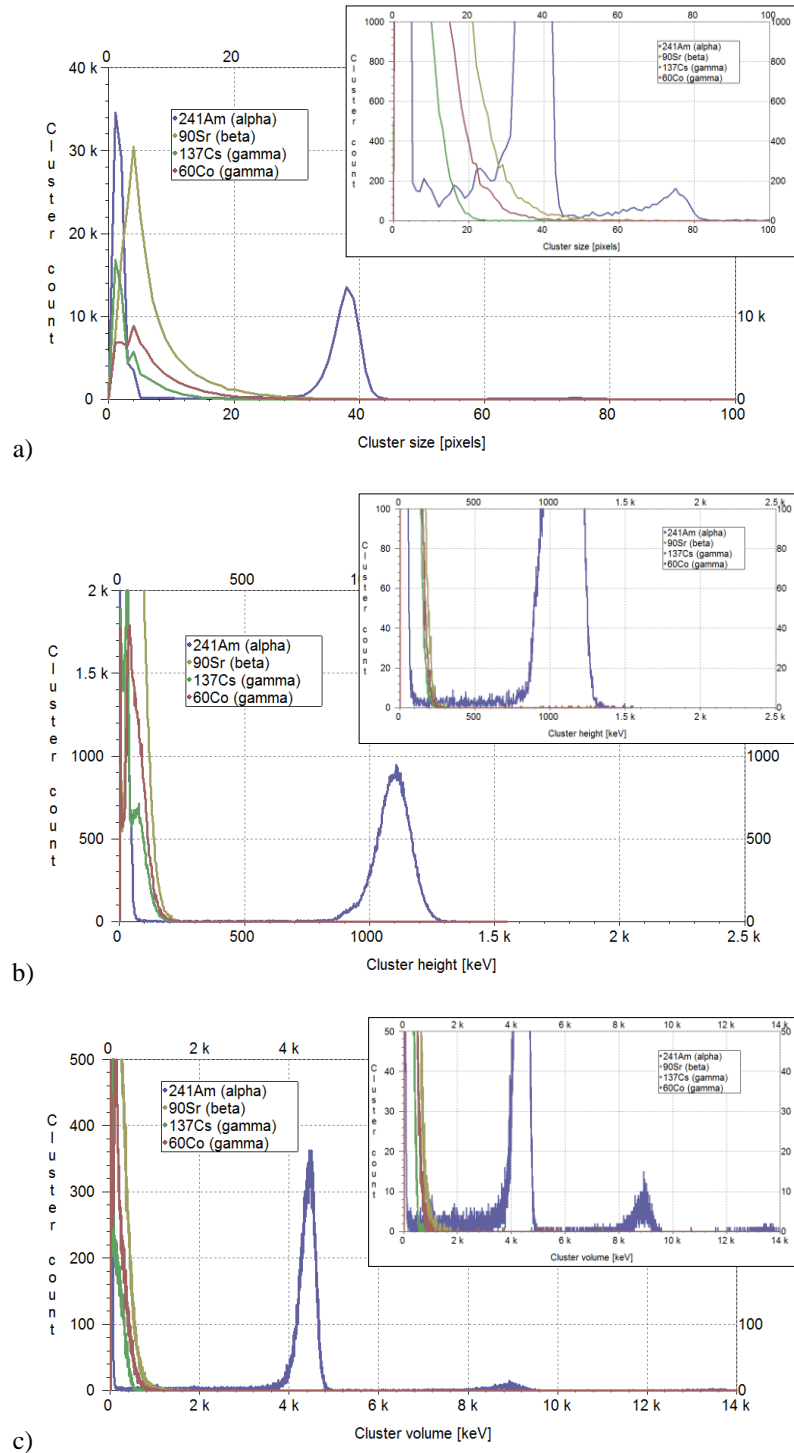
Figure 86. Example of the information extracted from the TOT mode of the Timepix device. a) The cluster-size spectrum of the number of pixels in each cluster provides the basic Medipix2-like information. b) The cluster height spectrum of the pixels with highest TOT count in the cluster show better separation of alpha particles and electrons. c) The cluster volume spectrum of the TOT sum of all pixels in the cluster can be used to detect e.g. the overlapping of the alpha clusters.

The TOT measurements provide additional information for the low energy transfer interactions as well (see Fig. 87).

a)

b)

c)
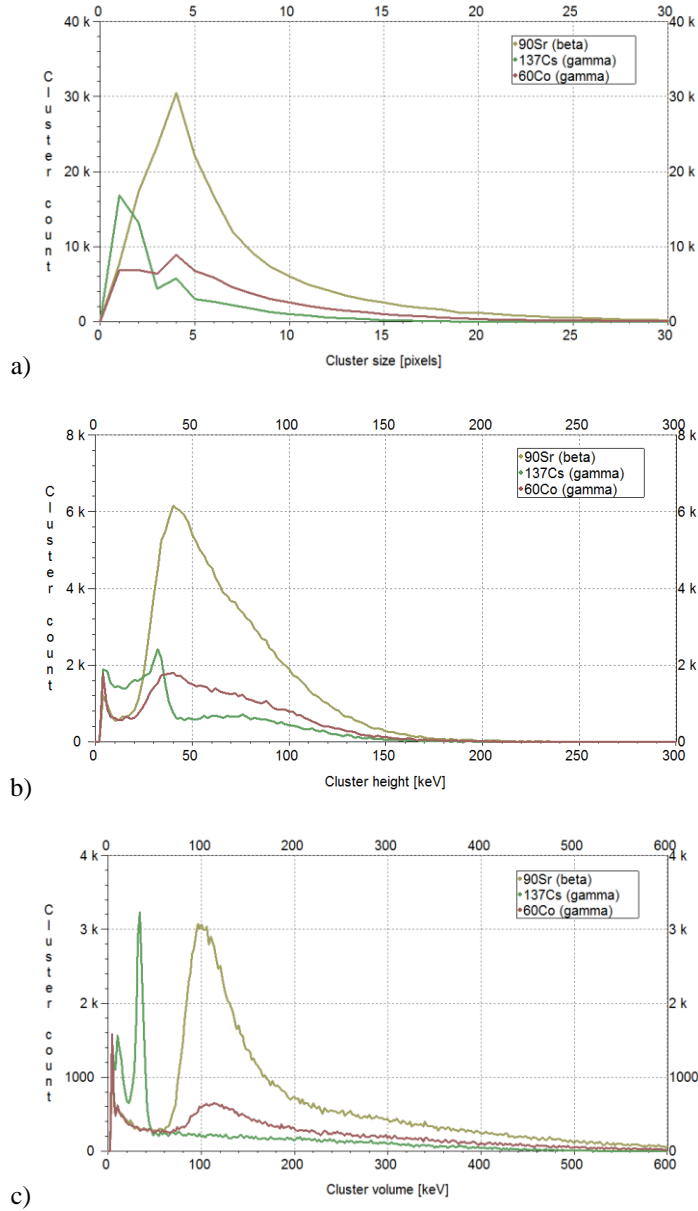
Figure 87. Timepix TOT measurement of the electron and photon interactions only. Cluster size spectrum a) and cluster heights spectrum b) show only very limited potential for the further recognition and separation of the electron and photon interactions. Cluster volume spectrum c) shows the total energy deposition in silicon as well as its distribution which is very useful for the dosimetry and radiation safety applications.

TOT mode allows direct energy deposition measurement for each interaction radiation quanta as well as the rough estimation of the energy spectrum of the LETP interactions (see Fig. 87c) which is important for example for the dosimetry and radiation safety applications.

8.2 Multilayer detector concept

Despite the enhanced capability of the Timepix readout chip in the radiation detection applications the directional sensitivity of the single planar pixel detector is limited to the specific interactions (e.g. MIP particles passing horizontally the sensor layer). In order to obtain more complete information on the direction of the interacting radiation the commonly used approach use a collimator and proper shielding material but this result in a significant reduction of the detection efficiency and sensitivity is limited half of the space.

Another possibility used especially in the high energy physics experiments is based on the arrangement of the several detector layers in a form of a telescope. The prototype of such multilayer device based on Timepix pixel detector has been already developed [38].

The device consists of a special PCB with the opening in the position of the Timepix chip to reduce the amount of the insensitive material in between individual layers (see Fig. 88).
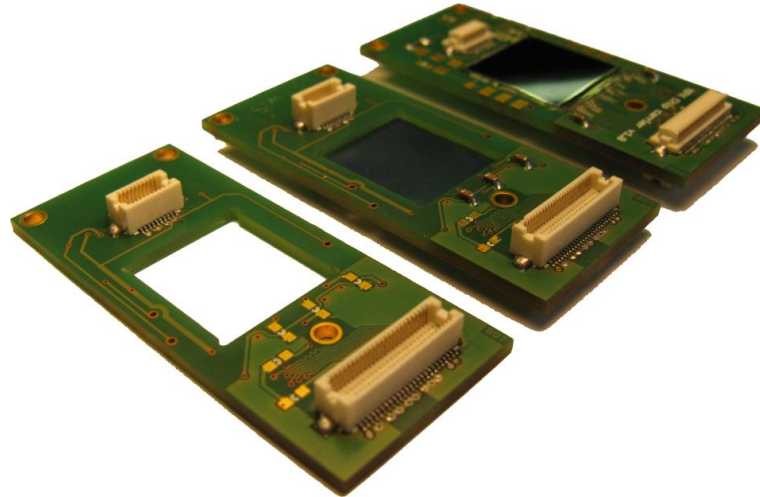
Figure 88. Photograph of the stack chipboard without detector chip (front), with the detector chip (center) and with the detector chip facing the 300 µm thick silicon sensor up (back). There is no PCB material below the chip active area to minimize the thickness of non-sensitive material in between the layers.

Such detector plains can be stacked together forming a multilayer pixel telescope. The individual Timepix readout chips are connected serially into the daisy-chain structure which allows using the same readout interfaces and software tools like with the single chip setup (see Fig. 89). With this implementation an arbitrary number of chips can be interconnected (four layers has been tested successfully).

The power dissipation of each detector layer is about 1 W. Absence of the PCB material below the chips limits the passive cooling capability of the setup which temperature can easily rise up to 80° C at room temperature conditions. Such a high operation temperature increases significantly the electronic noise of the chip and thus the minimum operating threshold level. Therefore a small fan is used to reduce the operating temperature of the setup to reasonable 40° C at room temperature.
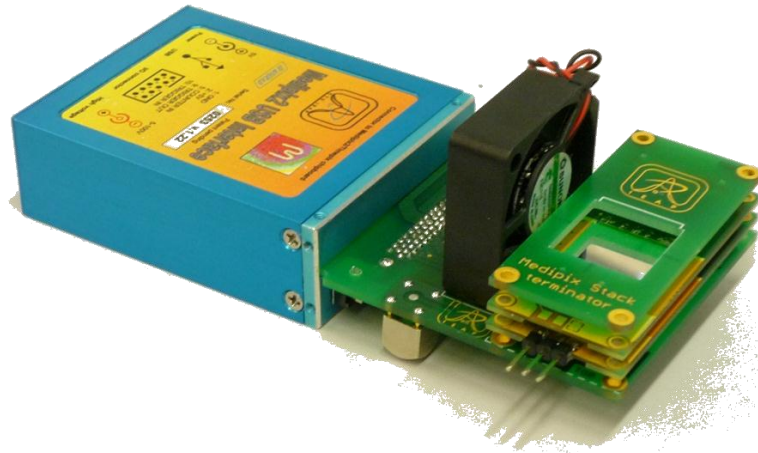
Figure 89. Two detector layers of stackable chipboard connected to the mother card with small fan to reduce the temperature of the setup (the absence of material below the chip limit the self-cooling capability of the chip through PCB). It is possible to stack several layers of Medipix or Timepix chips. They will be connected in daisy chain internally. The upper terminator board closes the daisy chain connection and serves as a mechanical protection of the chips below.

8.2.1 Combination of different sensor materials

Big advantage of this concept comes from the hybrid nature of the Medipix2 and Timepix chips. This allows easy combining of the sensitive layers made of different sensor materials and thicknesses in the telescope without any modifications in the readout hardware and software. An example showing the combination of the 300 μm thick Si top layer and 1 mm thick CdTe bottom layer is depicted in Fig. 90.
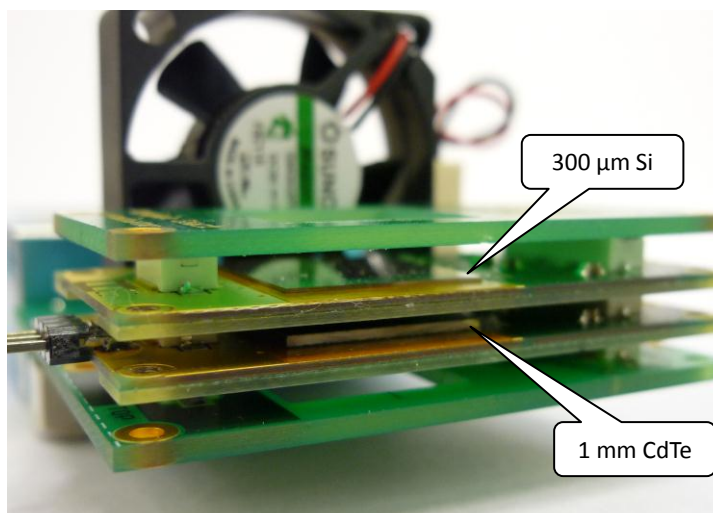
Figure 90. Detail of the two-layer detector setup. The top layer is assembled with the Timepix chip with 300 μm thick silicon sensor. Bottom layer is made of Timepix chip with 1 mm thick CdTe sensor. The distance between the layers is 3.6 mm in this case and can be tuned by means of the connector selection.

The silicon layer is biased by the positive voltage of 100 V (hole collection) while in the same time CdTe layer use the negative 300 V bias voltage (electron collection). Such combination can be used effectively as a Compton camera or in the field of radiation imaging. In the imaging applications, which have been studied in [39], one can benefit from the combination of these different material advantages. Si layer has higher homogeneity and spatial resolution and CdTe layer has higher detection efficiency for gamma radiation. Furthermore, this concept opens up new possibilities in the direction of material sensitivity studies (dual energy system) and scattering suppression.

8.2.2 Multilayer neutron detector

The experience from the analysis of the data from the ATLAS-MPX experiment shows that the detection of fast neutrons is extremely difficult in the field where neutrons are combined with energetic heavy charged particles. The neutron interactions in silicon produce the same characteristic clusters like proton interactions and with the small detection efficiency of the fast neutron conversion in PE layer (see subsection 5.3) it is difficult to distinguish contributions of those two components.

The independent information on position and energy or interaction time from the multiple sensor layers allows using the coincidence technique to separate neutron interactions (secondary heavy charged particles) from the interactions caused by primary heavy charged particles. This is achieved by adding the neutron converter material in between the sensitive layers. Two possible double layer layouts are visualized in Fig. 91.

First diagram on Fig. 91a presents the approach with the sensor layers facing in the same direction. In this case the top layer will remain sensitive to the very low energy photons and electrons (~10 keV). This configuration requires active airflow cooling to keep the temperature of the detectors at the reasonable values and the fast neutron detection is directionally insensitive.

Second diagram on Fig. 91b shows the configuration where sensors are facing each other. This configuration is capable of passive cooling and also allows evaluating the direction of the fast neutron interaction and also increases the overall neutron detection efficiency by factor two. However, low energy particles are effectively shielded by the readout chips and thin aluminum cooling layer.

In both cases by comparing the response of both sensitive layers following two conditions can be evaluated:

Coincidence: Interactions registered in both layers
- LETP signatures – minimum ionizing charge particles (muons, energetic electrons,…)
- HETP signatures – highly ionizing charged particles (~10 MeV protons,…)

Anticoincidence: Interactions registered in single layer only
- LETP signatures – photon interactions in one of the sensitive layers
- HETP signatures – fast neutron interactions in polyethylene region or thermal neutron interactions in ^{6}Li region
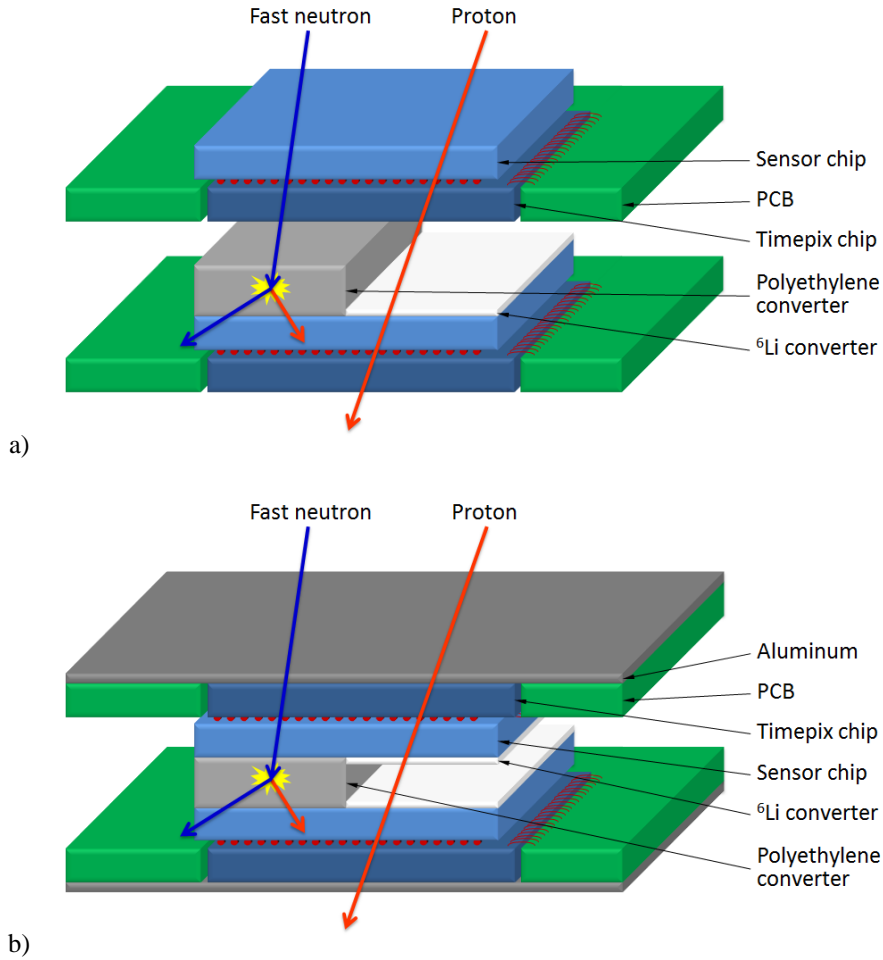
Figure 91: Two possible layouts of the two sensor layers with the neutron converter. a) Layout where sensors are facing the same direction has advantage of the low energy radiation sensitivity in the upper layer but there is insensitive Timepix readout chip in between the sensitive layers. b) Layout where sensor layers are facing each other has limited sensitivity to low energy radiation but the insensitive layer in between sensors can be minimized and aluminum plating provides better cooling potential as well as the mechanical protection.

The first tests of the coincidence neutron detector using multilayer detection system was done by Jan Jakubek [40] on in the secondary mixed field generated by the medical ^{12}C beam with the energy of 250 MeV/nucleon hitting the water tank. The example of the data analysis in the coincidence mode presented in [40] is shown in the Fig. 92. One can see clear separation of the anticoincident particle interactions and also the directional sensitivity of the coincident events.
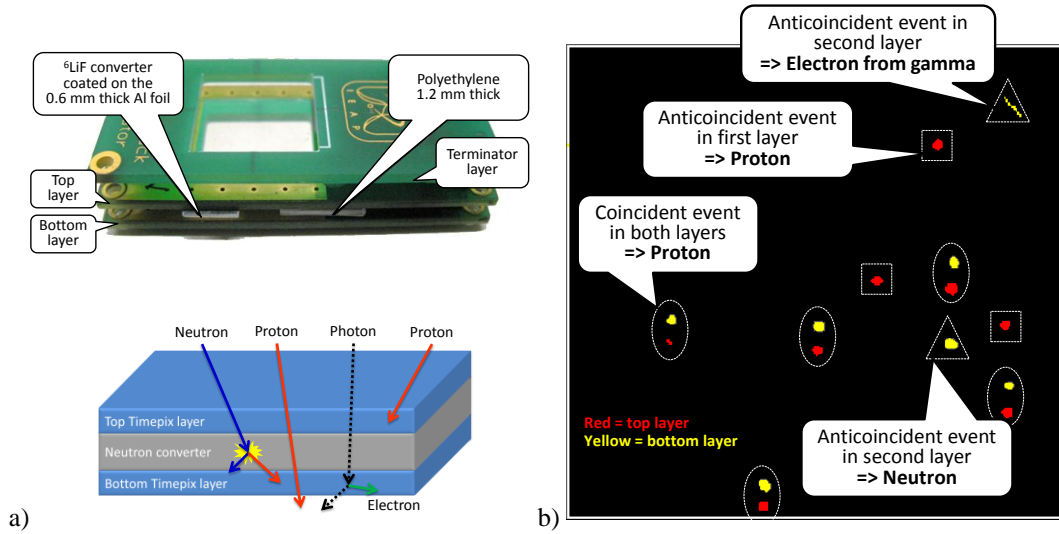
Figure 92. a) Photograph of the two layer Timepix setup, both with 300 μm thick silicon sensors, adapted for the neutron detection (top). Diagram of the Timepix detector layers showing different types of interactions. b) Response of the multilayer neutron detector in the mixed radiation field with the particle separation based on the coincidence technique presented at [40].

8.3 CdTe sensor material

As was discussed in the subsection 8.2.1 and before the hybrid Medipix2/Timepix technology allows using different semiconductor sensor materials in connection with the same readout chip. One of the available alternatives to the commonly used silicon sensors is cadmium telluride material.

In the case of radiation detectors applications it is strictly speaking cadmium zinc telluride (CdZnTe) material, an alloy of cadmium telluride and zinc telluride. Higher atomic numbers of cadmium (48) and tellurium (52) brings the advantage of higher sensitivity for X-rays and gamma-rays in comparison to silicon (14). CdZnTe can operate at room temperature and provide better energy resolution than scintillation detectors. On the other hand the heterogeneous structure of the material is causing local variations in the charge collection efficiency.

8.3.1 CdTe sensor homogeneity

A sample 1 mm thick CdTe Timepix assembly used for the measurements presented in this thesis has been scanned by the X-ray beam to measure 3D map of the charge collection efficiency using the method described in [41].

The narrow X-ray beam (10-20 μm in width) irradiates the sensor surface under the angle of 70° defining the interaction depth (volume) in several neighboring pixels. The maximal probe depth is limited by the initial X-ray beam intensity (90 kV tungsten X-ray tube in this case) and its attenuation in the sensor material (at some level the required information is lost in noise). The raw data obtained from scan needs was normalized for the attenuation of the beam in the sensor material (intensity depth profile). The 3D voxel matrix of the charge collection efficiency in measured sensor for different levels of the bias voltage created from the detector scan is depicted in Fig. 93.
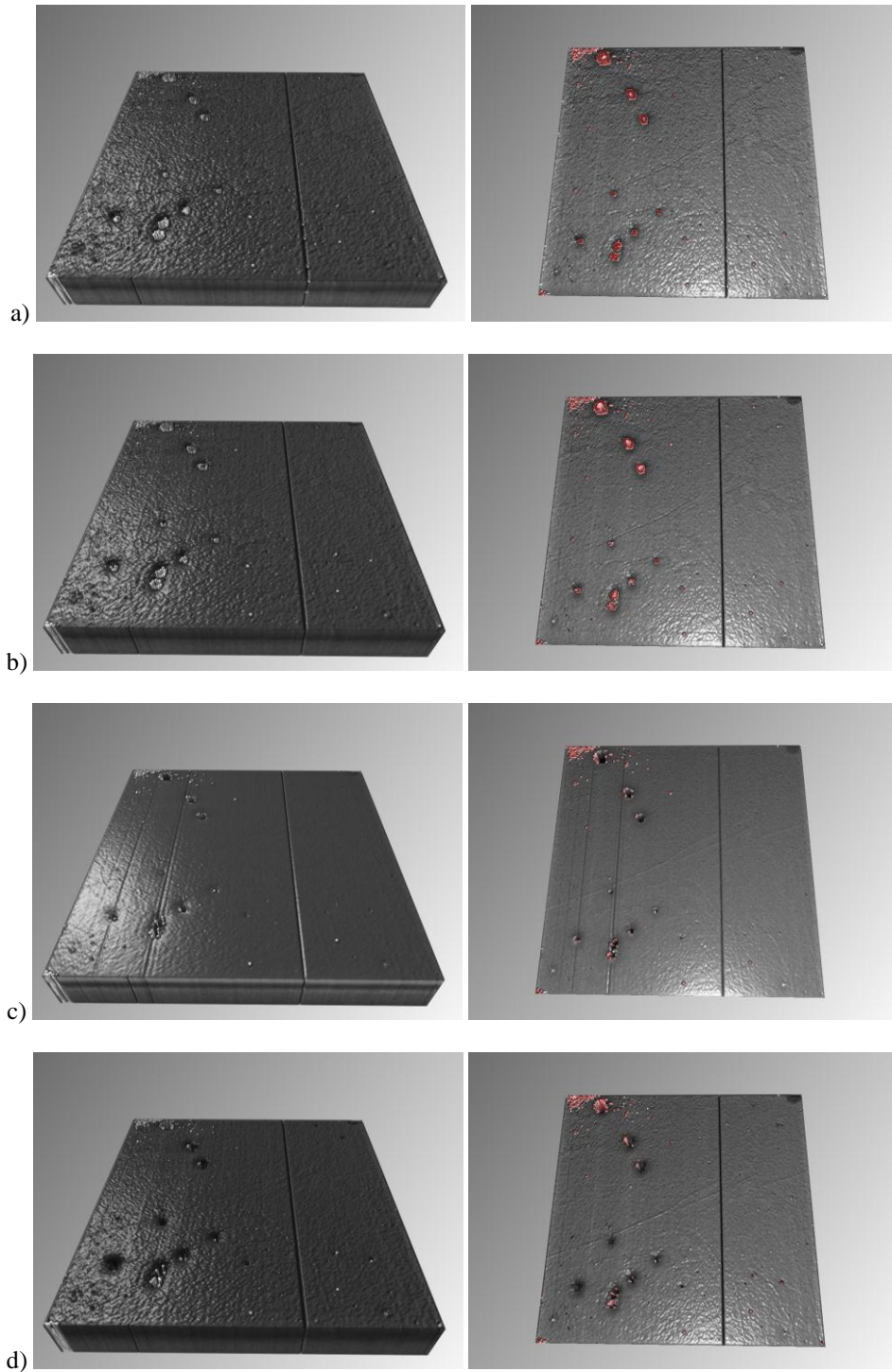
Figure 93. 3D map of the charge collection efficiency in the 1 mm thick CdTe sensor under different voltages. a) -100 V, b) -200 V, c) -300 V and d) -400 V. Visualization of the data was done in Voreen software [42].

One dead column of pixels can be seen in the 3D reconstructions of the charge collection efficiency as well as two types of local inhomogeneities.

First type is visualized as a round artifact with the deep conical shape. This is caused by increased leakage current which cause the local deformation of the electric field and thus charge collection efficiency. Second type can be seen as shallow line artifacts on the sensor surface. These are crystal grain boundaries of the CdTe material.

Only top part of the sensor can be visualized because of the limited X-ray energy of the used setup. Full scan would require X-ray beam with ~200 keV energy to be able to completely penetrate approximately 3000 µm of CdTe material in given geometry.

8.3.2 Comparison of the Si and CdTe detector responses to ^{137}Cs and ^{60}Co sources

Despite the inhomogeneities in the CdTe sensor material there are applications where higher sensitivity is more important than uniform response. For example the measurement of the radiation doses both for applications in the radiation protection and for estimation of the radiation damage of the detectors and electronics.

To evaluate the relative detection efficiency following three detector setups has been exposed to the ^{137}Cs and ^{60}Co photon sources used as well for the ATLAS-MPX detector dose rate calibration described in subsection 5.4:

- **ATLAS-MPX reference:** Medipix2 readout chip bump-bonded to the 300 µm thick silicon sensor covered by the neutron converter mask described in subsection 4.3.1.
- **CdTe:** Timepix chip bump-bonded to the uncovered 1 mm thick CdTe sensor.
- **Si + CdTe:** Combination of the Timepix chip bump-bonded to the uncovered 300 µm thick silicon sensor (top layers) and Timepix chip bump-bonded to the 1 mm thick CdTe sensor (bottom layer).

Images from the combined Si + CdTe detector irradiated by ^{137}Cs and ^{60}Co sources are shown in the Fig. 94 demonstrating higher sensitivity of the CdTe layer especially to the 662 keV photons from ^{137}Cs source. The detection efficiencies and cluster composition of the three compared devices relatively to the ATLAS-MPX reference detector are summarized in Tab. 11 for ^{137}Cs source and Tab. 12 for ^{60}Co source.

From Tab. 11 one can see that the single layered CdTe device has 7.6-times higher detection efficiency than single layered silicon device. Because of the CdTe device thickness the charge diffusion effect is much stronger compared to thinner Si and the particle miscategorization in the particle counting Medipix2 mode is at the level of 3%. The efficiency of the combined Si + CdTe device is 8.4-times higher than ATLAS-MPX reference detector. The first Si layer in the combined device has larger relative detection efficiency compared to the ATLAS-MPX reference detector because of photon attenuation in the neutron conversion layers above the reference device. However, the relative cluster composition remains almost the same.
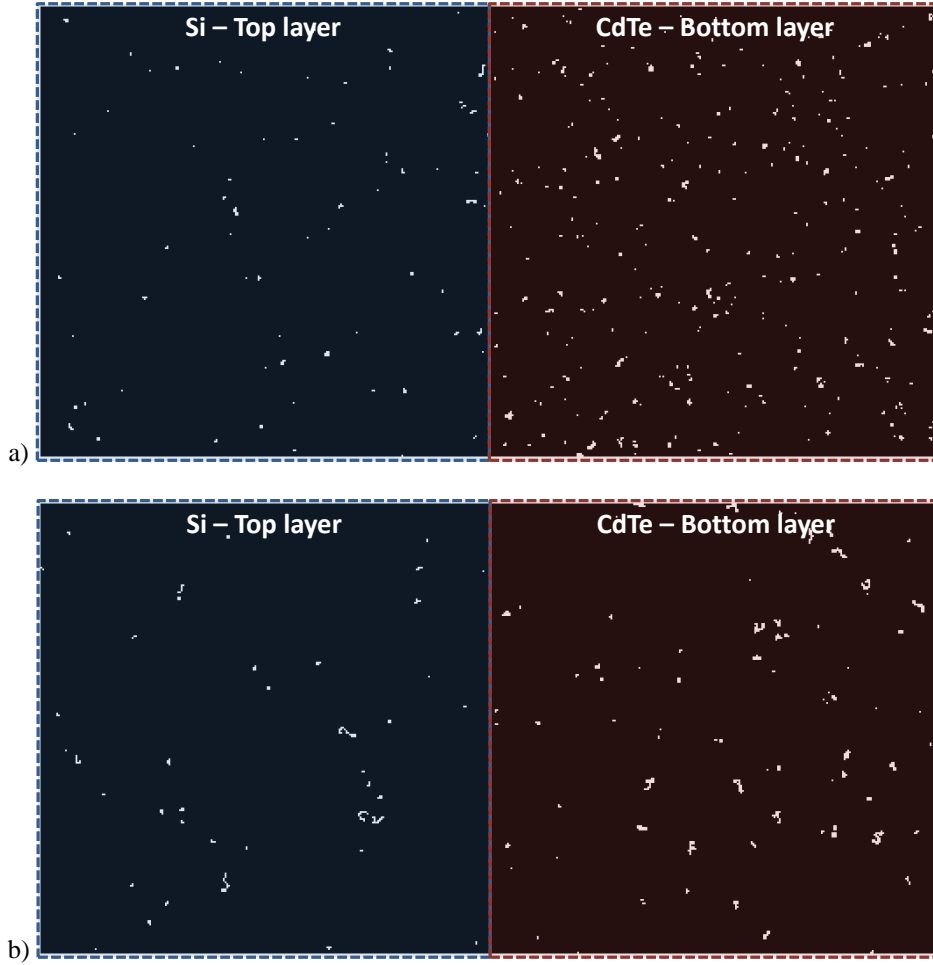
Figure 94. Response of the double-layered 300 μm thick silicon (top layer) and 1 mm thick CdTe (bottom layer) Timepix device to the radiation from a) ^{137}Cs source b) ^{60}Co source.

Device	All clusters	Cluster composition					
		Dot	Small blob	Curly track	Heavy blob	Heavy track	Straight track
ATLAS-MPX reference	100%	41%	33%	25%	1%	0%	0%
CdTe	764%	47%	38%	12%	3%	0%	0%
Si + CdTe	840%	40%	40%	16%	3%	0%	0%
Si (top layer)	153%	40%	31%	27%	1%	0%	0%
CdTe (bottom layer)	687%	41%	42%	14%	3%	0%	0%

Table 11. Relative comparison of the response and cluster composition of the 300 μm thick silicon, 1 mm thick CdTe and their combination to the ^{137}Cs source. CdTe detector show 7.6-times higher detection efficiency and combined device 8.4-times higher efficiency than single layer silicon device.

Device	All clusters	Cluster composition					
		Dot	Small blob	Curly track	Heavy blob	Heavy track	Straight track
ATLAS-MPX reference	100%	12%	24%	62%	2%	0%	0%
CdTe	303%	18%	32%	39%	9%	2%	0%
Si + CdTe	420%	15%	30%	48%	6%	2%	0%
Si (top layer)	165%	10%	25%	63%	2%	0%	0%
CdTe (bottom layer)	255%	18%	32%	38%	9%	3%	0%

Table 12. Relative comparison of the response and cluster composition of the 300 µm thick silicon, 1 mm thick CdTe and their combination to the ^{60}Co source. CdTe detector show 3-times higher detection efficiency and combined device 4-times higher efficiency than single layer silicon device.

Table 12 show the 3-times higher response of the single CdTe layer and 4.2-times larger response of the combined device in comparison to the ATLAS-MPX reference detector. The response of the first Si layer in the combined device is larger compared to the ATLAS-MPX reference detector because of photon attenuation in the neutron conversion layers above the reference device as before. The relative cluster composition is preserved as well. The probability of the particle miscategorization rise from 2% in Si to 11% of wrongly identified heavy events in CdTe device. However, further criteria on cluster height or volume from the TOT mode of operation (see subsection 8.1.2) can be used in this case to eliminate this issue.

9. Thesis summary

The results presented in this thesis have proven that the single photon counting pixel detectors from the Medipix family are excellent tools for investigation of the complex radiation field properties. Using methodology presented in section 3 it can provide information on the spectral composition of the radiation field by means of analysis of the characteristic clusters created by individual radiation particle interactions.

This concept was successfully used in the network of 16 ATLAS-MPX detectors installed within the ATLAS experiment at CERN. The network has been running continuously starting from early 2008 (background and cosmic radiation measurements) through the stable LHC operation during the 2010 and 2011 run periods (collision data) up to nowadays.

Each installed ATLAS-MPX detector and several reference units was equipped with the mask of neutron conversion materials described in subsection 4.3.1 and individually calibrated in the different photon and neutron fields to measure the detector efficiency for neutral particles. The process of the calibration and the efficiency values are presented in section 5.

The primary goals of the ATLAS-MPX network was initially to measure the radiation field inside the ATLAS detector volume with focus on neutron component to be used for the validation of the early Monte Carlo predictions about radiation field in ATLAS in the experimental hall and the detector surroundings. During the network operation it appeared that it is possible to use the network as an independent luminosity monitor as well as for measurements of the induced radioactivity in between and after collisions.

According to their characteristic signatures the measured particle types have been separated into categories of particles with low energy transfer (LETP - electrons, gamma rays, X-rays), particles with high energy transfer (HETP - alphas, protons, heavier ions, fast neutrons, minimum ionizing particles (MIP – energetic charged particles passing the detector under defined angle) and thermal neutrons. The LETP, HETP, MIP cluster rate and thermal neutron fluxes normalized per luminosity unit during collisions were measured for each ATLAS-MPX detector as presented in subsection 6.2.

The linear correlation between clusters rate of each radiation species or counts recorded in each ATLAS-MPX detector at a given time and the LHC machine luminosity was evaluated in subsection 6.3. It gives the ATLAS-MPX detectors the capability of bringing real-time information on beam conditions and to directly visualize any beam manipulation including beam set-up, adjustment and luminosity scans performed according the van der Meer method.

The residual material activation in the ATLAS environment was measured through the detection of gamma decay of instable radionuclides produced by the interaction of collision particles with these materials. The induced activation as measured with an MPX detector is analyzed in terms of short and long decay components with the cluster rate measured after the end of collisions. This analysis exhibits up to four decay components with the following half-lives: a few minutes, a few hours, several tens of hours and longer than 50 days (see Fig. 75). Comparison with dose rate calibration measurements which has been done with gamma ray sources (see subsection 5.4) provide value of a mean photon ambient dose equivalent rate as presented in subsection 6.5.

Measurements of the LETP, HETP, MIP cluster rate and thermal neutron flux obtained with each ATLAS-MPX detector were compared to corresponding output from Monte Carlo simulations as evaluated in section 7.

The measured LETP average registered cluster rate is found to be in good agreement within factor of two with Monte Carlo prediction of electron and photon currents. Only rough comparison of the simulated proton currents and HETP measured with ATLAS-MPX detectors has been done showing rather significant differences. The reason is that HETP signal can be caused also by other energetic charged particles (protons, pions, kaons…) as well as by fast neutron interactions. Similarly to HETP particles, only a rough comparison of measured MIP particles with simulated muon data was done. The MIP signal measured with ATLAS-MPX detectors include signal from all energetic charged particles which create a thin straight track of at least 20 pixels length (including electrons, protons, pions...). Further studies including the detailed Monte Carlo simulations of the ATLAS-MPX detector response have to be performed to include conversion, energy and angular efficiencies for all the simulated particles to be correctly assigned to the LETP, HETP or MIP category. This detailed comparison will be part of the prepared comprehensive ATLAS-MPX report [32].

The comparison of the average thermal neutron fluence per luminosity unit during collisions shows a fair agreement within a factor of two. Significant deviations are observed in the low radiation region of the UX15 cavern, where the measured thermal neutron flux is found to be lower than simulated mainly because of the poor statistics in the simulated data for larger distances from the interaction point.

The inability of the evaluation of the fast neutron component and discrimination of orthogonally incident MIP particles from low energy electrons and photons in the complex radiation field which is present in ATLAS require use of more sophisticated detection system capable to measure also the energy and direction of the incident particles. This can be possibly achieved by adding a multilayer detector equipped with the Timepix readout chips [37] as described in section 8. The Timepix detector allows direct energy measurement in each pixel and the double layer construction allows using coincidence techniques to separate fast neutron component of the radiation field and

provides the information on the interactions direction as well. The possible advantages of usage of the CdTe sensor material have been evaluated. In addition, an increase of the data readout speed by factor of 50 is foreseen [19], thus reducing the measurements dead time significantly. This major upgrade of the ATLAS-MPX network is in preparation for the long LHC shut down planned for years 2013-2014.

The results presented in this thesis have proven to be an important feedback for ATLAS community and will possibly allow the calculation of the safety factors to be used in the future to determine the viability of the ATLAS electronics exposed to growing doses of neutrons and photons, in particular in view of planned LHC upgrade. There is a growing interest in these results also from the other large LHC experiments. Several ATLAS-MPX type devices were installed also in the CMS detector [45] and newly two Timepix units were installed in the MoEDAL experiment [46].

References

[1] X. Llopart, M. Campbell, R. Dinapoli, D. San Segundo and E. Pernigotti, *Medipix2: a 64-k Pixel Readout Chip With 55-μm Square Elements Working in Single Photon Counting Mode*, IEEE Transactions on Nuclear Science, Vol. 49, 2002. doi:10.1109/TNS.2002.803788

[2] M. Campbell, C. Leroy, S. Pospisil, M. Suk, *Measurement of Spectral Characteristics and Composition of Radiation in ATLAS by MEDIPIX2-USB Devices*, Project proposal, 2006. Available at https://edms.cern.ch/document/815615

[3] T. Holy, J. Jakubek, S. Pospisil, J. Uher, Z. Vykydal, Z. Dolezal, M. Suk, I. Wilhelm, M. Campbell, E. Heijne, X. Lopart, L. Tlustos, C. Leroy, B. Mikulec, M. Nessi, C. Buttar, V. O'Shea, K.M. Smith, *Proposal to measure spectral characteristics and composition of radiation in ATLAS by MEDIPIX2-USB Devices,* Project technical note, 2006. Available at https://edms.cern.ch/document/815615

[4] G.F. Knoll, *Radiation detection and measurements*, John Willey and Sons, Inc., New York 2000. ISBN 0-471-07338-5

[5] J.F. Ziegler, J.P. Biersack, M.D. Ziegler, *SRIM - The Stopping and Range of Ions in Matter*, Simulation software package available at http://www.srim.org

[6] M.J. Berger (NIST), *ESTAR - Stopping powers and ranges for electrons*, Online service available at http://atom.kaeri.re.kr/

[7] M.J. Berger (NIST), *XCOM - Photon cross sections and attenuation coefficients*, Online service available at http://atom.kaeri.re.kr/

[8] S. Pospisil, B. Sopko, E. Havrankova, Z. Janout, J. Konicek, I. Macha and J. Pavlu, *Si Diode as a Small Detector of Slow Neutrons*, Radiation Protection Dosimetry, Vol. 46, 1993. Available at http://rpd.oxfordjournals.org/content/46/2/115

[9] S. Pospisil, *Spektrometrie rychlých neutronů pomocí polovodičových detektorů metodou odražených protonů*, Diploma thesis, Czech Technical University in Prague, 1964.

[10] J. Uher, *3D neutron detectors*, Doctoral thesis, Czech Technical University in Prague, 2007.

[11] *JANIS - Java-based nuclear data display program*, Software package available at http://www.nea.fr/abs/html/nea-1760.html

[12] Z. Vykydal, *Microprocessor controlled USB interface for Medipix2 detector*, Diploma thesis, Czech Technical University in Prague, 2005.

[13] E. Belau, et al., *Silicon detectors with 5 μm spatial resolution for high energy particles*, Nuclear Instruments and Methods A, Vol. 217, 1983. doi:10.1016/0167-5087(83)90138-2

[14] CERN Medipix2 collaboration at http://www.cern.ch/medipix

[15] D. San Segundo Bello, M. Van Beuzekom, P. Jansweijer, H. Verkooijen, J. Visschers, *An interface board for the control and data acquisition of the Medipix2 chip*, Nuclear Instruments and Methods A, Vol. 509, 2003. doi:10.1016/S0168-9002(03)01566-3

[16] C. Ponchut, J. Clement, J. Rigal, E. Papillon, J. Vallerga, D. LaMarra, B. Mikulec, *A noiseless kilohertz frame rate imaging detector based on microchannel plates read out with the Medipix2 CMOS pixel chip*, Nuclear Instruments and Methods A, Vol. 567, 2006. doi: 10.1016/j.nima.2006.05.063

[17] Z. Vykydal, J. Jakubek, S. Pospisil, *USB interface for Medipix2 pixel device enabling energy and position sensitive detection of heavy charged particles*, Nuclear Instruments and Methods A, Vol. 563, 2006. doi:10.1016/j.nima.2006.01.114

[18] Z. Vykydal, J. Jakubek, *USB Lite - Miniaturized readout interface for Medipix2 detector*, Nuclear Instruments and Methods A, Vol. 633, 2011. doi:10.1016/j.nima.2010.06.118

[19] V. Kraus, M. Holik, J. Jakubek, M. Kroupa, P. Soukup, Z. Vykydal, *FITPix - Fast Interface for Timepix Pixel Detectors*, Journal of Instrumentation 6 C01079, 2011. doi:10.1088/1748-0221/6/01/C01079

[20] D. Turecek, T. Holy, J. Jakubek, S. Pospisil, Z. Vykydal, *Pixelman: a multi-platform data acquisition and processing software package for Medipix2, Timepix and Medipix3 detectors*, Journal of Instrumentation 6 C01046, 2011. doi:10.1088/1748-0221/6/01/C01046

[21] T. Holy, J. Jakubek, S. Pospisil, J. Uher, D. Vavrik, Z. Vykydal, *Data acquisition and processing software package for Medipix-2 device*, Nuclear Instruments and Methods A, Vol. 563, 2006. doi:10.1016/j.nima.2006.01.122

[22] T. Holy, E. Heijne, J. Jakubek, S. Pospisil, J. Uher and Z. Vykydal, *Pattern recognition of tracks induced by individual quanta of ionizing radiation in Medipix2 silicon detector*, Nuclear Instruments and Methods A, Vol. 591, 2008. doi:10.1016/j.nima.2008.03.074

[23] J. Bouchami, A. Gutierrez, T. Holy, A. Houdayer, J. Jakubek, C. Lebel, C. Leroy, J. Macana, J. Martin, S. Pospisil, S. Prak, P. Sabella, C. Teyssier, *Measurement of pattern recognition efficiency of tracks generated by ionizing radiation in a Medipix2 device*, Nuclear Instruments and Methods A, Vol. 633, 2011, doi:10.1016/j.nima.2010.06.163

[24] CERN - European Organization for Nuclear Research at http://www.cern.ch

[25] ATLAS Collaboration, *The ATLAS Experiment at the CERN Large Hadron Collider*, Journal of Instrumentation 3 S08003, 2008. doi:10.1088/1748-0221/3/08/S08003

[26] Z. Vykydal, J. Bouchami, M. Campbell, Z. Dolezal, M. Fiederle, D. Greiffenberg, A. Gutierrez, E. Heijne, T. Holy, J. Idarraga, J. Jakubek, V. Kral, M. Kralik, C. Lebel, C. Leroy, X. Llopart, D. Maneuski, M. Nessi, V. O'Shea, M. Platkevic, S. Pospisil, M. Suk, L. Tlustos, P. Vichoudis, J. Visschers, I. Wilhelm, J. Zemlicka, *The Medipix2-Based Network for Measurement of Spectral Characteristics and Composition of Radiation in ATLAS Detector*, Nuclear Instruments and Methods A, Vol. 607, 2009, doi:10.1016/j.nima.2009.03.104

[27] Operation page of the ATLAS-MPX network measurements at http://www.cern.ch/Atlas

[28] M. Fiederle, D. Greiffenberg, J. Idarraga, J. Jakubek, V. Kral, C. Lebel, C. Leroy, G. Lord, S. Pospisil, V. Sochor, M. Suk, *Energy calibration measurements of MediPix2*, Nuclear Instruments and Methods A, Vol. 591, 2008. doi:10.1016/j.nima.2008.03.042

[29] J. Jakubek, *Precise Energy Calibration of Pixel Detector Working in Time-Over-Threshold Mode*, Nuclear Instruments and Methods A, Vol. 633, 2011. doi:10.1016/j.nima.2010.06.183

[30] D. Greiffenberg, M. Fiederle, Z. Vykydal, V. Kral, J. Jakubek, T. Holy, S. Pospisil, D. Maneuski, V. O'Shea, M. Suk, M. Kralik, C. Lebel, C. Leroy, *Detection efficiency of ATLAS-MPX detectors with respect to neutrons*, Nuclear Instruments and Methods A, Vol. 607, 2009. doi:10.1016/j.nima.2009.03.103

[31] Z. Vykydal, J. Bouchami, M. Campbell, Z. Dolezal, M. Fiederle, D. Greiffenberg, A. Gutierrez, E. Heijne, T. Holy, J. Idarraga, J. Jakubek, V. Kral, M. Kralik, C. Lebel, C. Leroy, X. Llopart, D. Maneuski, M. Nessi, V. O'Shea, M. Platkevic, S. Pospisil, V. Sochor, J. Solc, M. Suk, L. Tlustos, P. Vichoudis, J. Visschers, I. Wilhelm, J. Zemlicka, *Evaluation of the ATLAS-MPX Devices for Neutron Field Spectral Composition Measurement in the ATLAS Experiment*, 2008 IEEE Nuclear Science Symposium Conference Record, 2009. doi:10.1109/NSSMIC.2008.4774829

[32] M. Campbell, E. Heijne, C. Leroy, J.P. Martin, G. Mornacchi, M. Nessi, S. Pospisil, J. Solc, P. Soueid, M. Suk, D. Turecek and Z. Vykydal, *First Analysis of the Radiation Field in ATLAS using 2008-2011 Data from the ATLAS-MPX Network*, ATLAS internal note, in preparation.

[33] The ATLAS Collaboration, *Luminosity Determination in pp Collisions at √s = 7 TeV Using the ATLAS Detector at the LHC*, Eur. Phys. J. C, Vol. 71, 2011. doi:10.1140/epjc/s10052-011-1630-5

[34] The ATLAS Collaboration, *Luminosity Determination in pp Collisions at √s = 7 TeV using the ATLAS Detector in 2011*, ATLAS-COM-CONF-2011-130, 2011. Available at https://cdsweb.cern.ch/record/1367408

[35] Radiation Background Task Force, *Predicted Radiation levels in ATLAS*, Available at http://atlas.web.cern.ch/Atlas/GROUPS/PHYSICS/RADIATION/Radiation_Levels.html

[36] M. Shupe, Private communication, 2010.

[37] X. Llopart, R. Ballabriga, M. Campbell, L. Tlustos, W. Wong, *Timepix, a 65k programmable pixel readout chip for arrival time, energy and/or photon counting measurements*, Nuclear Instruments and Methods A, Vol. 581, 2007. doi:10.1016/j.nima.2007.08.079

[38] P. Soukup, J. Jakubek, Z. Vykydal, *3D sensitive voxel detector of ionizing radiation based on Timepix device*, Journal of Instrumentation 6 C01060, 2011. doi:10.1088/1748-0221/6/01/C01060

[39] Z. Vykydal, A. Fauler, M. Fiederle, J. Jakubek, P. Soukup, A. Fauler, *Combined Medipix based imaging system with Si and CdTe sensor*, 2011 IEEE Nuclear Science Symposium Conference Record, 2012. doi:10.1109/NSSMIC.2011.6154710

[40] J. Jakubek, *Imaging Based on Tracking of Individual Particles with the Timepix Pixel Detector*, Presentation at the 9th International Conference on Position Sensitive Detectors (PSD9), Aberystwyth, United Kingdom, 12-16. Sep 2011.

[41] J. Zemlicka, J. Jakubek, M. Jakubek, Z. Vykydal, G. Chelkov, V. Kruchonok, V. Elkin, M. Fiederle, A. Fauler, O. Tolbanov, A. Tyazhev, J. Visser, *X-ray based methods for 3D characterization of charge collection and homogeneity of sensors with the use of Timepix*

chip, 2011 IEEE Nuclear Science Symposium Conference Record, 2012. doi:10.1109/NSSMIC.2011.6154764

[42] J. Meyer-Spradow, T. Ropinski, J. Mensmann, K.H. Hinrichs, *Voreen: A Rapid-Prototyping Environment for Ray-Casting-Based Volume Visualizations*, IEEE Computer Graphics and Applications, Vol. 29, 2009. doi:10.1109/MCG.2009.130

[43] S. Baranov, M. Bosman, I. Dawson, V. Hedberg, A. Nisati and M. Shupe, *Estimation of Radiation Background Impact on Detectors, Activation and Shielding Optimization in ATLAS*, ATL-GEN-2005-001, 2005. Available at https://cdsweb.cern.ch/record/814823

[44] ICRU Report 85, *Fundamental Quantities and Units for Ionizing Radiation*, Journal of the ICRU, Vol. 11, 2011. doi:10.1093/jicru/ndr012

[45] A. Ball, A. Bell, A. Butler, S. Pospíšil, Z. Vykydal, . et al., *Design, implementation and first measurements with the Medipix2-MXR detector at the Compact Muon Solenoid experiment*, Journal of Instrumentation 6 P08005, 2011. doi:10.1088/1748-0221/6/08/P08005

[46] CERN MoEDAL collaboration blog at http://moedal.web.cern.ch/blog

Appendix A - DCS data available in ATLAS Control Room

The ATLAS-MPX page in DCS shows count rate of all events in Hz.cm^{-2} (see Fig. 95). In the top part of the image the positions of the detectors are shown together with actual count rate calculated from last measured frame. In the bottom part, two charts show history of count rate in the last 8 hours for detectors MPX01 and MPX15. It is possible to visualize other detectors by selecting the corresponding checkbox in each chart.
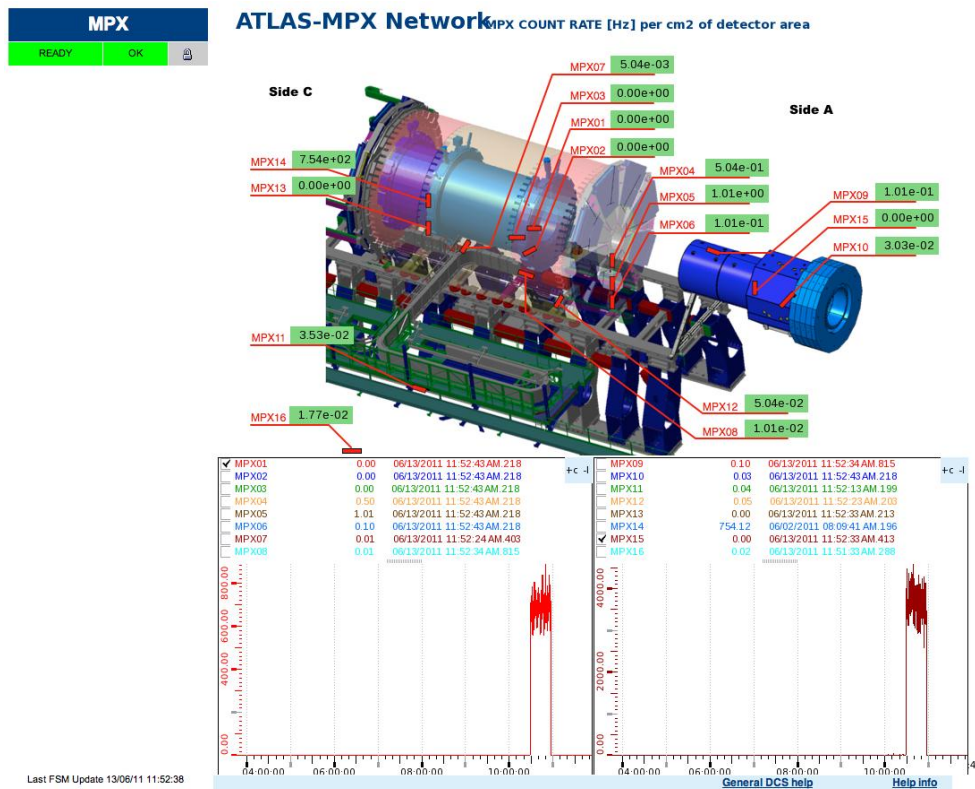
Figure 95. Screenshot of the ATLAS-MPX DCS webpage.

Unfortunately too many different variables prevent sending all the available information to the central ATLAS DCS database. However, the ATLAS-MPX network provides DCS data for each detector, namely:

- CNT_ALL   - number of clusters in a frame normalized to 1 second
- FLX_ALL   - number of clusters in a frame normalized to 1 second and cm^2
- STG   - settings id number
- TIME_STAMP - start time of the frame CNT_ALL and FLX_ALL
- DEV_STATUS - status of the detector

113

Appendix B - Quantities and units for ionizing radiation used in this thesis

9.1 Radiation field quantities

For the description of the radiation field the physical quantities: **particle current**, **particle fluence** and **particle flux** have been used as defined in a similar way in Appendix II of [43].

Although the nomenclature and definitions differ from the official ones described in ICRU 85 [44], the quantities used in this thesis are more applicable to the data obtained with a two-dimensional, planar, square pixelated chip of ATLAS-MPX detectors. Furthermore, it allows easier comparison with Monte Carlo calculations.

- **Particle current** is defined as the number of particles of a given type crossing through a given plane, normalized to the area of this plane and to time unit. The given plane is in our case the MPX sensor chip surface with the area of approximately 2 cm^2.
- **Particle fluence** is defined as the number of particles of a given type incident on a sphere of cross sectional area, normalized to this area.
- **Particle flux** is defined as the particle fluence, normalized to time unit. This means that the fluence and flux are independent on particle direction, in contrast to the particle current. Because the MPX sensor chip is not spherical, the particle current obtained from measured cluster rate cannot be recalculated into flux without the knowledge of radiation field anisotropy and ATLAS-MPX device angular response. The only exception is a radiation field of thermalized neutrons which is supposed to be isotropic and therefore identical with the reference field used for ATLAS-MPX detectors calibration.

9.2 Radiation protection quantities

For the description of the ATLAS radiation field for radiation protection purpose the quantity H*(10) - **photon ambient dose equivalent** has been used. This measurable quantity used in radiation protection surrogates the effective dose describing the biological effectiveness of the absorbed dose in different human tissues. In this thesis, H*(10) is used only for quantification of radiation field caused by activation products, i.e., photon radiation, and not mixed radiation field occurring during LHC runs. ATLAS-MPX device was calibrated in reference photon fields to obtain a conversion from measured cluster rate to photon ambient dose equivalent rate (see subsection 5.4).

Appendix C - Determination of neutron resonance integral

Resonance integral is in direct relation to the number of interactions of a given type (e.g. (n,α)) of neutrons with energies in a given energy interval. It is calculated as a sum (integral) of a product of neutron flux and the corresponding cross section. Using the cross section presented in Fig. 8 and neutron spectra obtained from GCALOR simulations (four examples are showed in Fig. 82), two resonance integrals were calculated:

- the first one (I_{th}) from 0 to 1 eV (approximate energy range of thermal neutrons),
- the second one (I_0) from 0 eV to infinity (energy range of all neutrons which could contribute to the measured signal).

Ratio I_{th}/I_0 is ≤ 1. The measured uncorrected thermal neutron flux was multiplied by this ratio to obtain the actual thermal neutron flux. Corrections are summarized in Tab. 13. Note that the correction is at level of 3 - 8% for all ATLAS-MPX detectors except for MPX15 where the correction reaches 82%. The new value of the thermal neutron flux at MPX15 is now in good agreement with Monte Carlo prediction.

Detector	Total resonance integral for ^{6}Li per luminosity unit [nb^{-1}]			Thermal (E < 1 eV) resonance integral for ^{6}Li per luminosity unit [nb^{-1}]		Thermal neutron fluence per luminosity unit [cm^{-2}/nb^{-1}]			
	MC calculation	ATLAS-MPX measurement	Ratio MC/ MPX	MC calculation	MC ratio Thermal/ Total	ATLAS-MPX measurement Without correction	With correction	MC calculation	Ratio MC/ MPX
MPX01	1.68E+07	2.439E+07	0.69	1.55E+07	0.93	49600	45933	38568	0.84
MPX02	1.64E+06	NA	0.98	1.54E+06	0.94	1728	1622	3835	2.36
MPX03	1.93E+05	1.744E+05	1.11	1.86E+05	0.96	283	273	459	1.68
MPX04	3.17E+06	1.668E+06	1.90	3.07E+06	0.97	3302	3202	7553	2.36
MPX05	4.53E+05	4.457E+05	1.02	4.24E+05	0.94	785	736	1029	1.40
MPX06	2.26E+05	1.506E+05	1.50	2.09E+05	0.92	226	209	521	2.50
MPX07	2.61E+04	4.551E+03	5.72	2.43E+04	0.93	7.1	6.6	63	9.50
MPX08	2.35E+04	1.081E+04	2.17	2.18E+04	0.93	17.4	16.1	56	3.47
MPX09	4.09E+04	1.506E+04	2.72	3.95E+04	0.96	29.4	28.4	100	3.54
MPX10	2.75E+04	1.085E+04	2.53	2.67E+04	0.97	20.5	19.9	66	3.31
MPX11	4.00E+04	2.381E+03	16.80	3.89E+04	0.97	2.9	2.9	96	33.50
MPX12	6.04E+04	3.719E+04	1.62	5.68E+04	0.94	65	61	140	2.29
MPX13	1.64E+06	1.664E+06	0.98	1.54E+06	0.94	2868	2693	3835	1.42
MPX14	1.68E+07	2.374E+07	0.71	1.55E+07	0.93	41270	38219	38568	1.01
MPX15	1.44E+08	9.288E+07	1.55	2.59E+07	0.18	211400	38092	33351	0.88

Table 13. Resonance integrals for (n,α) reaction on ^{6}Li obtained from GCALOR calculated neutron energy spectra and corrections of measured thermal neutron fluence to the signal not caused by thermal neutrons.

Appendix D - List of related author's publications

2012

[1] Z. Vykydal, M. Holik, V. Kraus, S. Pospisil, J. Solc, D. Turecek, *A Highly Miniaturized and Sensitive Thermal Neutron Detector for Space Applications*, American Institute of Physics (AIP) Conference Proceedings, Vol. 1423, 2012, doi:10.1063/1.3688833

[2] Z. Vykydal, A. Fauler, M. Fiederle, J. Jakubek, P. Soukup, A. Fauler, *Combined Medipix based imaging system with Si and CdTe sensor*, 2011 IEEE Nuclear Science Symposium Conference Record, 2012. doi:10.1109/NSSMIC.2011.6154710

[3] J. Zemlicka, J. Jakubek, M. Jakubek, Z. Vykydal, G. Chelkov, V. Kruchonok, V. Elkin, M. Fiederle, A. Fauler, O. Tolbanov, A. Tyazhev, J. Visser, *X-ray based methods for 3D characterization of charge collection and homogeneity of sensors with the use of Timepix chip*, 2011 IEEE Nuclear Science Symposium Conference Record, 2012. doi:10.1109/NSSMIC.2011.6154764

[4] M. Platkevic, P. Cermak, J. Jakubek, S. Pospisil, I. Stekl, Z. Vykydal, J. Zemlicka, C. Leroy, P. Allard, G. Bergeron, P. Soueid, C. Teyssier, R. Yapoudjian, M. Fiederle, A. Fauler, G. Chelkov, O. Toblanov, A. Tyazhev, J. Visser, *Characterization of Charge Collection in Various Semiconductor Sensors with Energetic Protons and Timepix Device*, 2011 IEEE Nuclear Science Symposium Conference Record, 2012. doi:10.1109/NSSMIC.2011.6154765

2011

[5] Z. Vykydal, J. Jakubek, *USB Lite - Miniaturized readout interface for Medipix2 detector*, Nuclear Instruments and Methods A, Vol. 633, 2011. doi:10.1016/j.nima.2010.06.118

[6] Z. Vykydal, A. Fauler, M. Fiederle, J. Jakubek, M. Svestkova, A. Zwerger, *Medipix2 based CdTe microprobe for dental imaging*, Journal of Instrumentation 6 C12002, 2011. doi:10.1088/1748-0221/6/12/C12002

[7] A. Ball, A. Bell, A. Butler, S. Pospíšil, Z. Vykydal, . et al., *Design, implementation and first measurements with the Medipix2-MXR detector at the Compact Muon Solenoid experiment*, Journal of Instrumentation 6 P08005, 2011. doi:10.1088/1748-0221/6/08/P08005

[8] V. Kraus, M. Holik, J. Jakubek, M. Kroupa, P. Soukup, Z. Vykydal, *FITPix - Fast Interface for Timepix Pixel Detectors*, Journal of Instrumentation 6 C01079, 2011. doi:10.1088/1748-0221/6/01/C01079

[9] D. Turecek, T. Holy, J. Jakubek, S. Pospisil, Z. Vykydal, *Pixelman: a multi-platform data acquisition and processing software package for Medipix2, Timepix and Medipix3 detectors*, Journal of Instrumentation 6 C01046, 2011. doi:10.1088/1748-0221/6/01/C01046

[10] P. Soukup, J. Jakubek, Z. Vykydal, *3D sensitive voxel detector of ionizing radiation based on Timepix device*, Journal of Instrumentation 6 C01060, 2011. doi:10.1088/1748-0221/6/01/C01060

2010

[11] E. Heijne, R. Ballabriga, D. Boltje, M. Campbell, J. Idarraga, J. Jakubek, C. Leroy, X. Llopart, L. Tlustos, R. Plackett, S. Pospisil, D. Turecek, J. Vermeulen, J. Visschers, J. Visser, Z. Vykydal, W. Wong, *Vectors and submicron precision: redundancy and 3D stacking in silicon pixel detectors*, Journal of Instrumentation 5 C06004, 2010. doi:10.1088/1748-0221/5/06/C06004

[12] C. Granja, V. Kraus, J. Jakubek, S. Pospisil, P. Masek, Z. Vykydal, M. Platkevic, Z. Kohout, Y. Kopatch, S. Telezhnikov, U. Koester, J. Vacik, I. Tomandl, *Spatially Correlated and Coincidence Detection of Fission Fragments with the Pixel Detector Timepix*, 2010 IEEE Nuclear Science Symposium Conference Record, 2010. doi:10.1109/NSSMIC.2010.5874042

2009

[13] Z. Vykydal, J. Bouchami, M. Campbell, Z. Dolezal, M. Fiederle, D. Greiffenberg, A. Gutierrez, E. Heijne, T. Holy, J. Idarraga, J. Jakubek, V. Kral, M. Kralik, C. Lebel, C. Leroy, X. Llopart, D. Maneuski, M. Nessi, V. O'Shea, M. Platkevic, S. Pospisil, M. Suk, L. Tlustos, P. Vichoudis, J. Visschers, I. Wilhelm, J. Zemlicka, *The Medipix2-Based Network for Measurement of Spectral Characteristics and Composition of Radiation in ATLAS Detector*, Nuclear Instruments and Methods A, Vol. 607, 2009, doi:10.1016/j.nima.2009.03.104

[14] Z. Vykydal, J. Bouchami, M. Campbell, Z. Dolezal, M. Fiederle, D. Greiffenberg, A. Gutierrez, E. Heijne, T. Holy, J. Idarraga, J. Jakubek, V. Kral, M. Kralik, C. Lebel, C. Leroy, X. Llopart, D. Maneuski, M. Nessi, V. O'Shea, M. Platkevic, S. Pospisil, V. Sochor, J. Solc, M. Suk, L. Tlustos, P. Vichoudis, J. Visschers, I. Wilhelm, J. Zemlicka, *Evaluation of the ATLAS-MPX Devices for Neutron Field Spectral Composition Measurement in the ATLAS Experiment*, 2008 IEEE Nuclear Science Symposium Conference Record, 2009. doi:10.1109/NSSMIC.2008.4774829

[15] D. Greiffenberg, M. Fiederle, Z. Vykydal, V. Kral, J. Jakubek, T. Holy, S. Pospisil, D. Maneuski, V. O'Shea, M. Suk, M. Kralik, C. Lebel, C. Leroy, *Detection efficiency of ATLAS-MPX detectors with respect to neutrons*, Nuclear Instruments and Methods A, Vol. 607, 2009. doi:10.1016/j.nima.2009.03.103

2008

[16] T. Holy, E. Heijne, J. Jakubek, S. Pospisil, J. Uher and Z. Vykydal, *Pattern recognition of tracks induced by individual quanta of ionizing radiation in Medipix2 silicon detector*, Nuclear Instruments and Methods A, Vol. 591, 2008. doi:10.1016/j.nima.2008.03.074

[17] J. Uher, J. Jakubek, C. Lebel, C. Leroy, S. Pospisil, R. Skoda, Z. Vykydal, *Detection of fast neutrons with the Medipix-2 pixel detector*, Nuclear Instruments and Methods A, Vol. 591, 2008. doi:10.1016/j.nima.2008.03.027

2007

[18] C. Granja, J. Jakubek, S. Pospisil, Z. Vykydal, Y. Kopatch, S. Telezhnikov, *Position-sensitive spectroscopy of 252Cf fission fragments*, Nuclear Instruments and Methods A, Vol. 574, 2007. doi:10.1016/j.nima.2007.01.164

[19] M. Campbell, V. Havranek, E. Heijne, T. Holy, J. Idarraga, J. Jakubek, C. Lebel, C. Leroy, X. Llopart, J. Novotny, S. Pospisil, L. Tlustos, Z. Vykydal, *Charge collection from proton*

and alpha particle tracks in silicon pixel detector devices, 2007 IEEE Nuclear Science Symposium Conference Record, 2007. doi:10.1109/NSSMIC.2007.4437190

[20] J. Uher, C. Frojd, J. Jakubek, S. Pospisil, G. Thungstrom, Z. Vykydal, "Directional radiation detector", 2007 IEEE Nuclear Science Symposium Conference Record, 2007. doi:10.1109/NSSMIC.2007.4437213

2006

[21] Z. Vykydal, J. Jakubek, S. Pospisil, *USB interface for Medipix2 pixel device enabling energy and position sensitive detection of heavy charged particles*, Nuclear Instruments and Methods A, Vol. 563, 2006. doi:10.1016/j.nima.2006.01.114

[22] T. Holy, J. Jakubek, S. Pospisil, J. Uher, D. Vavrik, Z. Vykydal, *Data acquisition and processing software package for Medipix-2 device*, Nuclear Instruments and Methods A, Vol. 563, 2006. doi:10.1016/j.nima.2006.01.122

[23] Z. Vykydal, J. Jakubek, T. Holy, S. Pospisil, *A portable pixel detector operating as an active nuclear emulsion and its application for X-ray and neutron tomography*, 9th ICATPP 2005 Conference Proceedings, 2006. doi:10.1142/9789812773678_0123

2005

[24] Z. Vykydal, *Microprocessor controlled USB interface for Medipix2 detector*, Diploma thesis, Czech Technical University in Prague, 2005.